# Progress and Challenges in the Synthesis of Two-Dimensional Van der Waals Ferroic Materials and Heterostructures

Jia Wang,[1] Junzhe Kang,[2] Stasiu Chyczewski,[2] Ye Lin,[2] Hanwool Lee,[2] Wenjuan Zhu,[2] Xia Hong[1*]

[1] Department of Physics and Astronomy & Nebraska Center for Materials and Nanoscience, University of Nebraska-Lincoln, NE 68588, USA

[2] Department of Electrical and Computer Engineering, University of Illinois at Urbana-Champaign, IL 61801, USA

[*] Email: xia.hong@unl.edu

**Abstract:**

Two-dimensional ferroelectric and magnetic van der Waals materials are emergent platforms for the discovery of novel cooperative quantum phenomena and development of energy-efficient logic and memory applications as well as neuromorphic and topological computing. This review presents a comprehensive survey of the rapidly growing 2D ferroic family from the synthesis perspective, including brief introductions to the top-down and bottom-up approaches for fabricating 2D ferroic flakes, thin films, and heterostructures as well as the important characterization techniques for assessing the sample properties. We also discuss the key challenges and future directions of the field, including scalable growth, property control, sample stability, and integration with other functional materials.

## 1. Introduction

Since the discovery of ferroelectricity and magnetism in two-dimensional (2D) van der Waals (vdW) materials, 2D ferroics and their heterostructures have attracted enormous research interests for both fundamental studies and technological developments [1-5]. For ferroic materials, the order parameters, such as the electric polarization for ferroelectrics, magnetization for ferromagnets and ferrimagnets, and staggered magnetization for antiferromagnets, can be controlled through external stimuli (electric field or magnetic field), resulting in switching hysteresis loops (**Fig. 1**), domain formation, or even quantum phase transitions [3]. Compared with their bulk counterparts, 2D ferroics can potentially overcome the finite size effects and provide versatile platforms for imposing nanoscale control of the ferroic order, correlation energy, magnetic exchange, spin-orbit coupling, symmetry, and topology of the system through electric field effect doping [6] or strain [7, 8]. It is also possible to stack different vdW materials into heterostructures that host multiferroic responses [9-11] or chiral spin textures [12]. Novel ferroic states can be further generated in vdW multilayers via engineering the twist angle [13-15], layer sliding [14], and stacking order [16, 17]. Capitalizing on the tremendous progress in the computational search and material synthesis, various 2D ferroics are made available over the last ten years for exploring emergent quantum phenomena [18] and developing high performance logic and memory devices as well as novel device applications for neuromorphic and topological computing [2, 19].

Layered $CuInP_2S_6$ (CIPS) was first confirmed experimentally to be ferroelectric in 2015 [20], although the theoretical prediction dated back to 1976 [21]. In 2017, magnetism down to monolayer thickness was discovered in ferromagnetic $Cr_2Ge_2Te_6$ [22] and antiferromagnetic $CrI_3$ [23] using magneto-optical Kerr effect (MOKE). The past few years have witnessed a surge in the discovery of 2D ferroic materials and their heterostructures. Spontaneous ferroelectric state has

been observed in various ultrathin 2D vdW materials, including CIPS [20, 24-28], $CuCrP_2S_6$ [29-32], α- and β-$In_2Se_3$ [33-41], SnTe [42-44], SnS [45-51], SnSe [52-54], GeS [55, 56], GeSe [57, 58], 1T'-$MoTe_2$ [59, 60], 1T'-$WTe_2$ [61-63], and $NbOI_2$ [64-66]. Magnetism has been reported in a wide range of layered transition metal chalcogenides/halides, including $Cr_2Ge_2Te_6$ [22, 67, 68], $CrI_3$ [23, 69-73], $CrCl_3$ [72-76], $CrBr_3$ [72, 73, 77-81], $VSe_2$ [82-84], $Fe_3GeTe_2$ [85-91], $Fe_5GeTe_2$ [92-95], $Fe_3GaTe_2$ [96, 97], and $MnBi_2Te_4$ [98-100]. Various emergent phenomena have been theoretically predicted or experimentally discovered in these 2D ferroics, such as intercorrelated in-plane and out-of-plane polarization switching [41] and multi-directional memristive effect in α-$In_2Se_3$ [101], unconventional quadruple energy well [102], giant negative piezoelectricity [103, 104], and interfacial lattice coupling enhanced piezoelectricity and ferroelectricity in CIPS [105], structural phase transition induced via electrostatic doping [106] and strain [107] in 1T'-$MoTe_2$, giant spin filter effect in graphene/$CrI_3$/graphene tunnel junctions [69], stacking order-induced magnetic transition in $CrI_3$ [108, 109], interface engineered magnetic skyrmions in $Fe_3GeTe_2$ [12, 85], even-odd layer-dependent anomalous Hall effect (AHE) in $MnBi_2Te_4$ [98], and the interfacial magnetoelectric coupling in MnSeTe/$In_2Se_3$ [11]. Emergent ferroelectricity [110-112] and moiré magnetism [14] have been identified in various stacking-engineered vdW multilayer systems. 2D ferroic materials and their heterostructures have also been utilized to develop novel device concepts [2, 113], such as negative-capacitance field effect transistors (FETs) [114-116], ferroelectric semiconductor FETs [25, 117, 118], memoristors [101, 119], phase-change transistors [107], programmable rectifiers [120], tunnel junctions with ferroic tunnel barriers [69-74, 121-124], ferrovalley memory [111], and spin tunneling FETs [6]. Several review papers have documented the significant progress in the exploration and understanding of the emergent phenomena [4, 5, 125-128] and development of potential applications [2, 127-129] of 2D ferroics.

Accelerated materials advancement is facilitated by the positive feedback loop between computational material search, material synthesis, property characterization and modelling, and device applications. The root of these discoveries lies in the availability of high-quality 2D ferroic materials. Compared with single crystal samples, 2D thin films possess high tunability of properties and can facilitate technological implementations due to the scalable growth and compatibility with industrial processing. This review centres on the recent advancements in the synthesis of emergent 2D ferroic flakes, thin films, and their heterostructures, including a brief overview of the synthesis techniques and available characterization methods for assessing the sample properties, and discusses the existing challenges and future directions in the field.

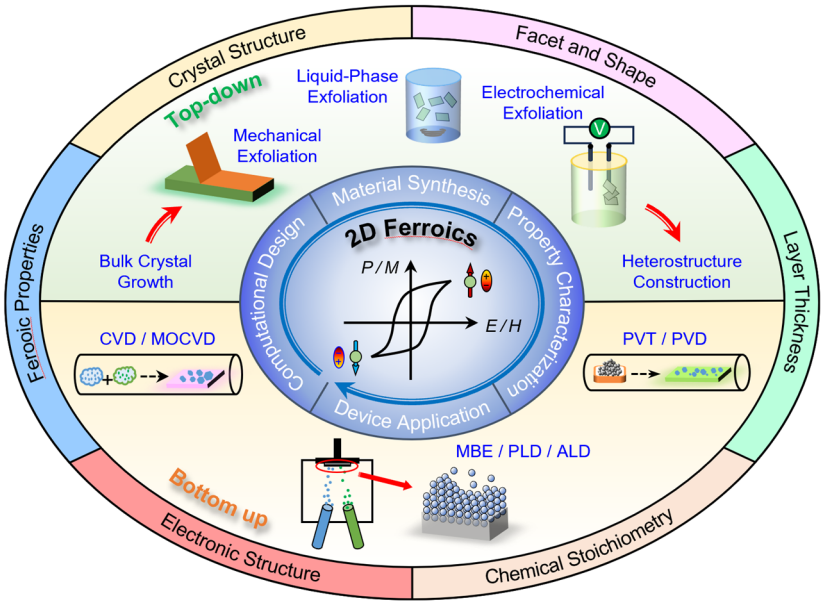


**Figure 1.** Overview of 2D research based on vdW ferroics showing ferroelectric/ferromagnetic switching hysteresis, research flow, synthesis techniques, and critical material considerations.

## 2. Synthesis Methods

The synthesis methods for achieving single phase ferroics in the 2D limit can be categorize into the top-down approaches, where atomically thin flakes are isolated from bulk crystals, and the bottom-up approaches, which involve direct growth of isolated flakes or continuous films on

designated substrates. As illustrated in **Fig. 1**, in the top-down approaches, high-quality bulk crystals are first obtained by melting growth, flux growth, or chemical vapor transport (CVT) methods and then then isolated into atomically thin flakes using various exfoliation techniques, including mechanical, liquid-phase, and electrochemical exfoliations. In the bottom-up approach, van der Waal flakes and thin films are deposited on the substrates directly, employing techniques such as chemical vapor deposition (CVD), physical vapor transport or deposition (PVT/PVD), and molecular beam epitaxy (MBE). The choice of preparation method for 2D ferroics depends on the desired material properties and potential applications.

Both top-down and bottom-up methods can be applied to fabricate ferroic heterostructures. The vdW heterostructures can be divided into three categories: vertical heterostructures, horizontal heterostructures, and core/shell structures (**Fig. 2**), which can have different types of interfacial bonding. The vertical heterostructures possess vdW interfaces, which can be realized through either direct growth (bottom-up methods) or stacking of individual layers (top-down methods). Both horizontal and core-shell heterostructures involve interfacial chemical bonding and can only be achieved via the bottom-up methods.

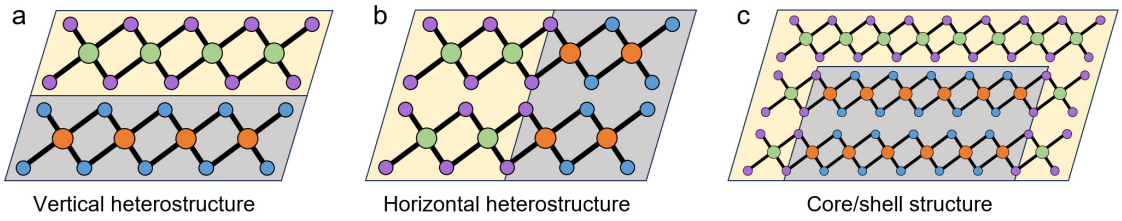


**Figure 2.** Different types of vdW heterostructures. (a) Vertical heterostructure. (b) Horizontal heterostructure. (c) Core/shell structure.

### 2.1 Top-Down Methods

The high-quality single crystals serve as essential material foundations for fundamental studies of material properties. Ultrathin flakes can then be isolated from the bulk samples through various

exfoliation techniques. The exfoliated samples can preserve to the maximum extent the intrinsic material properties and can be further stacked into homo- and heterostructures that host various emergent phenomena that are often distinct from the parent vdW materials.

### 2.1.1 Bulk Crystal Growth

The CVT and flux methods are two primary processes used for synthesizing bulk vdW ferroic materials [130, 131]. In CVT, the precursor materials and transport agents (such as $I_2$, $Br_2$) are sealed in a quartz ampoule, which is put inside a tube furnace with a controlled temperature gradient [131]. At the hot end of the ampoule, the volatile transport agent combines with the precursor components to form intermediate molecular species, which then diffuse to the cold end of the ampoule. When the partial pressure of the intermediate molecular species reaches a critical level, crystallization occurs at the cold end and the transport agent is released [131]. Many vdW ferroic materials have been synthesized using CVT method, including $Fe_3GeTe_2$ [86, 132], $Fe_5GeTe_2$ [94, 95], $CrI_3$ [133], $CuInP_2S_6$ [20, 24-27, 134, 135], $In_2Se_3$ [136], and $NbOI_2$ [64-66].

The flux method is another effective approach to grow single crystal materials [137, 138]. Unlike CVT, the flux method uses molten solids as solvents (or fluxes) instead of volatile transport agent. The flux, which is usually inorganic solids at room temperature, such as KCl, NaCl, and Te, melts at a low temperature [137, 138]. In a conventional vertical flux growth, the source materials are placed in a small crucible along with a large excess of the flux [138]. A frit filter and an empty crucible are placed on the top of the source crucible [138]. The entire stack is sealed in a silica tube and placed in a furnace. At high temperature, the source materials are dissolved into the flux forming a homogeneous eutectic liquid. When the temperature of the system is slowly reduced, the homogeneous eutectic liquid becomes supersaturated, leading to the slow nucleation and crystallization of high-quality crystals [138]. Various vdW ferroic materials have been synthesized

using the flux method, including $Fe_3GaTe_2$ [96, 97], $Cr_2Ge_2Te_6$ [22, 67, 68], $CrTe_3$ [139], $Fe_3GeTe_2$ [139], and $CuInP_2S_6$ [139]. The flux method has high potential for synthesizing high-quality vdW ferroic crystals with low defects. However, for certain complex vdW materials with unknown phase diagrams, the CVT method is needed.

### 2.1.2 Mechanical Exfoliation

The mechanical exfoliation method exploits the adhesive tape to peel off thin vdW flakes from bulk crystals, which are then laid on a designate substrates for device fabrication [140, 141] or further dry transfer [142]. It has been widely adopted for fundamental studies of 2D vdW materials as it capitalizes on the high quality, low defect bulk samples and preserves to the maximum extent the intrinsic material properties. **Figure 3a-c** shows the atomic force microscopy (AFM) images of mechanically exfoliated vdW ferroelectrics CIPS (**Fig. 3a**) [24-26, 66], α-$In_2Se_3$ (**Fig. 3b**) [33, 34, 36], and $NbOI_2$ (**Fig. 3c**) [65], where the ferroelectric properties have been characterized via piezoresponse force microscopy (PFM). Magnetic vdW flakes prepared via mechanical exfoliation include $CrX_3$ (X = I, Br, Cl) (**Fig. 3d-e**) [23, 69, 72, 73, 75, 76, 78, 81, 143], $NiPS_3$ (**Fig. 3f**) [144, 145], $Cr_2Ge_2Te_6$ [22], $Fe_3GeTe_2$ [86, 87], and $MnBi_2Te_4$ [146-148].

Recently, an advanced exfoliation method has been developed with the assistance of metal (*e.g.*, Au) or simple metal oxide (*e.g.*, $Al_2O_3$). As the adhesion between metals and 2D materials is stronger than the interlayer bonding of 2D crystals, it is easier for 2D flakes to be exfoliated on the metal surface [149, 150]. This advanced exfoliation method enables the production of large-size 2D flakes with high yield [151-154] and has been successfully applied to various 2D ferroic materials (**Fig. 3g**) [86, 150].

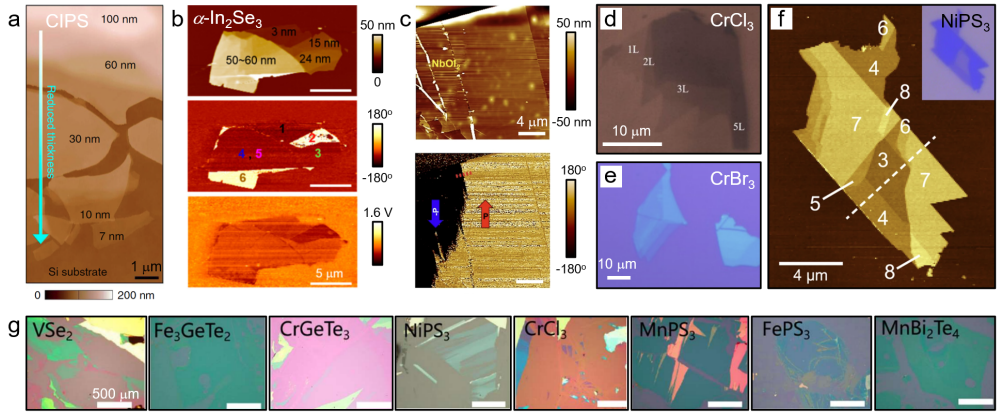


**Figure 3.** Mechanical exfoliation. (a) AFM image of CIPS on doped Si. (b) AFM (top) and PFM phase (middle) and amplitude (bottom) images of α-$In_2Se_3$ on Au. (c) AFM (top) and PFM phase (bottom) images of $NbOI_3$ on Au. (d) Optical microscopy image of $CrCl_3$ on $SiO_2$/Si. (e) Optical image of $CrBr_3$ on $SiO_2$/Si. (f) AFM and (inset) optical image s of $NiPS_3$ on $SiO_2$/Si. (g) Optical image s of various 2D ferroic flakes on Au/Ti-coated $SiO_2$/Si. (a) Adapted figure cited from [24]. Copyright © 2016, The Author(s). (b) Adapted figures with permission from [33]. Copyright © 2017, American Chemical Society. (c) Adapted figures cited from [65]. Copyright © 2022, The Author(s). (d) Adapted figure cited from [143]. Copyright © 2020 IOP Publishing Ltd. (e) Adapted figure cited from [78]. Copyright © 2022 IOP Publishing Ltd. (f) Adapted figure cited from [145]. Copyright © 2016, The Author(s). (g) Adapted figures cited from [150]. Copyright © 2020, The Author(s).

### 2.1.3 Liquid Phase Exfoliation

Liquid-phase exfoliation presents an effective alternative to the mechanical exfoliation method for achieving high-quality 2D vdW nano-materials [155-158]. It utilizes dispersion and sonication in proper solvent to achieve exfoliation. As shown in **Fig. 4a**, bulk crystals dispersed in the solvent experience the intercalation and agitation stages: the intercalation of ions or molecules between adjacent layers leads to an expansion of the interlayer spacing and suppression of adhesion; subsequent sonication then facilitates the breaking of materials into layered flakes, which can be isolated from the solvent [156]. For example, ferroelectric α-$In_2Se_3$ flakes have been prepared via

chemical intercalation in a mixed solution of polyvinylidene fluoride and tetrabutylammonium bromide [159], yielding large size α-$In_2Se_3$ flakes with average thickness of 1.6 μm, smooth surface, and high crystallinity (**Fig. 4b-c**). Liquid phase exfoliation has also been used to achieve CIPS nanosheets with smooth surfaces and thickness ranging from 50 to above 100 nm (**Fig 4d**) [160].

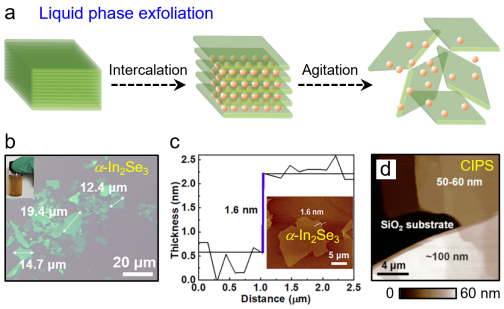


**Figure 4.** Liquid phase exfoliation. (a) Process schematic. (b-c) α-$In_2Se_3$ flakes. (b) Optical image. (c) AFM height profile with (inset) topography image. (d) AFM image of CIPS flakes with different thickness on $SiO_2$ substrate. (b-c) Adapted figures with permission from [159]. Copyright © 2022, American Chemical Society. (d) Adapted figures with permission from [160]. Copyright © 2020 Elsevier Ltd. All rights reserved.

### 2.1.4 Electrochemistry Exfoliation

Electrochemistry exfoliation method can be utilized for mass production of 2D materials and has been adopted to synthesize graphene [161-164], transition metal dichalcogeneides (TMDs) [165, 166], and h-BN [167]. It involves the intercalation of anions or cations into a bulk crystal in liquid environment. Under a fixed potential between two electrodes, with the bulk crystals serving as either cathodes or anodes (**Fig. 5a**) [168], ionic species within the liquid intercalate into the 2D materials, weakens the interlayer bonding, and expands the layer spacing, resulting in layer separation. In anodic exfoliation, bulk material serves as the anode and accumulates negative charges (*e.g.*, $SO_4^{2-}$). In cathodic exfoliation, bulk material serves as cathode and attracts positive

charged ions (*e.g.*, $Li^+$). For example, thin α-$In_2Se_3$ samples have been produced through a standard cathodic electrochemical insertion process, with bulk $In_2Se_3$ as the cathode and a Pt foil as the anode (**Fig. 5b**) [169]. Scanning electron microscopy (SEM) studies show that the exfoliated samples have lateral sizes larger than 5.0 μm and exhibit uniform elemental distribution (**Fig. 5c**). Gao *et al.* used bulk $In_2Se_3$ as cathode and carbon rods as anode and obtained ultrathin α-$In_2Se_3$ flakes, where over 90% of flakes have thickness of 2.2 nm (**Fig. 5d**) [170].

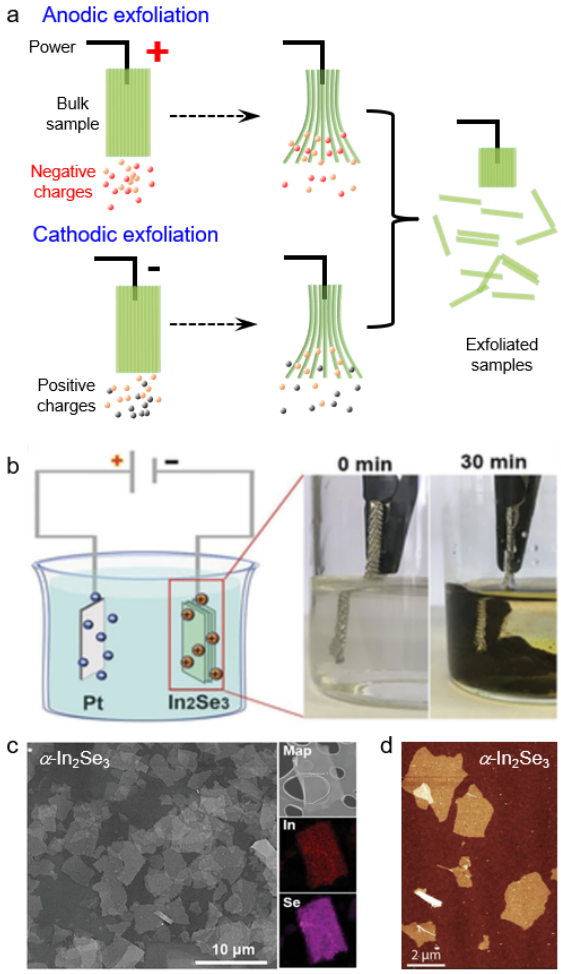


**Figure 5.** Electrochemistry exfoliation. (a) Schematic of anodic and cathodic exfoliations. (b) Schematic of α-$In_2Se_3$ exfoliation (left), and optical image s of the experimental setup at 0 minute (middle) and 30 minutes (right) after intercalation. (c) SEM image of α-$In_2Se_3$ flakes (left) and elemental maps of a α-$In_2Se_3$ flake. (d) AFM image of *α*-$In_2Se_3$. (b-c) Adapted figures with permission

from [169]. Copyright © 2020 WILEY-VCH Verlag GmbH & Co. KGaA, Weinheim. (d) Adapted figures cited from [170]. Copyright © 2022 by the authors.

### 2.1.5 Heterostructure Stacking

Stacking 2D ferroic flakes into heterostructures can lead to emergent phenomena and novel functionalities. **Figure 6a** illustrates the dry transfer process for creating vdW heterostructures, where a 2D flake is picked up by a polymer film (*e.g.,* gel-film) and transferred onto a target substrate [142]. The second layer of 2D material is then picked up, aligned at a certain twist angle, and then placed on the top of the first 2D flake. Repeating these steps can yield a complex heterostructure. The lattice mismatch between different vdW layers or twisting between the same type of vdW layers can lead to moiré patterns (**Fig. 6b**). It has been shown that twisting 2D magnet $CrI_3$ trilayers possess periodic patterns with alternating ferromagnetic and antiferromagnetic domains [13] and $CrI_3$ bilayers can host noncolinear spin textures [14]. Emergent ferroelectricity has been observed in 2D multilayer systems consisting of non-ferroelectric or even non-polar vdW layers [171, 172], including stacking-engineered h-BN (**Fig. 6c**) [15, 17, 173], twisted TMDs (**Fig. 6d**) [17, 174], and twisted bilayer graphene (**Fig. 6e**) [175, 176].

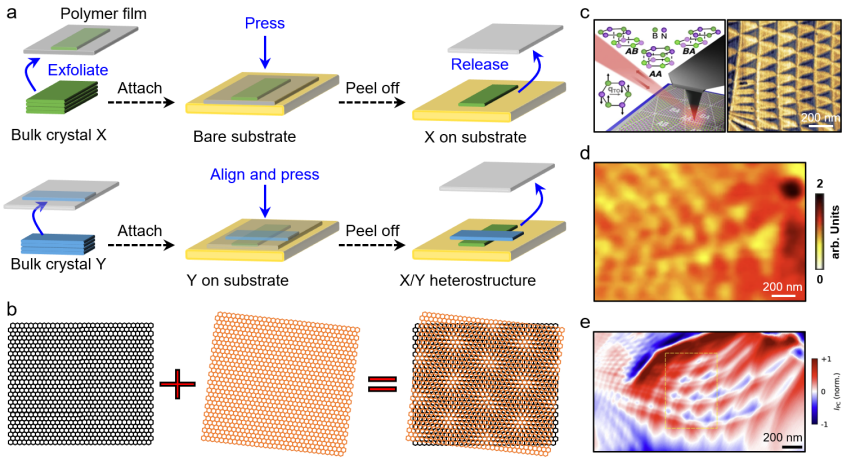


**Figure 6.** Heterostructure assembling. (a) Schematic of the transfer and stacking process. (b) Schematic of moiré patterns formed by stacking two honeycomb monolayers with a twist angle. (c) Schematic of

near-field nanoimaging (left) and PFM amplitude image (right) of a bilayer h-BN sample. (d) Near-field mapping of a twisted bilayer of $WSe_2$ sample. (e) Photocurrent mapping of a twisted bilayer graphene sample. (c) Adapted figures cited from [174]. Copyright © 2021, The Author(s). (d) Adapted figure cited from [177]. Copyright © 2023, The Author(s). (e) Adapted figure cited from [176]. Copyright © 2021, The Author(s).

## 2.2 Bottom-Up Methods

Although bulk ferroic crystals provide a route for achieving ultrahigh-quality, crystalline flakes of materials for scientific investigations, they are not considered suitable for large-area ferroelectric and magnetic devices. Large-scale synthesis of vdW ferroic thin films using bottom-up techniques such as CVD, PVT, and MBE, is a critical step in realizing technologically relevant 2D ferroic layers.

### 2.2.1 Vapor Phase Deposition

Vapor phase-based direct growth methods such as CVD and PVT offer controlled and cost-effective approaches for producing large-area, high-quality 2D flakes or thin films. The typical growth apparatus for CVD and PVT consists of a tube furnace, where the vapor-solid process occurs. **Figure 7a** shows the schematic growth setup with solid precursors. In the CVD process, the chalcogen or halogen powder and the metal inorganic compound powder are placed upstream in the hot zone of the tube furnace. and the substrates are placed downstream (or face down directly on top of the metal compound crucible). Upon heating, the metal compound and chalcogen/halogen powders are vaporized and transported downstream in the furnace, coating the substrate and forming vdW ferroic thin films. As it is better to control the growth temperature of different source materials according to their melting temperatures, precursors containing different source materials can be held at different furnace zones for individual temperature control ($T_{source}$).

For example, ferrimagnetic $Cr_2S_3$ thin flakes has been synthesized using solid source powders of Cr (mixed with salt NaCl, $T_{source}$ ~ 750 °C) and S ($T_{source}$ ~ 200 °C) [178], or source powders of $CrCl_2$ ($T_{source}$ ~ 830 °C) and S ($T_{source}$ at lower temperature) [179]. Ferromagnetic $VSe_2$ flakes has been synthesized using source powders of $V_2O_5$ (mixed with KI, $T_{source}$ ~ 500-700 °C) and Se ($T_{source}$ at lower temperature) [180].

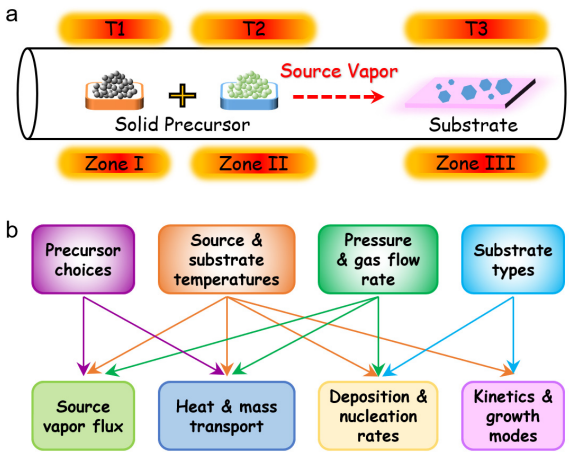


**Figure 7.** Vapor phase deposition. (a) Schematic tube furnace system during the vapor phase-based direct growth of 2D materials. (b) Impacts of various growth parameters.

In the PVT process (also known as PVD), the precursor with the same chemical formula as the target material is used as the sole source. PVT (or PVD) is characterized by a process in which the material transitions from a condensed phase to a vapor phase and then back to a thin film condensed phase. The fundamental difference between CVD and PVT lies in that a chemical reaction occurs during the CVD growth process [178-182], while only a change in crystalline type or morphology (without chemical reaction) takes place in the PVD process [45, 183-185].

The parameters governing vapor phase-based direct growth include the precursor choice, growth temperature, substrate type, gas pressure and flow rate, and growth time (**Fig. 7b**) [186, 187]. These parameters collectively affect the growth mode, and their impacts can be highly intertwined. The **precursors** or source materials act as the reactants for growth and can be either

vapor or solid sources. Solid precursors such as powders are most used for the synthesis of 2D ferroic materials, including ferroelectric semiconductors SnS [45, 185, 188] and $In_2Se_3$ [183, 184] and 2D magnets $CrCl_3$ [74] and $Cr_5Te_8$ [181, 182]. Since the temperature window for the decomposition reaction of these solid precursors is very narrow, it is critical to have precise temperature control for the solid precursors.

Among all growth parameters, the **source temperature** is the one that directly affect the decomposition reaction of the solid source as it determines the equilibrium concentration of the source vapor. A slight variation of temperature will lead to a large change of the decomposition rate, which affect the sample deposition on the substrates. Generally, a higher source temperature corresponds to a higher source vapor concentration and results in a higher growth rate on the substrate. The **substrate temperature** is a critical parameter controlling the growth mode, affecting both the sample nucleation and the kinetics of lateral and vertical growth. Usually, a higher substrate temperature is preferable for achieving ultrathin flakes with large lateral size. However, the high substrate temperature also leads to a higher decomposition probability of the 2D flakes, so the materials may not be successfully grown on the substrate if the temperature is too high.

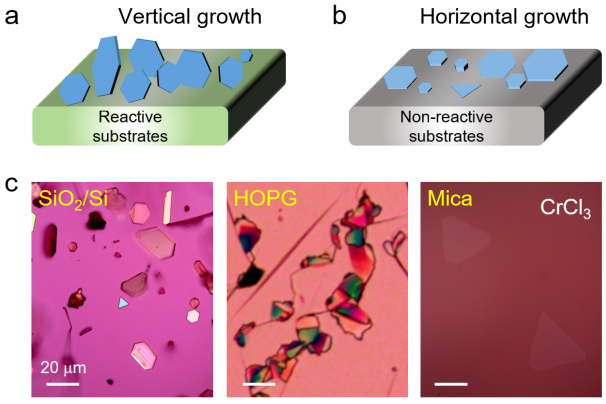


**Figure 8.** Effect of substrate on growth mode. (a) Schematic of vertical growth of 2D samples on reactive substrate. (b) Schematic of horizontal growth of 2D flakes on reactive substrate. (c) Optical

image s of $CrCl_3$ samples grown on $SiO_2$/Si, HOPG, and mica via PVT. (c) Adapted figures cited from [74]. Copyright © 2022 The Authors. Advanced Science published by Wiley-VCH GmbH.

The **substrate** choice plays an important role in absorbing adatoms from the source materials, promoting nucleation, and stimulating growth. **Figure 8a-b** illustrates two possible growth modes of 2D flakes on the substrates. There are two types of substrates commonly used for the growth of 2D ferriocs: the reactive substrates such as Si/$SiO_2$ wafers and the non-reactive vdW substrates such as highly ordered pyrolytic graphite (HOPG) crystal and mica. For the reactive substrate, the adatoms/molecules from the source vapor are likely chemisorbed onto the substrate and form random nucleation sites. Due to the chemical bonding (covalent or ionic) between the adatoms and substrate, the adatoms have low mobility on the substrate surface and the sample may favour vertical growth to minimize the interface energy (**Fig. 8a**). For the non-reactive substrate, besides individual nucleation sites promoted by defects (*e.g.*, layer edges and grain boundaries), the adatoms are mostly physiosorbed onto the substrate surface and have high mobility. They can be attached to the edges of existing flakes either directly from the source vapor or through diffusion on the substrate. The vdW bonding between the 2D flake and the substrate lowers the interface energy and favours horizontal growth (**Fig. 8b**) [189]. In recent studies, the horizontal growth of various 2D vdW flake has been demonstrated on non-reactive vdW substrates [45, 178-185]. For example, Wang *et al.* have shown that PVT growth of $CrCl_3$ on reactive substrate $SiO_2$/Si prefers vertical growth mode, producing relatively thick crystals growth mode via PVT method, while on non-reactive substrates such as HOPG and mica $CrCl_3$ prefers horizontal growth, resulting in thin flakes with large lateral dimensions (**Fig. 8c**) [74].

**Pressure** in the tube furnace can vary over a wide range from the ambient conditions to vacuum (several millitorr). The pressure and carrier gas **flow rate** collectively determine the

thermodynamic heat and mass transport in the growth apparatus and have a large influence on the source vapor flux on the substrate. Generally, a lower pressure corresponds to a lower source vapor concentration and can be used to facilitate controllable reaction. However, some reaction cannot be initiated at low pressure, *e.g.*, the deposition of $Cr_2S_3$ [178, 179], $CrCl_3$ [74], and $Cr_5Te_8$ [181, 182] has been realized at the atmospheric pressure.

### 2.2.2 Epitaxy Growth

MBE is a powerful technique for epitaxy growth of high-quality 2D vdW materials in the forms of both isolated flakes and continuous films. As shown in **Fig. 9a**, the solid source materials are contained in separate effusion cells and evaporate upon heating. As the growth occurs in ultra-high vacuum, the evaporated atoms have long mean free paths and do not interact until they reach the substrate. This facilitates atomic-level control of the growth mode and low impurity density. Once the arriving atoms stick to the substrate, they can diffuse, absorb, or desorb, and the relative rates depend on the substrate type and temperature.

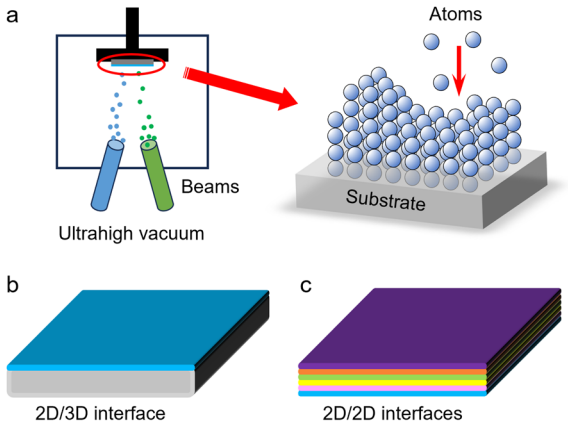


**Figure 9.** Epitaxy growth. (a) Schematic of MBE growth. (b-c) Schematics of 2D/3D interface (b) and 2D/2D interfaces (c) for the 2D materials growth.

For the epitaxial growth of 2D materials, the important control parameters include the source flux ratio, substrate type, substrate temperature, and gas pressure. By systematically optimizing

these parameters, it is possible to achieve layer-by-layer growth of 2D flakes or films with the desired stoichiometry, crystal structure, and morphology. An MBE system can contain multiple effusion cells, each containing one type of **source material**. The sample stoichiometry and even polymorph forms can be varied by tailoring the flux ratio of different effusion cells. For example, in the synthesis of $In_xSe_y$, crucible cells containing $In_2Se_3$ and Se powders have been held at different temperatures. Controlling the flux ratio can result in InSe films ($In_2Se_3$:Se = 1:3) [190], $\alpha$-$In_2Se_3$ films ($In_2Se_3$:Se = 1:6) [190], and $\beta$-$In_2Se_3$ flakes ($In_2Se_3$:Se = 1:10) [191].

For conventional epitaxial growth, the choice of **substrates** requires compatible crystal structures and lattice parameters with the target materials due to the 2D/3D interface (**Fig. 9b**). For example, sapphire has been used to grow 2D ferroics such as $Fe_3GeTe_2$ [88, 89] and $Fe_5GeTe_2$ [92]. However, the dangling-bond-free surface of 2D vdW materials can also eliminate the lattice constraint [192]. In previous studies, graphene buffered $SiO_2$/Si or SiC wafers and vdW bulk crystals such as HOPG have been exploited to create the 2D/2D interface (**Fig. 9c**). For example, continuous ferroelectric $In_2Se_3$ films have been achieved on Si/$SiO_2$ wafers buffered by monolayer graphene [190], monolayer films of antiferromagnetic $CrCl_3$ have been deposited on graphene buffered SiC substrates [193], and isolated ferromagnetic $CrBr_3$ flakes have been synthesized on HOPG [77] and bulk vdW $NbSe_2$ [79]. The vdW layered substrates thus present a versatile venue for epitaxial growth of 2D materials.

For controlled MBE growth, the **gas pressure** is typically in the range of $10^{-8}$ to $10^{-12}$ torr. The slow deposition rate, often below 1 nm per second, facilitates the layer-by-layer growth of 2D films or flakes on the substrate, minimizing defect and impurity sites. The synthesized epitaxial samples can possess high crystalline quality and atomically smooth surfaces. The control of the effusion cell and substrate **temperatures** is also critical and depends on the material types. In

general, the growth temperature for MBE is much higher than those for the CVD/PVT methods. In this regard, mica is not a good substrate option for MBE growth, since it cannot be used in temperatures that exceed 750 $^{o}$C [194].

### 2.2.3 Other Growth Methods

In addition to CVD, PVD and MBE, several other synthesis methods, including metal organic chemical vapor deposition (MOCVD), pulsed laser deposition (PLD), and atomic layer deposition (ALD), can be used to synthesize vdW ferroic materials [195-197]. 2D ferromagnetic $CrTe_2$ was grown epitaxially on $Al_2O_3$ substrates using PLD [195]. Semi-metallic 1T' phases $MoTe_2$ films were synthesized on a 4 inch $SiO_2$/Si wafer with high spatial uniformity via MOCVD [196]. Highly crystalline FeSe, CoSe and NiSe films were deposited using ALD process, showing excellent conformality into 10:1 high-aspect-ratio micro-trenches [197]. Compared to CVD, which uses solid precursors, MOCVD with liquid or gas precursors and a showerhead configuration provides much better uniformity and larger scale coverage on the wafer [198], which is critical for industrial applications. The self-limiting and alternating nature of surface reactions gives ALD its unique advantages, including excellent reproducibility, precise thickness control, and exceptional conformality on complex-shaped substrates. Additionally, the low-temperature process in ALD makes it compatible with back-end-of-line processes [197].

### 2.2.4 Heterostructure Growth

Despite the numerous reports on the direct growth of vdW heterostructures [199-202], only few studies have focused on the direct synthesis of 2D ferroic heterostructures. Among them, vapor phase deposition has been exploited to produce vertical [203-206], horizontal [207, 208], and core/shell ferroic heterostructures [188] (**Fig. 2**). For example, Li *et al.* demonstrated a one-step CVD method to grow vertical $SnS_2$/SnS heterostructures on mica using S and SnS powders as

precursors [203]. In a same growth, they have obtained SnS flakes, SnS/$SnS_2$ vertical heterostructures, $SnS_2$ flakes in different deposition zones (**Fig. 10a**). The authors attributed the different compositions at different substrate positions to the change of precursor concentration, showing that the SnS vapor concentration decreases with the precursor-substrate distance, while the S vapor remains the same. The samples tend to form pure SnS with high SnS/S ratio and pure $SnS_2$ with low SnS/S ratio. When the SnS and S concentrations are comparable, vertical $SnS_2$/SnS heterostructure start to form.

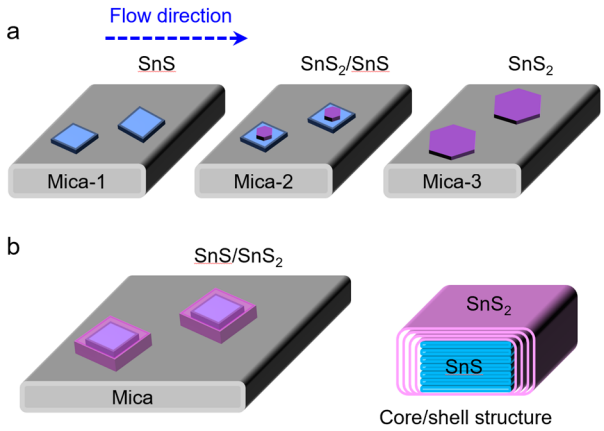


**Figure 10.** Schematic of heterostructure growth via vapor deposition. (a) CVD growth of SnS flakes, $SnS_2$/SnS vertical heterostructures, and $SnS_2$ flakes at different substrate positions. (b) SnS/$SnS_2$ core/shell heterostructures growth. The core is SnS, and the shell is $SnS_2$.

The SnS/$SnS_2$ heterostructures have also been synthesized via CVD, where SnS powder containing a small proportion of $SnS_2$ phase or S powder has been used to achieve extremely high SnS/S ratio [188]. The SnS/$SnS_2$ core/shell heterostructures form spontaneously with SnS cores and $SnS_2$ shells (**Fig. 10b**). The key parameter for controlling the shell thickness is the precursor concentration, which can be adjusted by varying the SnS/S precursor ratio or having the samples reacting with pure S vapor after growth.

### 2.3 Comparison

**Table 1** compares the pros and cons of the mechanical exfoliation, vapor phase deposition, and MBE methods for preparing vdW ferroic flakes and thin films in terms of sample quality, controllability, uniformity, scalability, and the commercialization potential. We do not include liquid phase and electrochemical exfoliation for comparison as they are implemented in solvent, while many 2D magnets are sensitive to water moisture and cannot be produced using these two methods.

**Table 1.** Comparison of mechanical exfoliation, vapor phase deposition, and MBE methods for synthesizing 2D ferroic flakes and thin films.

| | **Mechanical Exfoliation** | **Vapor Phase Deposition** | **MBE** |
|---|---|---|---|
| **Experimental setup cost** | Low | Affordable | High |
| **Process throughput** | Low | High | High |
| **Sample quality** | Excellent | Good | Excellent |
| **Controllability** | Poor | Good | Excellent |
| **Uniformity** | Poor | Good | Excellent |
| **Scalability** | Poor | Good | Excellent |
| **Commercialization potential** | Low | High | Low |

The mechanical exfoliation approach has been widely exploited for obtaining high quality 2D ferroic thin flakes. The exfoliated samples preserve the pristine ferroelectric/magnetic properties of the materials, which is critical for fundamental studies. While this method is low cost, it cannot produce scalable, wafer-size samples and is thus not viable for industrial applications.

Vapor phase deposition such as CVD and PVT is a cost-effectiveness method to produce large-scale 2D flakes and films with controlled shape, size, and thickness. It can also control the structural phase and stoichiometry and enable heterostructure construction. These advantages make vapor phase deposition promising for industrial production of 2D ferroics, as demonstrated

for CVD-graphene films [209, 210]. The main drawback of this technique is the relatively low sample quality of 2D ferriocs, including high-density defects and grain boundaries, compared to those synthesized via mechanical exfoliation and MBE growth.

Epitaxial growth like MBE offers distinct advantages over the exfoliation and vapor deposition techniques in controlling sample quality and growth mode. The MBE technique provides precise control of sample growth at the atomic level, so the synthesized flakes or films can be highly uniform with low defect density. For the layer-by-layer growth mode, samples with well-defined crystal structure and orientation can be achieved by choosing proper substrates. However, the MBE growth is characterized by its complex growth conditions, relatively slow growth rates, constraints on the substrate/sample sizes, and high operation cost for maintaining the ultrahigh vacuum conditions, thus not viable for industrial production. Also, not all materials can be easily evaporated and deposited via MBE, limiting the choice of source materials.

## 3. Characterization Techniques

### 3.1 Characterization of 2D Ferroelectrics

2D ferroelectrics presents a significant challenge to conventional electrical methods for characterizing dielectric properties and *P*-*E* loops due to the markedly reduced sample dimensions in comparison to their bulk counterparts. It is thus imperative to employ more sensitive techniques or local probes to investigate ferroelectricity at the nanoscale. The PFM, second-harmonic generation (SHG), and scanning tunneling microscopy (STM) techniques have proven effective in probing the properties of 2D ferroelectrics.

AFM-based techniques such as PFM and conductive-AFM (c-AFM) are powerful technique to visualize ferroelectric domain structures, identify and control polarization directions, and quantify the piezoelectric responses of nanoscale materials [211]. Employing a conductive AFM

probe as an *in situ* electrode, PFM detects the local piezoelectric deformation induced by the tip bias. It has been exploited to investigate ferroelectricity and piezoelectricity in a wide range of 2D materials [24, 33-35, 41, 65, 105, 212]. For example, PFM phase and amplitude images have been utilized to resolve ferroelectric domain structures in α-$In_2Se_3$ (**Fig. 3b** and **11a**) [33, 35, 41] and CIPS (**Fig. 11b**) [24, 212]. The domain structure can be further controlled locally using c-AFM. It has been shown that the polarization direction of α-$In_2Se_3$ can be precisely controlled by c-AFM (**Fig. 11a**) [35]. For CIPS flakes, domain writing yields irregular, diffusive domain walls (DWs) (**Fig. 11b**) [24], which can be attributed to the highly mobile Cu ions. By studying the piezoresponse amplitude as a function of tip vias voltage ($V_{bias}$), it is also possible to quantify the piezoelectric coefficient ($d_{33}$). As shown in **Fig. 11c-d**, thin CIPS flakes interfaced with ferroelectric oxide $Pb(Zr,Ti)O_3$ (PZT) exhibit a much stronger PFM amplitude signal compared with those prepared on dope Si and Au, which has been attributed to the interfacial lattice coupling with PZT [105]. It results in a lattice distortion of the interfacial CIPS layer that tilts the quadruple energy well, which favors the metastable state, leading to an enhanced positive $d_{33}$ in CIPS (**Fig. 11d**). *In situ* PFM has been exploited to track the evolution of domain structures at elevated temperatures for CIPS on PZT (**Fig. 11e**), which reveals a ferroelectric Curie temperature ($T_C$) exceeding 200°C, over 50% enhancement over the bulk value. This value is in good agreement with theoretical prediction considering the interfacial lattice distortion [105].

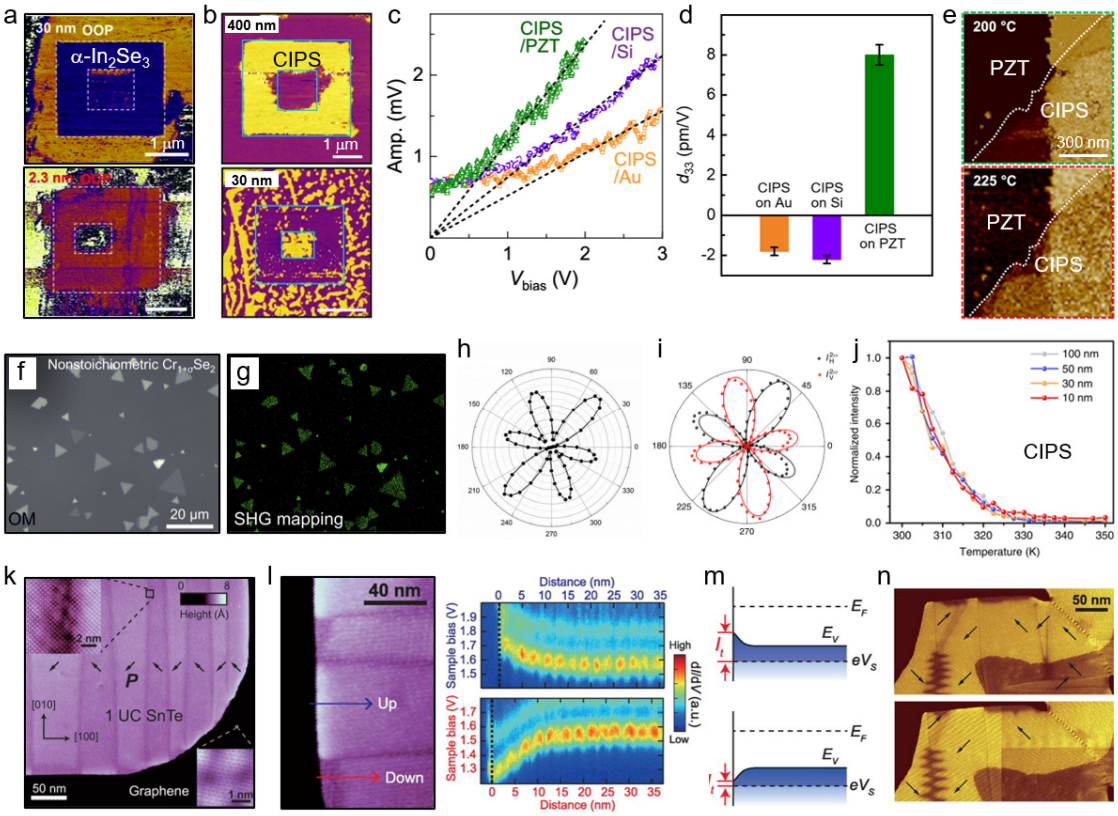


**Figure 11.** Characterizations of 2D ferroelectrics. (a) PFM phase images of domains written in α-$In_2Se_3$ flakes. (b) PFM phase images of domains written in CIPS flakes. (c) PFM amplitude *vs* $V_{bias}$ for 14 nm CIPS on PZT, doped Si, and Au. (d) $d_{33}$ for 14 nm CIPS on PZT, doped Si, and Au. (e) *In situ* PFM phase images of 13 nm CIPS on PZT with prepatterned domains at 200°C (top) and 225°C (bottom). (f-g) Optical image (f) and SHG mapping (g) of nonstoichiometric $Cr_{1+\sigma}Se_2$ (σ: intercalated metal atoms) triangular nanoflakes. (h-j) SHG characterizations of CIPS. (h) Polar plot of SHG intensity parallel to light polarization as a function of crystal angle. (i) Polar plots of SHG intensity along horizontal and vertical directions (lab coordinates) *vs* light polarization. (j) Temperature dependence of SHG intensity. (k-n) STM characterizations of 1 UC SnTe films. (k) STM image of SnTe on graphene with (upper inset) topography image across a DW and (lower inset) close-up view of graphene substrate. (l) STM image (left) and spatially resolved d*I*/d*V* spectra (right) close to edges with opposite polarization. (m) Schematic of in-plane polarization induced band bending. (n) STM images of SnTe film before (top) and after (bottom) a positive voltage pulse. (a) Adapted figures with

permission from [35]. Copyright © 2018 WILEY-VCH Verlag GmbH & Co. KGaA, Weinheim. (b) Adapted figures cited from [24]. Copyright © 2016, The Author(s). (c-e) Adapted figures with permission from [105]. Copyright © 2023 American Chemical Society. (f-g) Reprinted figures cited from [213]. Copyright © 2023, The Author(s). (h-j) Adapted figures cited from [24]. Copyright © 2016, The Author(s). (k-n) Reprinted figure with permission from [42]. Copyright © 2016, The American Association for the Advancement of Science.

SHG is the lowest order nonlinear optical response based on light-matter interaction and can be generated by non-centrosymmetric materials. Its sensitivity to inversion symmetry breaking in crystalline and electronic structures makes it highly effective for probing polar or magnetic order in nanomaterials. For example, Rogée *et al*. revealed the out-of-plane ferroelectricity in untwisted $MoS_2/WS_2$ bilayer arising from broken symmetry and interlayer sliding and studied the broken centrosymmetry using SHG [214]. The intensity of SHG emission depends on the interlayer angle between $MoS_2$ and $WS_2$, resulting in stark differences in intensity between the 3R and 2H-like stacking modes. SHG mapping images can serve as a high throughput tool for assessing emergent polar properties. For example, it has been used to identify sliding and defect-engineered piezoelectricity and ferroelectricity in nonstoichiometric TMDs that are nominally centrosymmetric (**Fig. 11f**) [213]. Liu *et al*. first probed the crystal structural symmetry associated with ferroelectricity in CIPS via SHG [24]. The SHG intensity as a function of the crystal structure shows the six-lobe pattern, revealing the hexagonal symmetry of the shifted Cu and In sublattices in CIPS in the ferroelectric phase (**Fig. 11g**). The polarized SHG as a function of excitation light polarization shows four-lobe symmetry that marks the noncentrosymmetric point group *m* of the system (**Fig. 11h**). The temperature dependence of SHG intensity reveals that the ferroelectric Cure temperature ($T_C$) of CIPS is close to 330 K and does no vary significantly with flake thickness between 10 and 100 nm (**Fig. 11i**).

STM is a sensitive tool for resolving atomic-scale structural features [215] and domain structures [216] of 2D ferroelectric materials. This approach detects the tunneling current between a sharp tip and the sample, which varies exponentially with the distance between the atoms of the tip and sample surface, providing topography information with atomic resolution. The ferroelectric behavior can be uncovered at the nanoscale by identifying the crystal symmetry and structural phase boundaries via STM. STM has been conducted to investigate and control ferroelectricity in various 2D materials, including the characterization and switching of the ferroelectric order in β-$In_2Se_3$ [39], observation of the in-plane ferroelectricity of β'-$In_2Se_3$ with a $T_C$ of 200 ºC [217], investigation of ferroelectricity and ferroelectric domain switching in monolayer phosphorus-like α-phase Bi [218], and manipulation and control of ferroelectric domains in monolayer SnSe [54] and SnTe [43]. Chang *et al*. reported a systematic STM study of ferroelectricity in SnTe film, which reveals the stripe domain structure and the associated lattice distortion in a one unit-cell (UC) SnTe film along the [010] direction (**Fig. 11j**) [42]. The edges of different in-plane polarizations are charged, resulting in opposite bending direction, which is confirmed by spatially resolved d$I$/d$V$ spectra (**Fig. 11k-l**). The domains of SnTe have also been manipulated by applying local voltage pulses via the STM tip (**Fig. 11m**).

### 3.2 Characterization of 2D Magnets

It is challenging to characterize 2D magnetism via conventional magnetometry such as the superconducting quantum interference device (SQUID) and vibrating sample magnetometry, which rely on having sufficient mass of the magnetic materials. The commonly used techniques for probing 2D magnetism include magnetotransport, magneto-optic effect (MOKE), reflective magnetic circular dichroism (RMCD), magnetic force microscopy (MFM), nitrogen vacancy (NV)

magnetometry, Lorentz transmission electron microscopy (TEM), scanning transmission x-ray microscopy (STXM), photoemission electron microscopy (PEEM), and Raman spectroscopy.

Magnetotransport is one of the most accessible characterization techniques for probing the magnetic state of nanoscale conducting systems. Various Hall effects, including anomalous Hall effect (AHE), planar Hall effect, quantum Hall effect, and quantum AHE, and magnetoresistance (MR), including longitudinal MR, anisotropic MR, and tunneling MR, can be used to identify the magnetic Curie temperature $T_C$ or Néel temperature $T_N$, coercive field ($H_c$), and magnetic anisotropy [219, 220]. For conductive 2D magnets, AHE is among the most common means of obtaining hysteresis loops in exfoliated samples [91, 93, 95]. Leveraging the Berry phase effect associated with the broken time-reversal symmetry, the amplitude of AHE signal also provides information about the out-of-plane magnetization [221]. For example, the competing magnetic orders in $Fe_3GeTe_2$ have been studied by combining AHE and MR measurements [91]. AHE has been used to systematically explore the layer-number-dependence of magnetic hysteresis, giving insight into how flake thickness affects the magnetic anisotropy [95]. May *et al.* used temperature-dependent AHE hysteresis to confirm the magnetic order in an exfoliated $Fe_5GeTe_2$ flake and identified a $T_C$ of about 280 K (**Fig. 12a-b**) [94].

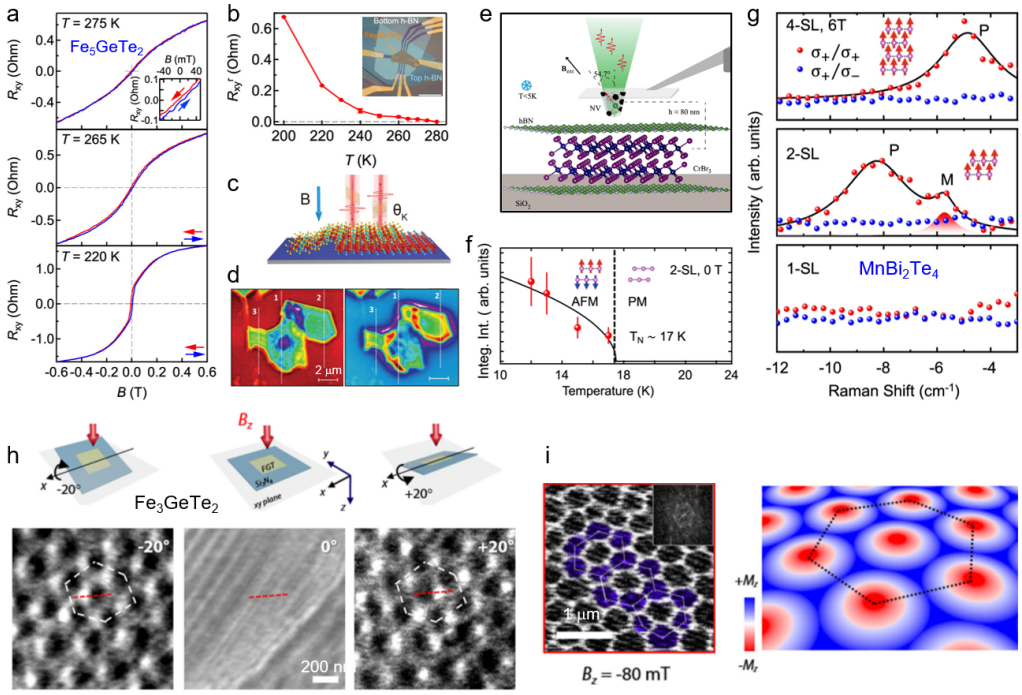


**Figure 12.** Characterizations of 2D magnets. (a-b) AHE in 28 nm $Fe_3GeTe_2$. (a) AHE hysteresis at various temperatures. (b) Temperature dependence of AHE signals with (inset) optical device image. Scale bar: 20 μm. (c) Schematic MOKE setup. (d) AFM (left) and MFM (right) images of an exfoliated $CrCl_3$ flakes on Si. (e) Schematic NV magnetometry setup. (f-g) Raman studies of $MnBi_2Te_4$ samples. (f) Temperature dependence of integrated Raman intensity in a 2-SL sample. (g) Raman spectra for 4-SL, 2-SL, and 1-SL samples. (h-i) Images of skyrmion lattice in $Fe_3GeTe_2$. (h) Lorentz TEM image at $B_z = -40$ mT and $T = 160$ K after field cooling at different tilting angles with respect to $x$ axis. (i) STXM image at $B_z = -80$ mT (left) with (inset) the fast-Fourier transform image and (right) schematic of the skyrmion lattice. The hexagonal unit cell of the skyrmion lattice is outlined. (a-b) Adapted figures with permission from [94]. Copyright © 2019, American Chemical Society. (c) Reprinted figure with permission from [222]. Copyright © 2020 Wiley-VCH GmbH. (d) Adapted figures with permission from [223]. Copyright © 2020 WILEY-VCH Verlag GmbH & Co. KGaA, Weinheim. (e) Adapted figure cited from [81]. Copyright © 2021, The Author(s). (f-g) Adapted figures cited from [224]. Copyright © 2022, The Author(s). (h-i) Adapted figures with permission from [225]. Copyright (2021) by the American Physical Society.

Optical techniques such as MOKE and RMCD have been extensively used to characterize magnetic thin films [226]. **Figure 12c** shows the schematic setup for MOKE measurements [222]. When light is reflected from a magnetic surface, it experiences a rotation in polarization and change in intensity, which is analogous to the Faraday effect for transmitted light [227]. The rotation in polarization plane in a MOKE signal (the Kerr angle $\theta_K$) is directly proportional to sample magnetization parallel to the beam. For example, MOKE measurements have been used to probe magnetism in the magnetic 2D $Cr_2Ge_2Te_6$ [22] and $CrI_3$ [23]. Magnetic circular dichroism detects the different absorption between left and right circularly polarized light induced by sample magnetization parallel to the light propagation direction, and the RMCD technique has been applied to probe the out-of-plane magnetization of bilayer $CrI_3$ *[69]*.

Scanning probe-based techniques such as MFM and scanning NV-magnetometry can visualize magnetic domains and DWs at the nanoscale. MFM detects the magnetic interaction between a magnetized cantilever and the sample. **Figure 12d** shows the MFM images taken on an exfoliated $CrCl_3$ flake with different thicknesses, which reveals spontaneous domain formation [223]. **Figure 12e** illustrate the schematic setup of NV-magnetometry [81], which is among the newly developed methods for exploring 2D magnets [228-230]. It exploits the spin-triplet ground state in the negatively charged NV in diamond to detect magnetic fields with high sensitivity at the nanoscale. NV-sensing can be integrated with scanning probe microscopy (*e.g.*, AFM), where an NV-center is implanted near the apex of a diamond nano-pillar probe. NV-magnetometry can achieve spatial resolution much higher than optical methods: depending on the distance between defect and sample, the resolution is usually on the order of tens of nanometers. It can be used to detect stray fields at the sample surface to deduce the magnetization distribution of a 2D flake. The ability to accurately measure the size and shape of nano-domains can also provide insight into the magnetic

anisotropy of the sample. Compared with techniques such as MOKE and MFM, the NV magnetometry can reveal quantitative information of local magnetization [231] and provide vector mapping of magnetic structures [232]. For example, NV-magnetometry has been used to study layer-dependent magnetism in $CrI_3$ and quantify sample magnetization in various regions [231]. The application of NV-magnetometry to 2D materials is a rising field, with commercial systems becoming available in recent years.

Electron and x-ray microscopy techniques have been widely used to resolve magnetic domains and spin textures in 2D magnets. Lorentz TEM provides phase information of spin orientation, which can be used to resolve spin textures such as skyrmion in 2D magnets [233]. It is based on TEM and exploits the deflection of the electron beam due to the Lorentz force exerted by sample magnetization to generate contrast in an image. This method can provide nanoscale resolution for visualizing spin orientations and has been used to study skyrmion lattices. Owing to their 2D nature, layered 2D magnets are readily compatible with this method. For example, Lorentz TEM has successfully been used to image domain structures and skyrmions in both $Fe_3GeTe_2$ [87, 225, 234, 235] and $Cr_2Ge_2Te_6$ [236], providing valuable insight into the formation and dynamics of topological spin textures in 2D magnets. **Figure 12h** shows the Lorentz TEM images of quasistatic Néel-type skyrmion lattices in $Fe_3GeTe_2$, where the phase information of the spin texture is clearly illustrated by tilting the sample [225]. Scanning transmission x-ray microscopy (**Figure 12i**) [225] and PEEM [85] have also been exploited to visualize the magnetic domains and skyrmion lattices in $Fe_3GeTe_2$ with high spatial resolution.

In addition to being a critical tool for standard structural characterization, Raman spectroscopy can also be used to study magnetism in 2D materials. Magnetic phase changes in a material are often associated with subtle structural changes as well. Such interactions can result in spin-phonon

coupling, which allows indirect coupling between magnetic behavior and the Raman response [235]. Consequently, magnons can be detected using Raman measurements [224, 237, 238]. Signatures of magnetic behaviors in the Raman spectra include the emergence of a new peak beneath the $T_C$, shifting and splitting of a peak in a magnetic field due to Zeeman splitting, and changes in the polar Raman symmetry. Raman spectroscopy has also been used to explore spin-phonon coupling related to skyrmions [239]. Raman hysteresis loops can be extracted by measuring the intensity of a certain peak as a function of magnetic field. Using polarized Raman spectroscopy, detailed information about spin-phonon coupling and magnon modes present in a sample can be obtained by controlling the chirality of the incident light and applying selection rules [237, 240]. Lujan *et al.* reported magnons and spin fluctuations in magnetic $MnBi_2Te_4$ flakes via magneto-Raman measurements (**Fig. 12g**), which show that the magnon mode only appears in the two septuple layer (SL) sample [224]. From the temperature dependence of the Raman intensity, $T_N$ of 17.5 K is deduced (**Fig. 12f**).

## 4. Progress in van der Waals Ferroics

### 4.1 2D Ferroelectrics

A variety of 2D vdW materials have been reported possessing ferroelectricity, with their electronic behaviors spanning from insulators to semiconductors and semi-metals. The vdW nature of interlayer interaction also enables artificially engineered ferroelectricity. Notable examples include ferroelectricity achieved by changing the stacking order between 2D layers with lateral shifts or twisted angles [15, 17, 171-176]. It is of rising research interests to explore the physical mechanisms underlying 2D ferroelectricity and harness their capabilities in novel nanoelectronic applications, such as ferroelectric FETs, NC FETs, ferroelectric tunnel junctions, and memristors for nonvolatile memory, energy-efficient logic, and neuromorphic applications [2]. **Table 2**

provides a comprehensive summary of representative 2D vdW ferroelectrics, including their polarization direction, $T_C$, and synthesis methods.

**Table 2.** Representative 2D ferroelectrics with their properties and synthesis methods.

| Materials | Polarization | $T_C$ | Synthesis Methods |
|---|---|---|---|
| **$CuInP_2S_6$** | OOP | 315 K (bulk) [241] | CVT and ME [20, 24-27, 66, 134, 135]; LPE [160] |
| **$CuCrP_2S_6$** | OOP | 190 K (bulk) [242] | ME [29-31, 243] |
| **$In_2Se_3$** | Intercorrelated OOP & IP | > 473 K (bulk) [2] | ME [33-37, 136, 217, 244]; LPE [159]; ECE [169, 170]; MBE [39, 190, 191, 217]; CVD [33, 183]; PVT [33, 183] |
| **SnTe** | IP | 98 K (bulk) [2]<br>270 K (1L) [42] | MBE [42, 43]; PVT [44] |
| **SnS** | IP | 800 K (bulk) [2]<br>> RT (1L) [45] | LPE [245, 246]; MBE [46]; CVD [51, 247, 248]; PVT [45-50, 185, 188, 249] |
| **SnSe** | IP | ~337 K (~41.4 nm) [250] | ME [251, 252]; LPE [253]; MBE [54, 254]; CVD [255]; PVT [53, 250] |
| **GeS** | IP | > RT (FL) [55] | ME [55, 256]; LPE [257]; CVD [258, 259]; PVT [56, 207, 260] |
| **GeSe** | IP | > 700 K (30 nm) [58] | ME [58, 261]; LPE [262, 263]; PVT [109] |
| **GaSe** | OOP & IP | > RT (14 nm) [264] | ME [264]; MBE [265, 266]; CVD [267] |
| **1T'-$MoTe_2$** | OOP | > RT (1L) [59] | ME [59, 107]; CVD [60] |
| **1T'-$WTe_2$** | OOP | > 300 K (bulk) [2]<br>350 K (2-3L) [61] | ME [61-63] |
| **$NbOI_2$** | OOP | > RT (82 nm) [65] | CVT and ME [60, 64, 66] |

OOP: out-of-plane. IP: in-plane. *n*L: *n*-layer. FL: few-layer. RT: room temperature. ME: mechanical exfoliation. LPE: liquid phase exfoliation. ECE: electrochemistry exfoliation.

CIPS is one of the most studied vdW ferroelectric materials due to its relative large bandgap, large out-of-plane polarization, and above room temperature $T_C$ [2]. The majority of studies on CIPS is based on mechanical exfoliation. Bulk CIPS crystals are typically synthesized using the chemical vapor transport method (**Fig. 13a**) [135], which is one of the most used techniques for producing high-quality bulk crystals. In this process, a stoichiometric mixture of Cu, In, P, and S (in a 1:1:2:6 ratio) serves as the precursor. All the powders are sealed in an evacuated silica tube and heated to 600 °C for two weeks. Air stable CIPS single crystals are subsequently formed in the tubes. **Figure 13b** shows the X-ray diffraction (XRD) scan of CIPS samples prepared with CVT ,

which shows a single crystalline structure with space group of $C_C$, and flakes exfoliated from the CVT sample show clear layered structure and smooth terraces (**Fig. 13c**) [135]. The exfoliated CIPS flakes can be transferred to different base layers for further engineering their ferroelectricity. For example, Wang *et al.* showed that the interfacial synergy between CIPS and ferroelectric oxide PZT promotes polar alignment in ultrathin CIPS flakes (**Fig. 13d-f**) and enhanced $T_C$ (**Fig. 11e**), which have been attributed to lattice distortion induced tilting of the quadruple well [105]. Liu *et al.* showed that laying CIPS flakes on a corrugated surface can lead to spontaneous DW motion and investigated the effects of curvature and stress on the ferroelectric energy profile [134].

Another extensively studied 2D ferroelectric is α-$In_2Se_3$, which possesses both out-of-plane and in-plane components of polarization and intercorrelated switching [41]. Ferroelectricity was initially reported experimentally in exfoliated thin α-$In_2Se_3$ samples, and the polarization is switchable in flakes with thickness down to 10 nm [33]. The exfoliated α-$In_2Se_3$ samples show spontaneous ferroelectric domains [244]. Exfoliated α-$In_2Se_3$ can be further integrated with other 2D materials, forming functional heterostructures. **Figure 13g** shows the high resolution scanning TEM (STEM) image of an h-BN/α-$In_2Se_3$ heterojunction, which can be used to develop ultra-fast ferroelectric memory and neural computing [136]. Element mapping (**Fig. 13g**) and Raman spectra (**Fig. 13h**) have been used to analyze the chemical and structural properties of the α-$In_2Se_3$ samples, and PFM measurements have been utilized to characterize the polarization switching hysteresis (**Fig. 13i**) [136] and assess the in-plane polarization [41] in exfoliated α-$In_2Se_3$ flakes. Unlike CIPS, domain writing via c-AFM can have precise control of polarization reversal and yield sharp DWs in α-$In_2Se_3$ (**Fig. 11a**) [35, 136, 244].

Besides CIPS and α-$In_2Se_3$, other ferroelectric materials such as $CuCrP_2S_6$ [29-31, 243], SnSe [251, 252], GeS [55, 256], GeSe [134], 1T'-$MoTe_2$ [59, 107], 1T'-$WTe_2$ [61-63], GaSe [264], and

$NbOI_3$ [64-66] have also been prepared using the mechanical exfoliation method. Specifically, single crystal synthesis followed by mechanical exfoliation can provide fast experimental input to theoretical material search of novel 2D ferroelectrics [65, 268].

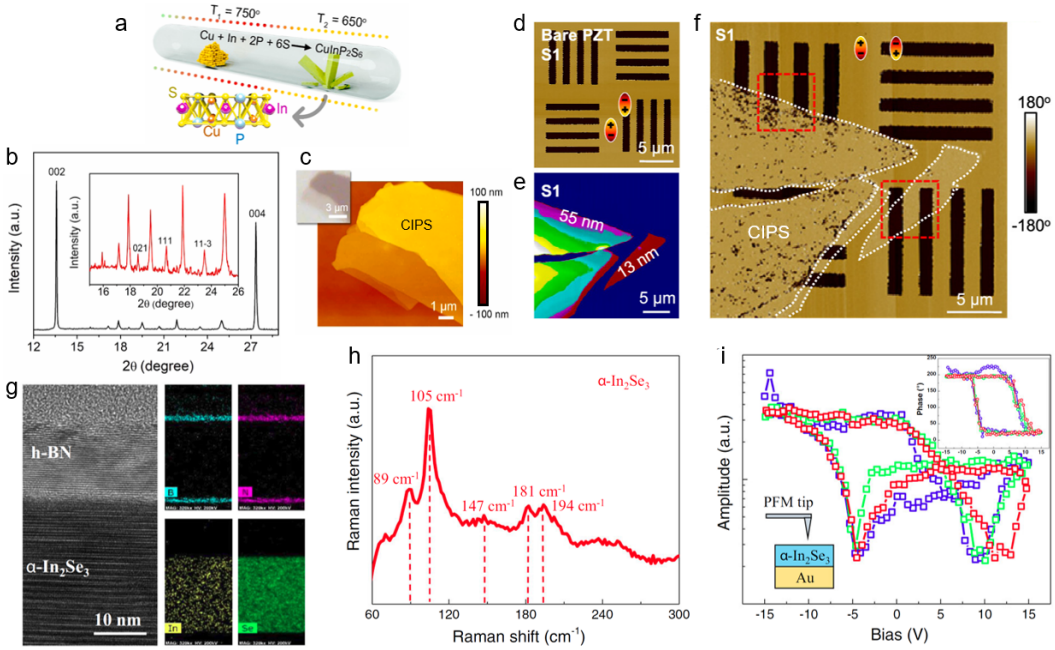


**Figure 13.** 2D ferroelectrics prepared via mechanical exfoliation from CVT samples. (a) Schematic of CVT growth of CIPS crystals. (b) XRD of CVT CIPS on $Si/SiO_2$. (c) AFM topology and (inset) optical images of exfoliated CIPS flakes. (d-f) PFM study of CIPS on PZT. (d) PFM phase image of bare PZT with prepatterned domains. (e) AFM and (f) PFM phase images of the same area with CIPS transferred on top. (g-i) Characterizations of exfoliated CVT $\alpha$-$In_2Se_3$. (g) STEM and element mapping of an h-BN/$\alpha$-$In_2Se_3$ heterojunction. (h) Raman spectra of $\alpha$-$In_2Se_3$ flake suggesting hexagonal structure. (i) PFM amplitude and (top inset) phase hysteresis loops taken on 40 nm $\alpha$-$In_2Se_3$, with (bottom inset) schematic setup. (a-c) Adapted figures with permission from [135]. Copyright © 2019 Elsevier Ltd. All rights reserved. (d-f) Adapte figures with permission from [105]. Copyright © 2023, American Chemical Society. (g-i) Reprinted figures cited from [136]. Copyright © 2021, The Author(s).

Notable progress has been made in vapor deposition of 2D vdW ferroelectrics. For example, high-quality $\alpha$-$In_2Se_3$ flakes have been synthesized via both PVT [39, 190, 191, 217] and CVD

[42, 43]. Triangular-shaped α-$In_2Se_3$ flakes down to monolayer thickness have been obtained utilizing $In_2Se_3$ powder as the precursor, and the lateral size of the flakes has reached about 10 μm (**Fig. 14a-c**) [183]. Large α-$In_2Se_3$ flakes with about 50 μm lateral sizes have been deposited on mica substrates using $In_2O_3$ and Se powders in a $H_2$/Ar mix gas environment (**Fig. 14d-g**) [269].

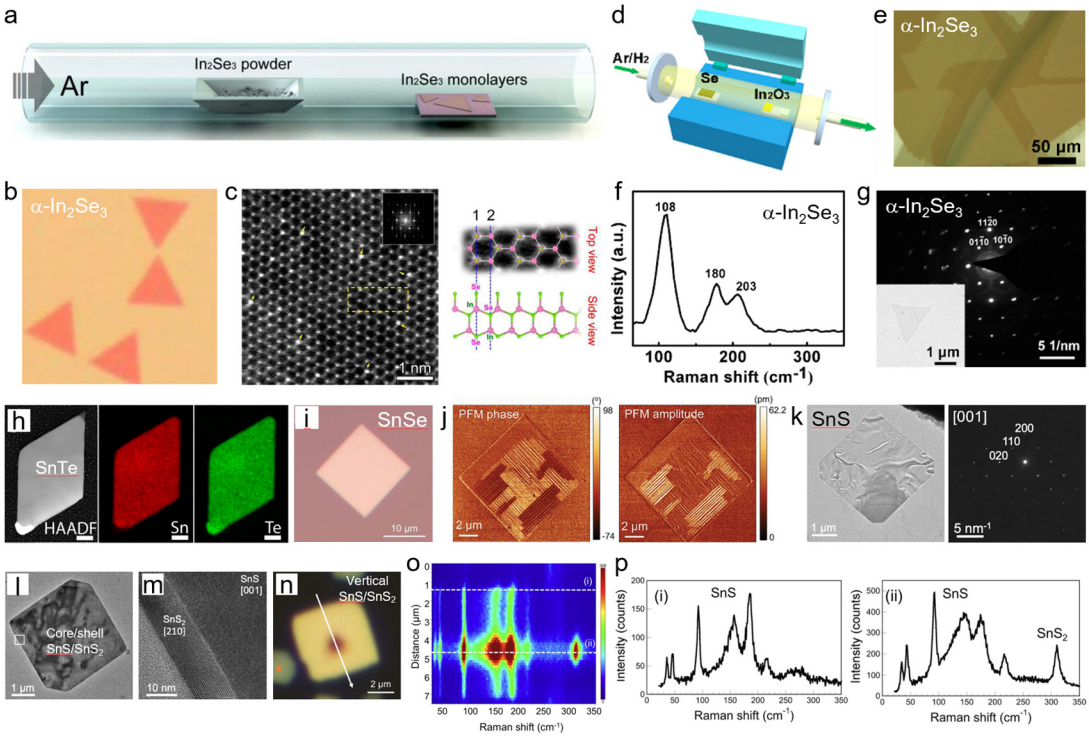


**Figure 14.** 2D ferroelectrics prepared via vapor depositions. (a-c) PVT α-$In_2Se_3$. (a) Schematic growth setup. (b) Optical image. (c) High resolution TEM image with (inset) diffraction pattern and (lower right) schematic crystal structure. (d-g) CVD α-$In_2Se_3$. (d) Schematic growth setup. (e) Optical image. (f) Raman spectrum of an as-grown flake thicker than 5 nm. (g) Diffraction pattern with (inset) TEM image. (h) STEM image (left) with elemental mapping of Sn (middle) and Te (right) taken on PVT SnTe samples. (i-j) PVT SnSe. (i) Optical image. (j) PFM phase (left) and amplitude (right) images. (k) TEM image of a PVT-grown SnS flake (left) with DP (right). (l-p) One-step CVD-grown SnS/$SnS_2$ core/shell and vertical heterostructures. (l) TEM image of SnS/$SnS_2$ core/shell heterostructure, with (m) high-resolution TEM image of the boxed area. (n) Optical image of SnS/$SnS_2$ vertical heterostructure, with (o) Raman spectra along the solid arrow. (p) Raman spectra taken at the edge (i) and center (ii) of

the sample, marked as the dashed lines in (o). (a-c) Adapted figures with permission from [183]. Copyright © 2015, American Chemical Society. (d-g) Adapted figures with permission from [269]. Copyright © 2016, American Chemical Society. (h) Adapted figures with permission from [44]. Copyright © 2014, American Chemical Society. (i-j) Adapted figures cited from [53]. Copyright © 2023 The Authors. Advanced Electronic Materials published by Wiley-VCH GmbH. (k-p) Adapted figures with permission from [185]. Copyright © 2020, American Chemical Society.

After the discovery of the ferroelectricity in group IV monochalcogenides, significant progress has been made to the vapor deposition of this class of materials, including SnTe [44] (**Fig. 14h**), SnSe [53, 250] (**Fig. 14i**), SnS [45, 185, 188, 249] (**Fig. 14k**), GeS [207], and GaSe [267]. Shen *et al*. pioneered the synthesis of SnTe nanoplates using the PVT method (**Fig. 14h**) [44]. These nanoplates were cultivated on $SiO_2$/Si substrates at temperatures ranging from 300 to 450 °C in an argon atmosphere, employing vapor-liquid-solid and vapor-solid mechanisms. This process yielded nanoplates with lateral dimensions of tens of microns and thicknesses around a hundred nanometers. Notably, the crystalline orientation of these nanoplates depends on the growth substrate temperature: (100) nanoplates and nanoribbons are prevalent at 350-450 °C, while (111) nanoplates and nanoribbons dominate at around 300 °C. These nanoplates, with either (100) or (111) surface orientations, are optimal for maximizing topological surface states [44]. Chiu *et al*. reported reliable PVT growth of 2D SnSe flakes (**Fig. 14i**) [53]. The PFM amplitude and phase maps of the as-grown SnSe flake show spontaneous formation of in-plane ferroelectric domains (**Fig. 14j**). Sutter *et al.* have achieved PVT and CVD growth of a range of group IV monochalcogenides, including SnS flakes [185], GeS flakes [207], SnS/$SnS_2$ core/shell heterostructures [185, 188], SnS/$SnS_2$ vertical heterostructures [185], and SnS/GeS lateral heterostructures [207]. The SnS flakes are in the orthorhombic structure and have quasi-square shapes (**Fig. 14k**) [185]. The SnS/$SnS_2$ core/shell heterostructures (**Fig. 14l**) show similar shapes

as the single-phase SnS flakes (**Fig. 14k**) [185, 188]. However, high-resolution TEM clearly reveals several nanometres thick $SnS_2$ (about 10 atomic layers) at the edge of the flake (**Fig. 14m**) [185, 188]. The SnS/$SnS_2$ vertical heterostructures have been synthesized by incorporating extra sulfur during growth (**Fig. 14n**) [185]. Raman spectra confirms that $SnS_2$ layers form on the top of the SnS flake in the center area (**Fig. 14o-p**) [185].

Recently, MBE has been exploited to successfully synthesize a range of two-element vdW ferroelectrics, including $In_2Se_3$ with different phases (**Fig. 15a-b**) [39, 190, 191, 217], SnTe (**Fig. 11j-m**) [42, 43], SnS (**Fig. 15c-e**) [46], SnSe [54] (**Fig. 15f-i**), and GaSe [265, 266]. Bao *et al.* reported layer-by-layer MBE growth of thin SnS samples with robust in-plane ferroelectricity (**Fig. 15c-e**) [46]. PFM studies reveal the presence of the ferroelectric domains (**Fig. 15d**). The odd-even layer effect on ferroelectric polarization in SnS further confirms the effect of inversion symmetry breaking (**Fig. 15e**). MBE growth can also facilitate *in situ* STM studies. Chang *et al.* synthesized monolayer SnSe flakes with robust in-plane ferroelectricity (**Fig. 145**) and manipulated the ferroelectric domains by applying a bias voltage pulse to the STM tip (**Fig. 15g-i**) [54].

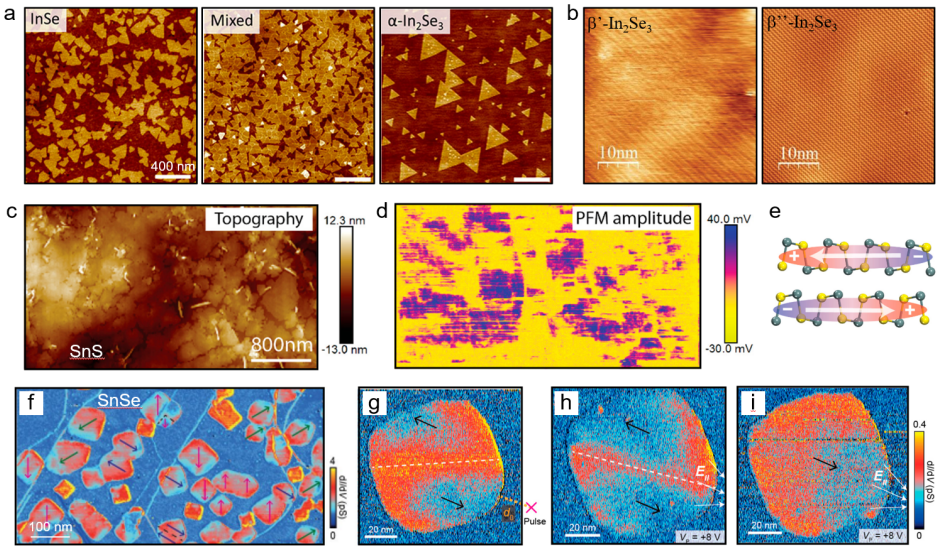


**Figure 15.** 2D ferroelectrics prepared via MBE. (a) AFM topography images of InSe (left), mix of InSn and α-$In_2Se_3$ (middle), and α-$In_2Se_3$ (left). (b) STM image of β'-$In_2Se_3$ (left) and β''-$In_2Se_3$ (right). (c-

e) MBE-grown SnS. (c) AFM topography image. (d) PFM amplitude image. (e) schematic of ferroelectric order in SnS. (f-i) STM study of MBE-grown SnSe. (f) STM resolved d$I$/d$V$ mapping of SnSe flakes with different in-plane polarization directions. (g-i) d$I$/d$V$ mapping of a monolayer SnSe upon sequential ferroelectric switching. (a) Adapted figures with permission from [190]. Copyright © 2018, American Chemical Society. (b) Adapted figures cited from [191]. Copyright © 2021 The Authors. Advanced Science published by Wiley-VCH GmbH. (c-e) Adapted figures with permission from [46]. Copyright © 2019, American Chemical Society. (f-i) Adapted figures with permission from [54]. Copyright © 2020, American Chemical Society.

### 4.2 2D Magnets

A growing family of magnetic 2D materials has been synthesized and explored in recent years [4, 130, 270-272]. These materials exhibit diverse electronic and topological states, encompassing insulators, semiconductors, conductors, and topological insulators, and the host magnetic behaviors ranging from ferromagnetism [22, 72, 73, 86, 273], ferrimagnetism [178, 179, 274, 275], and antiferromagnetism [23, 72-74, 76]. Additionally, magnetic homo- and heterostructures can be constructed through stacking or direct growth of magnetic multilayers, which can potentially lead to distinct magnetic orders compared with the parent materials and give rise to emergent phenomena such as majorana edge modes [80] and noncollinear spin textures [12, 14]. **Table 3** provides a comprehensive summary of representative 2D vdW magnets, including their magnetic order, $T_C$ or $T_N$, and synthesis methods.

**Table 3.** Representative 2D magnets with their properties and synthesis methods.

| Materials | Magnetic Order | Spin model (Anisotropy) | $T_C$ or $T_N$ | Synthesis Methods |
|---|---|---|---|---|
| **$Cr_2Ge_2Te_6$** | FM | Heisenberg (PMA) | $T_C$ = 40 K (bilayer), and 66 K (FL) [22] | ME [22, 276, 277] |
| **$CrI_3$** | A-type AFM (FL)<br>FM (1L) | Ising (PMA) | $T_N$ = 45 K (1L) [23]<br>$T_N$ = 47 K (FL) [72, 73]; | ME [23, 69-73, 231]; MBE [278]; CVT [133] |

| | | | | |
|---|---|---|---|---|
| **$CrBr_3$** | FM | Between Ising and Heisenberg (PMA) | $T_C$ = 37 K (FL) [72, 73]; | ME [72, 73]; MBE [77, 79, 80]; CVT [133] |
| **$CrCl_3$** | A-type AFM (FL) FM (1L) | XY (IMA) | $T_N$ = 17 K (FL) [72-74, 76]; | ME [72, 73, 76]; MBE [193]; CVT [133]; PVT [74] |
| **α-$RuCl_3$** | Zigzag-type AFM | | $T_N$ = 7-8 K (1-3L) [279] | ME [279]; MBE [280]; CVT [281] |
| **$Fe_3GeTe_2$** | FM | Ising (PMA) | $T_C$ = 120 K (3L), and 145 K (4L) [86, 273] | ME [85-87, 273]; MBE [88, 89, 282] |
| **$MnPS_3$** | Néel-type AFM | Ising (PMA) | $T_N$ = 78 K (FL) [283] | ME [117, 283] |
| **$FePS_3$** | Zigzag-type AFM | Ising (PMA) | $T_N$ = ~118 K (thickness independence) [284] | ME [284, 285] |
| **$VSe_2$** | FM | (IMA) | $T_C$ = 470 K (FL) [286] | MBE [79, 83, 287]; CVD [84, 288] |
| **$CrSe_2$** | FM | | $T_C$ = 15 K (1L), and 110 K (16L) [289] | MBE [290]; CVD [289] |
| **1T-$CrTe_2$** | FM | (PMA) | $T_C$ =~187-212 K (~130 nm to ~7.5 nm) [291] | ME [292]; MBE [293-295]; CVD [291] |
| **$MnBi_2Te_4$** | A-type AFM | (PMA) | $T_N$ = 23 K (5L), 21 K (4L), and 18 K (3L) [296] | ME [224, 296]; MBE [98, 99] |

FM: ferromagnetic. AFM: antiferromagnetic. PMA: perpendicular magnetic anisotropy. IMA: in-plane magnetic anisotropy.

Mechanical exfoliated $Cr_2Ge_2Te_6$ [22] and $CrI_3$ [23] flakes are the first 2D materials that have been shown to persist magnetic orders down to atomic thickness. Since then, a wide range of 2D vdW magnets have been successfully exfoliated from bulk crystals, and their magnetic properties have been investigated via magnetotransport, magneto-optical, Raman spectroscopy, electron microscopy, and scanning probe techniques (**Fig. 16**). For example, the ferromagnetic properties of few-layer $Cr_2Ge_2Te_6$ were investigated using MOKE [22]. The temperature-dependent Kerr signals indicate that $T_C$ of $Cr_2Ge_2Te_6$ varies with flake thickness, with thinner flakes displaying lower $T_C$ values. For regions thicker than 4 layers, the sample exhibits strong MOKE signal at 40 K. In the bilayer region, on the other hand, strong MOKE signal emerges at much lower temperature.

The ferromagnetic order in monolayer to FL $CrI_3$ has been identified via magneto-optical and magnetotransport studies [23, 69-73]. The MOKE signal of a monolayer flake shows a single hysteresis loop, suggesting that monolayer $CrI_3$ exhibits ferromagnetism, while the bilayer flake shows vanishing signal at magnetic fields up to 0.65 T, indicating antiferromagnetic order [23]. Tunneling MR of FL $CrX_3$ has been studied in graphite/$CrX_3$/graphite tunnel junctions (**Fig. 16a**) [69-74]. For a bilayer $CrI_3$ junction, the tunneling current remains constant at low perpendicular magnetic fields and exhibits a sharp, step-like increase when reaching a critical magnetic field value (**Fig. 16b**) [69]. This sharp switching of current points to a spin-flip transition in perpendicular magnetic field, which lowers the tunnel barrier for spin aligned with the magnetic field. Such type of transition is consistent with the RMCD (**Fig. 16c**) and the earlier MOKE results [23], revealing perpendicular magnetic anisotropy in $CrI_3$. Thiel *et al.* have imaged the magnetic domains in 1-9 layer $CrI_3$ flakes via scanning single-spin magnetometry based on diamond NV centers and discovered a puncture-induced magnetic transition from antiferromagnetic to ferromagnetic interlayer ordering in FL $CrI_3$, which has been attributed to a monoclinic to rhombohedral structural transition (**Fig. 16d**) [231].

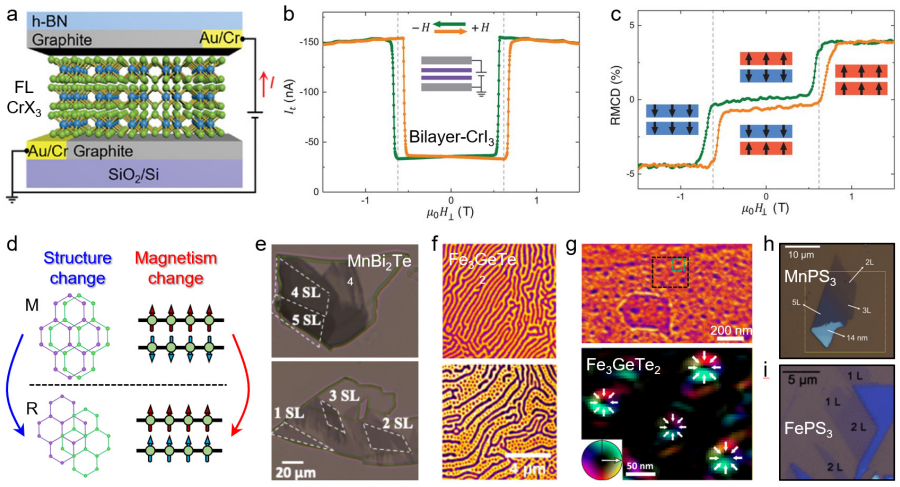


**Figure 16.** 2D magnets prepared via mechanical exfoliation. (a) Schematic of a graphite/$CrX_3$/graphite tunnel junction. (b) Tunneling current *I* and (c) RMCD signature as functions of perpendicular magnetic

field taken on a FL graphene/bilayer $CrI_3$/FL graphene junction. (d) Schematic of structural change induced magnetic phase transition in bilayer $CrI_3$. (e) Optical images of exfoliated $MnBi_2Te_4$ flakes. (f) PEEM images of 130 nm $Fe_3GeTe_2$ flakes on 16 nm (top) and 1.5 nm (bottom) Pd. (g) Lorentz TEM image (top) and expanded view of the boxed area (bottom) taken on 70 nm $Fe_3GeTe_2$ on $(Co/Pd)_{10}$. (h) Optical image of a $MnPS_3$ flake with different thicknesses. (i) Optical image of $FePS_3$ flakes. (a) Adapted figure cited from [74]. Copyright © 2022 The Authors. Advanced Science published by Wiley-VCH GmbH. (b-c) Adapted figures with permission from [69]. Copyright © 2018, The American Association for the Advancement of Science. (e) Adapted figures cited from [224]. Copyright © 2022, The Author(s). (f-g) Adapted figures cited from [85]. Copyright © 2020 The Authors, some rights reserved, exclusive licensee American Association for the Advancement of Science. (h) Adapted figure cited from [117]. Copyright © 2019 IOP Publishing Ltd. (i) Adapted figure with permission from [285]. Copyright © 2016, American Chemical Society.

Both bulk single crystals and exfoliated flakes of $Fe_3GeTe_2$ have been investigated. Deng *et al.* have isolated $Fe_3GeTe_2$ thin flakes via the advanced exfoliation method with the assistance of $Al_2O_3$ layer [86]. This method is easier to obtain ultrathin samples than the conventional exfoliation method [224, 296] (**Fig. 16e**). It has been shown that sample thickness and interfacial layers have critical influences on the characteristic magnetic domain structures or spin textures in $Fe_3GeTe_2$. Ding *et al.* has reported the Bloch-type magnetic skyrmion bubbles in bulk single crystals of $Fe_3GeTe_2$ [87]. Lorentz TEM studies show that strip magnetic domains in 167 nm thick $Fe_3GeTe_2$ samples transform into skyrmion bubble patterns in a perpendicular magnetic field. PEEM studies of 130-150 nm $Fe_3GeTe_2$ flakes on Pd reveal predominant strip domains in samples on thick (16 nm) Pd and coexistence of magnetic bubble domains when the Pd thickness is reduced to 5 and 1.5 nm (**Fig. 16f**). Lorentz TEM studies show the emergence of Néel-type skyrmions in 70 nm $Fe_3GeTe_2$ on $(Co/Pd)_{10}$ substrates (**Fig. 16g**) [85].

Other 2D magnets such as $MnPS_3$ [117] and $FePS_3$ [285] have also been prepared with mechanical exfoliation, with large isolated flakes obtained (**Fig. 16h-i**). Raman spectroscopic studies have been performed on $MnPS_3$ to examine the thickness-dependence of magnetic phase transition, and stable magnetic order has been observed in bilayer samples [117].

To date, direct vapor phase deposition approach has been successfully utilized to synthesize various 2D magnets, and progress has been made in acquiring ultrathin samples with uniform thickness and large size. For example, highly crystalline $CrI_3$, $CrBr_3$, and $CrCl_3$ samples were initially synthesized on yttrium stabilized zirconia (YSZ) substrates via CVT [133]. Most of the samples are thicker than 100 nm, with only a small fraction of the flakes thinner than 10 nm (**Fig. 17a-b**). Recently, Wang *et al.* have reported direct PVT growth of thin $CrCl_3$ flakes down to monolayer thickness with well-defined shapes on HOPG and mica substrates (**Fig. 8c**) and characterized the magnetic properties using graphite/FL $CrCl_3$/graphite tunnel junctions [74]. **Figure 17c** shows the tunneling MR of a 6-layer $CrCl_3$ junction at 2 K and 17 K. At 2 K, the tunneling current increases gradually with perpendicular magnetic field and saturates at 2.5 T. Compared to the sharp current switching associated with spin-flip transition in $CrI_3$ (**Fig. 17b**) [69], the spins in $CrCl_3$ continuously rotate in magnetic field, pointing to an in-plane magnetic anisotropy [74]. At 17 K, the tunneling current shows a weaker field dependence and does not saturate up to 6 T, showing that the sample is approaching $T_N$.

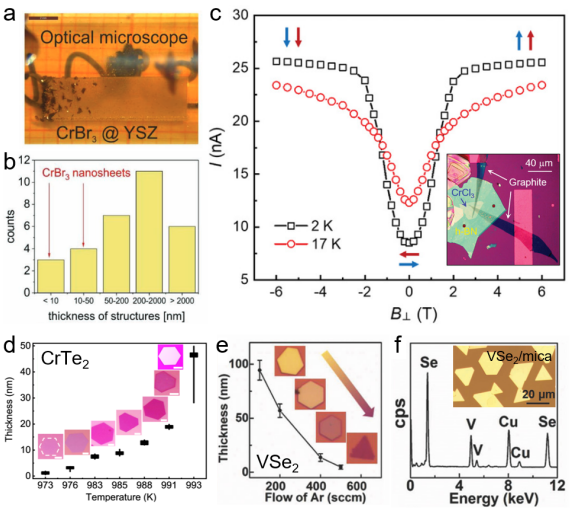


**Figure 17.** 2D magnets grown via vapor phase deposition. (a) Optical image of $CrBr_3$ grown on YSZ substrate, with (b) thickness histogram. (c) Tunneling current *I vs B* of a 6-layer $CrCl_3$-based tunnel junction. Inset: Optical image of the device. (d) $CrTe_2$ flake thickness as a function of growth temperature, with (inset) corresponding optical images. (e) $VSe_2$ flakes thickness as a function of Ar flow rate, with (inset) corresponding optical images. (f) TEM stoichiometry analysis of $VSe_2$ on Cu grid. Inset: Optical image of as-grown $VSe_2$ on mica substrate. (a-b) Reprinted figure cited from [133]. Copyright © 2018 The Authors. Published by WILEY-VCH Verlag GmbH & Co. KGaA, Weinheim. (c) Adapted figures cited from [74]. Copyright © 2022 The Authors. Advanced Science published by Wiley-VCH GmbH. (d) Adapted figure cited from [291]. Copyright © 2021, The Author(s). (e-f) Adapted figure with permission from [288]. Copyright © 2017 WILEY-VCH Verlag GmbH & Co. KGaA, Weinheim.

Ultrathin $CrSe_2$ flakes have been successfully synthesized via CVD using $CrCl_3$ and Se precursors [289]. Monolayer $CrSe_2$ flakes are formed on dangling-bond-free $WSe_2$ layers, supporting that vdW-type substrates facilitate horizontal growth. The thickness of $CrSe_2$ flakes depends sensitively on the growth temperature. Reducing the growth temperature from 720 to 700 °C decreases the average flake thickness from 10 to 4 nm, which has been attributed to the enhanced surface energy. RMCD studies show that monolayer samples exhibit a soft hysteresis

loop with the hysteresis window disappeared at 50 K, while the 16-layer sample shows a square hysteresis that persists above 100 K, indicating robust perpendicular magnetic anisotropy.

The CVD growth of 2D magnet $CrTe_2$ also depends highly on the growth temperature (**Fig. 17d**) [291]. Hexagonal $CrTe_2$ flakes have been synthesized on bare $SiO_2/Si$ substrate using $CrCl_2$ and Te precursors. Decreasing the growth temperature from 993 to 973 K reduces drastically the average flake thickness from 47.9 to 1.2 nm. The thickness of $CrSe_2$ can also be tuned by introducing $H_2$ process gas, with the thinnest flake achieved at $Ar/H_2$ flow rate of 200 sccm/10 sccm.

High quality $VSe_2$ flakes were successfully synthesized via CVD in 2017 [288], while magnetism in $VSe_2$ was first reported in MBE samples in 2018 [83]. **Figure 17e** illustrates tuning of $VSe_2$ flake thickness via the carrier gas flow [288]. The sample thickness decreases from about 90 to 4.9 nm as the Ar flow increases from 500 to 100 sccm. The CVD samples of $VSe_2$ possess large lateral dimensions (tens of microns) with high uniformity (**Fig. 17e-f**). Recent MFM studies of CVD-grown $VSe_2$ flakes show high magnetic phase contrast and domain formation in flakes thinner than 2 nm, pointing to above room temperature ferromagnetism [84]. The MFM signal becomes gradually weaker with increasing flake thickness and diminishes in sample thicker than 6 nm, suggesting the change of magnetic anisotropy or $T_C$.

MBE has been exploited to achievable controllable growth of a wide range of 2D magnets, including $Fe_3GeTe_2$ (**Fig. 18a**) [88, 89, 282], $MnBi_2Te_4$ (**Fig. 18b**) [98, 99], $VSe_2$ (**Fig. 18c**) [83, 287], $CrI_3$ (**Fig. 18d**) [278], $CrBr_3$ (**Fig. 18e**) [77, 79, 80], $CrCl_3$ [193], $RuCl_3$ [280], and $CrTe_2$ (**Fig. 18f**) [293-295]. Epitaxial growth of 2D magnets on a vdW substrate can naturally lead to vertical heterostructures with 2D/2D interfaces. For example, Kezilebieke *et al*. reported epitaxial growth of ferromagnetic $CrBr_3$ on 2D superconducting $NbSe_2$ substrate (**Fig. 17e**), and the $CrBr_3$

samples show ferromagnetic ordering with out-of-plane magnetic anisotropy down to monolayer thickness [79, 80]. MBE-grown samples enable the *in situ* STM characterizations without been exposed to air, which is critical for the study of moisture-sensitive 2D magnets such as $CrX_3$. For example, low-temperature STM imagining reveals 1D majorana edge modes in monolayer $CrBr_3$ on $NbSe_2$ [80].

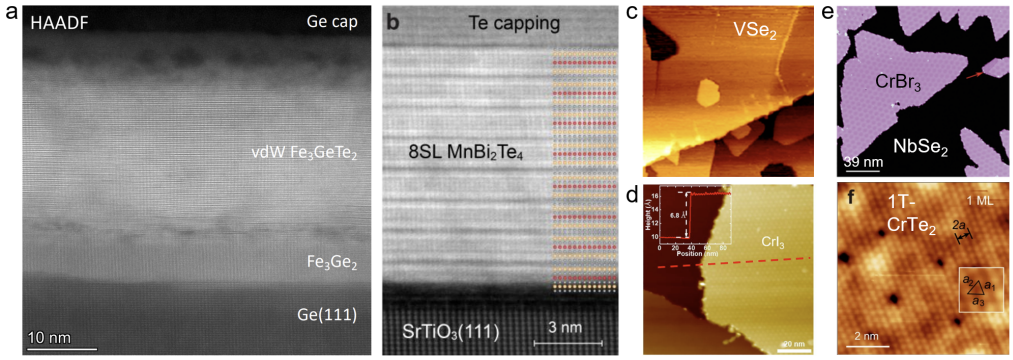


**Figure 18.** 2D magnets prepared via MBE. (a) STEM image of $Fe_3GeTe_2/Fe_3Ge_2$ grown on (111) Ge. (b) STEM image of $MnBi_2Te_4$ film grown on (111) $SrTiO_3$. (c) STM image of $VSe_2$ flakes on HOPG. (d) STM image of $CrI_3$ flakes on (111) Au with (inset) the height profile along the dashed line. (e) STM image of a monolayer $CrBr_3$ grown on $NbSe_2$ crystal. (f) STM image of monolayer 1T-$CrTe_2$ with (inset) an expanded view of 1 $nm^2$ area. (a) Reprinted figure with permission from [282]. Copyright © 2022, American Chemical Society. (b) Reprinted figure with permission from [98]. Copyright © 2022, American Chemical Society. (c) Reprinted figure with permission from [287]. Copyright © 2019, American Chemical Society. (d) Adapted figure with permission from [278]. Copyright © 2020 Elsevier Ltd. All rights reserved. (e) Adapted figure cited from [79]. Copyright © 2021 The Authors. Advanced Materials published by Wiley-VCH GmbH. (f) Adapted figure cited from [293]. Copyright © 2022, The Author(s).

## 5. Challenges and Future Directions

Despite the tremendous progress in the discovery of new 2D ferroic materials and heterostructures and the design and understanding of various emergent phenomena, several key

challenges remain in the material synthesis. In this section, we discuss the challenges in synthesizing 2D vdW ferroic materials and heterostructures, including high throughput, scalable growth, quality control, and deterministic creation of heterostructures, and future directions for developing effective top-down and bottom-up synthesis methods.

### 5.1 Challenges

**High throughput synthesis**: Recent advances in data-driven computational discovery, particularly enabled by density functional theory (DFT) combined with machine learning, have facilitated the high throughput prediction of 2D ferroic materials [65, 268, 297-300]. In contrast to the large numbers of materials that are theoretically predicted to exhibit ferroelectricity or magnetism at atomic layers, experimental verification remains limited. It is thus instrumental to develop high throughput synthesis techniques that can bridge the gap between theoretical predictions and experimental studies.

**Scalable Growth**: Current synthesis methods for 2D ferroic materials primarily occur within laboratory settings, while the production of cost-effective wafer-scale samples remains challenging. Encouraging developments have been made in other 2D materials, such as CVD-grown wafer-scale graphene [301], h-BN [302], and $WS_2$ [303]. Advancing industrial-compatible vapor deposition techniques for 2D ferroics is critical for developing their technological applications [304].

**Stability of 2D ferroics, particularly 2D magnets**: Ambient stability and environmental reactions pose significant challenges in 2D ferroics research, particularly for magnetic materials. Many 2D magnets are prone to degradation when exposed to air, moisture, and thermal fluctuations, demanding specialized preparation methods such as glovebox environments or encapsulation layers to maintain their integrity [69, 72-74, 76]. These constraints limit their practical applications.

Recently, air-stable 2D magnets have been synthesized, including $Cr_5Te_8$ [181], 1T-$CrTe_2$ [291], and $CrSe_2$ [289]. Synthesis of more air stable 2D magnets or finding solutions to streamline encapsulation or enhance air stability is essential for expanding their applicability and enabling broader exploration of their intrinsic properties.

### 5.2 Development Trends and Future Directions

**Top-down methods**: With the development of computational material search, it is expected that there will be rapid expansion of the repertoire for 2D ferroic bulk crystals available for exfoliating isolated thin flakes and synthesizing customized heterostructures. While mechanical exfoliation has proven invaluable for the initial exploration and fundamental understanding of 2D ferroic materials, it has built-in limitations associated with contamination from tape residue, low yield, small sample sizes, and uncontrollable flake shapes. It is thus of enormous interest to refine the mechanical exfoliation technique for achieving contamination-free, scalable, and high-uniformity production of 2D ferroic materials. Efforts have been made towards optimizing the exfoliation parameters, tape and substrate selections, and substrate surface treatment (*e.g.*, via UV ozone) to reduce tape residue, increase yield, and enhance reproducibility of thin flakes. The development of automated exfoliation systems can streamline the process and minimize human intervention, leading to more consistent results and increased throughput. Liquid and electrochemical exfoliation techniques can be further developed for high throughput sample preparation in conjunction with the discovery with new vdW ferroics that are insensitive to moisture, and the key challenge is to optimize conditions for achieving low-defect, high-quality samples with high uniformity.

**Bottom-up methods:** For vapor phase deposition, efforts to enhance sample quality and yield involve optimizing growth parameters, exploring novel precursor materials, and developing

innovative growth techniques to minimize defects and improve crystalline quality. Techniques such as MOCVD and ALD are promising for synthesizing large-scale vdW thin films with excellent uniformity and crystal quality, while their implementation in 2D ferroic growth remains to be further developed. It is also of interest to advance vapor deposition methods for epitaxial growth and *in situ* property characterization, which are conventionally expected for MBE growth. In addition, streamline the vapor phase deposition, pre-growth substrate and post-growth sample treatments, heterostructure construction, and *in situ* characterization in a gas-environment-controlled apparatus can offer avenues for enhancing material/interface qualities and exploring intrinsic material properties, especially for 2D magnets that are sensitive to air and moisture.

For MBE, the growth complexity increases substantially with the number of elements in the compound. Efforts to expand the range of viable materials and heterostructures involve exploring alternative source materials and substrate combinations, as well as exploring the parameter space for *in situ* tuning of sample composition, polymorphs, and material types. Recent development of MBE and laser MBE based remote epitaxial growth of complex oxide membranes such as $SrTiO_3$ [305] and $BaTiO_3$ [306] on substrates buffered with patterned graphene points to a new route for achieving high quality interfaces between functional oxides and vdW materials. It is conceivable that similar approach can be applied to vdW ferroic buffered substrates to create novel 2D/3D heterostructures with tailored functionalities.

**Creation of multifunctional heterostructures and integration with semiconductor technology**: Expanding the scope of 2D research and applications involves the creation of functional 2D ferroic heterostructures. The 2D/2D interfaces can host emergent phenomena such as charge-transfer [289], magnetoelectric coupling [11], spin-dependent tunneling [69, 72-74], and topological spin textures [307-310]. For example, giant tunneling MR has been realized in FL

graphene/$CrI_3$/graphene heterostructures [61], and a long-retention FeFET has been built based on CIPS/graphene/h-BN/$MoS_2$ heterostructure [311]. Integration of 2D ferroics with ferroelectric and piezoelectric oxides and polymers can further expand the property tuning capacities and introduce new coupling mechanisms [107, 312-314]. Scalable synthesis of high quality and even epaxial 2D/2D [314] and 2D/3D interfaces [315] between 2D ferroics and other functional materials can facilitate the exploration of various interfacial synergies and develop novel device concepts [113, 316, 317]. Looking forward, 3D monolithic integration of these 2D ferroic heterostructures with conventional semiconductor technology can promote the implementation of for developing high performance, energy-efficient electronics, spintronics, and neuromorphic computing [2, 304].

**Acknowledgements:**

We would like to thank Yinjie Guo and Kai Huang for technical support. This work is supported by the National Science Foundation through Grant No. DMR-2118828 and EPSCoR RII Track-1: Emergent Quantum Materials and Technologies (EQUATE), Award No. OIA-2044049, the UNL Grand Challenges catalyst award entitled Quantum Approaches addressing Global Threats, and the Nebraska Center for Energy Sciences Research.

**Conflict of Interest:**

The authors have no conflicts to disclose.

**References:**


[1] M. H. Wu, and P. Jena, The rise of two-dimensional van der Waals ferroelectrics, Wiley Interdiscip. Rev.-Comput. Mol. Sci. **8**, e1365 (2018).

[2] H. Ryu, K. Xu, D. Li, X. Hong, and W. Zhu, Empowering 2D nanoelectronics via ferroelectricity, Applied Physics Letters **117**, 080503 (2020).

[3] J. Chu, Y. Wang, X. Wang, K. Hu, G. Rao, C. Gong, C. Wu, H. Hong, X. Wang, K. Liu, C. Gao, and J. Xiong, 2D Polarized Materials: Ferromagnetic, Ferrovalley, Ferroelectric Materials, and Related Heterostructures, Advanced Materials **33**, 2004469 (2021).

[4] Q. H. Wang, A. Bedoya-Pinto, M. Blei, A. H. Dismukes, A. Hamo, S. Jenkins, M. Koperski, Y. Liu, Q.-C. Sun, E. J. Telford, H. H. Kim, M. Augustin, U. Vool, J.-X. Yin, L. H. Li, A. Falin, C. R. Dean, F. Casanova, R. F. L. Evans, M. Chshiev, A. Mishchenko, C. Petrovic, R. He, L. Zhao, A. W. Tsen, B. D. Gerardot, M. Brotons-Gisbert, Z. Guguchia, X. Roy, S. Tongay, Z. Wang, M. Z. Hasan, J. Wrachtrup, A. Yacoby, A. Fert, S. Parkin, K. S. Novoselov, P. Dai, L. Balicas, and E. J. G. Santos, The Magnetic Genome of Two-Dimensional van der Waals Materials, ACS Nano **16**, 6960 (2022).

[5] Z. Guan, H. Hu, X. Shen, P. Xiang, N. Zhong, J. Chu, and C. Duan, Recent Progress in Two-Dimensional Ferroelectric Materials, Advanced Electronic Materials **6**, 1900818 (2020).

[6] S. Jiang, L. Li, Z. Wang, K. F. Mak, and J. Shan, Controlling magnetism in 2D $CrI_3$ by electrostatic doping, Nature Nanotechnology **13**, 549 (2018).

[7] L. Webster, and J.-A. Yan, Strain-tunable magnetic anisotropy in monolayer $CrCl_3$, $CrBr_3$, and $CrI_3$, Physical Review B **98**, 144411 (2018).

[8] Z. Wu, J. Yu, and S. Yuan, Strain-tunable magnetic and electronic properties of monolayer $CrI_3$, Physical Chemistry Chemical Physics **21**, 7750 (2019).

[9] Y. Lu, R. Fei, X. Lu, L. Zhu, L. Wang, and L. Yang, Artificial Multiferroics and Enhanced Magnetoelectric Effect in van der Waals Heterostructures, ACS Applied Materials & Interfaces **12**, 6243 (2020).

[10] Y. Su, X. Li, M. Zhu, J. Zhang, L. You, and E. Y. Tsymbal, Van der Waals Multiferroic Tunnel Junctions, Nano Letters **21**, 175 (2021).

[11] X. Jin, A. O'Hara, Y.-Y. Zhang, S. Du, and S. T. Pantelides, Designing strong and tunable magnetoelectric coupling in 2D trilayer heterostructures, 2D Materials **10**, 015007 (2023).

[12] K. Huang, D.-F. Shao, and E. Y. Tsymbal, Ferroelectric Control of Magnetic Skyrmions in Two-Dimensional van der Waals Heterostructures, Nano Letters **22**, 3349 (2022).

[13] T. Song, Q.-C. Sun, E. Anderson, C. Wang, J. Qian, T. Taniguchi, K. Watanabe, M. A. McGuire, R. Stöhr, D. Xiao, T. Cao, J. Wrachtrup, and X. Xu, Direct visualization of magnetic domains and moiré magnetism in twisted 2D magnets, Science **374**, 1140 (2021).

[14] H. C. Xie, X. P. Luo, Z. P. Ye, Z. L. Sun, G. H. Ye, S. H. Sung, H. W. Ge, S. H. Yan, Y. Fu, S. J. Tian, H. C. Lei, K. Sun, R. Hovden, R. He, and L. Y. Zhao, Evidence of non-collinear spin texture in magnetic moire superlattices, Nature Physics **19**, 1150 (2023).

[15] A. Weston, E. G. Castanon, V. Enaldiev, F. Ferreira, S. Bhattacharjee, S. Xu, H. Corte-León, Z. Wu, N. Clark, A. Summerfield, T. Hashimoto, Y. Gao, W. Wang, M. Hamer, H. Read, L. Fumagalli, A. V. Kretinin, S. J. Haigh, O. Kazakova, A. K. Geim, V. I. Fal'ko, and R. Gorbachev, Interfacial ferroelectricity in marginally twisted 2D semiconductors, Nature Nanotechnology **17**, 390 (2022).

[16] K. Huang, E. Schwartz, D.-F. Shao, A. A. Kovalev, and E. Y. Tsymbal, Magnetic antiskyrmions in two-dimensional van der Waals magnets engineered by layer stacking, Physical Review B **109**, 024426 (2024).
[17] K. Yasuda, X. Wang, K. Watanabe, T. Taniguchi, and P. Jarillo-Herrero, Stacking-engineered ferroelectricity in bilayer boron nitride, Science **372**, 1458 (2021).
[18] L. Gogoi, W. B. Gao, P. M. Ajayan, and P. Deb, Quantum magnetic phenomena in engineered heterointerface of low-dimensional van der Waals and non-van der Waals materials, Physical Chemistry Chemical Physics **25**, 1430 (2023).
[19] H. Wang, Y. Wen, H. Zeng, Z. R. Xiong, Y. Y. Tu, H. Zhu, R. Q. Cheng, L. Yin, J. Jiang, B. X. Zhai, C. S. Liu, C. X. Shan, and J. He, 2D Ferroic Materials for Nonvolatile Memory Applications, Advanced Materials **n/a**, 2305044 (2024).
[20] A. Belianinov, Q. He, A. Dziaugys, P. Maksymovych, E. Eliseev, A. Borisevich, A. Morozovska, J. Banys, Y. Vysochanskii, and S. V. Kalinin, $CuInP_2S_6$ Room Temperature Layered Ferroelectric, Nano Letters **15**, 3808 (2015).
[21] J. Feder, Two dimensional ferroelectricity, Ferroelectrics **12**, 71 (1976).
[22] C. Gong, L. Li, Z. Li, H. Ji, A. Stern, Y. Xia, T. Cao, W. Bao, C. Wang, Y. Wang, Z. Q. Qiu, R. J. Cava, S. G. Louie, J. Xia, and X. Zhang, Discovery of intrinsic ferromagnetism in two-dimensional van der Waals crystals, Nature **546**, 265 (2017).
[23] B. Huang, G. Clark, E. Navarro-Moratalla, D. R. Klein, R. Cheng, K. L. Seyler, D. Zhong, E. Schmidgall, M. A. McGuire, D. H. Cobden, W. Yao, D. Xiao, P. Jarillo-Herrero, and X. Xu, Layer-dependent ferromagnetism in a van der Waals crystal down to the monolayer limit, Nature **546**, 270 (2017).
[24] F. Liu, L. You, K. L. Seyler, X. Li, P. Yu, J. Lin, X. Wang, J. Zhou, H. Wang, H. He, S. T. Pantelides, W. Zhou, P. Sharma, X. Xu, P. M. Ajayan, J. Wang, and Z. Liu, Room-temperature ferroelectricity in $CuInP_2S_6$ ultrathin flakes, Nature Communications **7**, 12357 (2016).
[25] M. Si, P.-Y. Liao, G. Qiu, Y. Duan, and P. D. Ye, Ferroelectric Field-Effect Transistors Based on $MoS_2$ and $CuInP_2S_6$ Two-Dimensional van der Waals Heterostructure, ACS Nano **12**, 6700 (2018).
[26] M. Si, A. K. Saha, P.-Y. Liao, S. Gao, S. M. Neumayer, J. Jian, J. Qin, N. Balke Wisinger, H. Wang, P. Maksymovych, W. Wu, S. K. Gupta, and P. D. Ye, Room-Temperature Electrocaloric Effect in Layered Ferroelectric $CuInP_2S_6$ for Solid-State Refrigeration, ACS Nano **13**, 8760 (2019).
[27] D.-D. Xu, R.-R. Ma, A.-P. Fu, Z. Guan, N. Zhong, H. Peng, P.-H. Xiang, and C.-G. Duan, Ion adsorption-induced reversible polarization switching of a van der Waals layered ferroelectric, Nature Communications **12**, 655 (2021).
[28] Z. Zhao, K. Xu, H. Ryu, and W. Zhu, Strong Temperature Effect on the Ferroelectric Properties of $CuInP_2S_6$ and Its Heterostructures, ACS Applied Materials & Interfaces **12**, 51820 (2020).
[29] W. F. Io, S. Y. Pang, L. W. Wong, Y. Zhao, R. Ding, J. Mao, Y. Zhao, F. Guo, S. Yuan, J. Zhao, J. Yi, and J. Hao, Direct observation of intrinsic room-temperature ferroelectricity in 2D layered $CuCrP_2S_6$, Nature Communications **14**, 7304 (2023).
[30] K. Cho, S. Lee, R. Kalaivanan, R. Sankar, K.-Y. Choi, and S. Park, Tunable Ferroelectricity in Van der Waals Layered Antiferroelectric $CuCrP_2S_6$, Advanced Functional Materials **32**, 2204214 (2022).

[31] Y. Lai, Z. Song, Y. Wan, M. Xue, C. Wang, Y. Ye, L. Dai, Z. Zhang, W. Yang, H. Du, and J. Yang, Two-dimensional ferromagnetism and driven ferroelectricity in van der Waals $CuCrP_2S_6$, Nanoscale **11**, 5163 (2019).
[32] P. Liu, Y. Li, D. Hou, H. Zhu, H. Luo, S. Zhou, L. Wei, W. Niu, Z. Sheng, W. Mao, and Y. Pu, Switchable diode effect in 2D van der Waals ferroelectric $CuCrP_2S_6$, Applied Physics Letters **124**, 091901 (2024).
[33] Y. Zhou, D. Wu, Y. Zhu, Y. Cho, Q. He, X. Yang, K. Herrera, Z. Chu, Y. Han, M. C. Downer, H. Peng, and K. Lai, Out-of-Plane Piezoelectricity and Ferroelectricity in Layered α-$In_2Se_3$ Nanoflakes, Nano Letters **17**, 5508 (2017).
[34] M. Si, A. K. Saha, S. Gao, G. Qiu, J. Qin, Y. Duan, J. Jian, C. Niu, H. Wang, W. Wu, S. K. Gupta, and P. D. Ye, A ferroelectric semiconductor field-effect transistor, Nature Electronics **2**, 580 (2019).
[35] F. Xue, W. Hu, K.-C. Lee, L.-S. Lu, J. Zhang, H.-L. Tang, A. Han, W.-T. Hsu, S. Tu, W.-H. Chang, C.-H. Lien, J.-H. He, Z. Zhang, L.-J. Li, and X. Zhang, Room-Temperature Ferroelectricity in Hexagonally Layered α-$In_2Se_3$ Nanoflakes down to the Monolayer Limit, Advanced Functional Materials **28**, 1803738 (2018).
[36] X. Tao, and Y. Gu, Crystalline–Crystalline Phase Transformation in Two-Dimensional $In_2Se_3$ Thin Layers, Nano Letters **13**, 3501 (2013).
[37] Y. Li, C. Chen, W. Li, X. Mao, H. Liu, J. Xiang, A. Nie, Z. Liu, W. Zhu, and H. Zeng, Orthogonal Electric Control of the Out-Of-Plane Field-Effect in 2D Ferroelectric α-$In_2Se_3$, Advanced Electronic Materials **6**, 2000061 (2020).
[38] Q. He, Z. Tang, M. Dai, H. Shan, H. Yang, Y. Zhang, and X. Luo, Epitaxial Growth of Large Area Two-Dimensional Ferroelectric α-$In_2Se_3$, Nano Letters **23**, 3098 (2023).
[39] Z. Zhang, J. Nie, Z. Zhang, Y. Yuan, Y.-S. Fu, and W. Zhang, Atomic Visualization and Switching of Ferroelectric Order in β-$In_2Se_3$ Films at the Single Layer Limit, Advanced Materials **34**, 2106951 (2022).
[40] W. Han, X. Zheng, K. Yang, C. S. Tsang, F. Zheng, L. W. Wong, K. H. Lai, T. Yang, Q. Wei, M. Li, W. F. Io, F. Guo, Y. Cai, N. Wang, J. Hao, S. P. Lau, C.-S. Lee, T. H. Ly, M. Yang, and J. Zhao, Phase-controllable large-area two-dimensional $In_2Se_3$ and ferroelectric heterophase junction, Nature Nanotechnology **18**, 55 (2023).
[41] C. Cui, W.-J. Hu, X. Yan, C. Addiego, W. Gao, Y. Wang, Z. Wang, L. Li, Y. Cheng, P. Li, X. Zhang, H. N. Alshareef, T. Wu, W. Zhu, X. Pan, and L.-J. Li, Intercorrelated In-Plane and Out-of-Plane Ferroelectricity in Ultrathin Two-Dimensional Layered Semiconductor $In_2Se_3$, Nano Letters **18**, 1253 (2018).
[42] K. Chang, J. W. Liu, H. C. Lin, N. Wang, K. Zhao, A. M. Zhang, F. Jin, Y. Zhong, X. P. Hu, W. H. Duan, Q. M. Zhang, L. Fu, Q. K. Xue, X. Chen, and S. H. Ji, Discovery of robust in-plane ferroelectricity in atomic-thick SnTe, Science **353**, 274 (2016).
[43] M. Amini, O. J. Silveira, V. Vaňo, J. L. Lado, A. S. Foster, P. Liljeroth, and S. Kezilebieke, Control of Molecular Orbital Ordering Using a van der Waals Monolayer Ferroelectric, Advanced Materials **35**, 2206456 (2023).
[44] J. Shen, Y. Jung, A. S. Disa, F. J. Walker, C. H. Ahn, and J. J. Cha, Synthesis of SnTe Nanoplates with {100} and {111} Surfaces, Nano Letters **14**, 4183 (2014).
[45] N. Higashitarumizu, H. Kawamoto, C.-J. Lee, B.-H. Lin, F.-H. Chu, I. Yonemori, T. Nishimura, K. Wakabayashi, W.-H. Chang, and K. Nagashio, Purely in-plane ferroelectricity in monolayer SnS at room temperature, Nature Communications **11**, 2428 (2020).

[46] Y. Bao, P. Song, Y. Liu, Z. Chen, M. Zhu, I. Abdelwahab, J. Su, W. Fu, X. Chi, W. Yu, W. Liu, X. Zhao, Q.-H. Xu, M. Yang, and K. P. Loh, Gate-Tunable In-Plane Ferroelectricity in Few-Layer SnS, Nano Letters **19**, 5109 (2019).
[47] P. Sutter, H. P. Komsa, H. Lu, A. Gruverman, and E. Sutter, Few-layer tin sulfide (SnS): Controlled synthesis, thickness dependent vibrational properties, and ferroelectricity, Nano Today **37**, 101082 (2021).
[48] M. J. Moody, J. T. Paul, P. J. M. Smeets, R. dos Reis, J.-S. Kim, C. E. Mead, J. T. Gish, M. C. Hersam, M. K. Y. Chan, and L. J. Lauhon, van der Waals Epitaxy, Superlubricity, and Polarization of the 2D Ferroelectric SnS, ACS Applied Materials & Interfaces **15**, 56150 (2023).
[49] Y.-R. Chang, R. Nanae, S. Kitamura, T. Nishimura, H. Wang, Y. Xiang, K. Shinokita, K. Matsuda, T. Taniguchi, K. Watanabe, and K. Nagashio, Shift-Current Photovoltaics Based on a Non-Centrosymmetric Phase in In-Plane Ferroelectric SnS, Advanced Materials **35**, 2301172 (2023).
[50] R. Moqbel, Y.-R. Chang, Z.-Y. Li, S.-H. Kung, H.-Y. Cheng, C.-C. Lee, K. Nagashio, and K.-H. Lin, Wavelength dependence of polarization-resolved second harmonic generation from ferroelectric SnS few layers, 2D Materials **10**, 015022 (2023).
[51] K. C. Kwon, Y. Zhang, L. Wang, W. Yu, X. Wang, I.-H. Park, H. S. Choi, T. Ma, Z. Zhu, B. Tian, C. Su, and K. P. Loh, In-Plane Ferroelectric Tin Monosulfide and Its Application in a Ferroelectric Analog Synaptic Device, ACS Nano **14**, 7628 (2020).
[52] R. Fei, W. Kang, and L. Yang, Ferroelectricity and Phase Transitions in Monolayer Group-IV Monochalcogenides, Physical Review Letters **117**, 097601 (2016).
[53] M.-H. Chiu, X. Ji, T. Zhang, N. Mao, Y. Luo, C. Shi, X. Zheng, H. Liu, Y. Han, W. L. Wilson, Z. Luo, V. Tung, and J. Kong, Growth of Large-Sized 2D Ultrathin SnSe Crystals with In-Plane Ferroelectricity, Advanced Electronic Materials **9**, 2201031 (2023).
[54] K. Chang, F. Küster, B. J. Miller, J.-R. Ji, J.-L. Zhang, P. Sessi, S. Barraza-Lopez, and S. S. P. Parkin, Microscopic Manipulation of Ferroelectric Domains in SnSe Monolayers at Room Temperature, Nano Letters **20**, 6590 (2020).
[55] Y. Yan, Q. Deng, S. Li, T. Guo, X. Li, Y. Jiang, X. Song, W. Huang, J. Yang, and C. Xia, In-plane ferroelectricity in few-layered GeS and its van der Waals ferroelectric diodes, Nanoscale **13**, 16122 (2021).
[56] R. R. Barreto, T. C. Ribeiro, G. H. R. Soares, E. Pereira, D. R. Miquita, G. A. M. Safar, M. S. C. Mazzoni, A. Malachias, and R. Magalhaes-Paniago, Evidence of thickness-dependent surface-induced ferroelectricity in few-layer germanium sulfide obtained via scanning tunneling spectroscopy, Nanoscale **16**, 5794 (2024).
[57] S. Guan, C. Liu, Y. Lu, Y. Yao, and S. A. Yang, Tunable ferroelectricity and anisotropic electric transport in monolayer β-GeSe, Physical Review B **97**, 144104 (2018).
[58] Z. Guan, Y. Zhao, X. Wang, N. Zhong, X. Deng, Y. Zheng, J. Wang, D. Xu, R. Ma, F. Yue, Y. Cheng, R. Huang, P. Xiang, Z. Wei, J. Chu, and C. Duan, Electric-Field-Induced Room-Temperature Antiferroelectric–Ferroelectric Phase Transition in van der Waals Layered GeSe, ACS Nano **16**, 1308 (2022).
[59] S. Yuan, X. Luo, H. L. Chan, C. Xiao, Y. Dai, M. Xie, and J. Hao, Room-temperature ferroelectricity in $MoTe_2$ down to the atomic monolayer limit, Nature Communications **10**, 1775 (2019).

[60] T. Ma, H. Chen, K. Yananose, X. Zhou, L. Wang, R. Li, Z. Zhu, Z. Wu, Q.-H. Xu, J. Yu, C. W. Qiu, A. Stroppa, and K. P. Loh, Growth of bilayer $MoTe_2$ single crystals with strong non-linear Hall effect, Nature Communications **13**, 5465 (2022).
[61] Z. Fei, W. Zhao, T. A. Palomaki, B. Sun, M. K. Miller, Z. Zhao, J. Yan, X. Xu, and D. H. Cobden, Ferroelectric switching of a two-dimensional metal, Nature **560**, 336 (2018).
[62] P. Sharma, F.-X. Xiang, D.-F. Shao, D. Zhang, E. Y. Tsymbal, A. R. Hamilton, and J. Seidel, A room-temperature ferroelectric semimetal, Science Advances **5**, eaax5080 (2019).
[63] S. C. de la Barrera, Q. Cao, Y. Gao, Y. Gao, V. S. Bheemarasetty, J. Yan, D. G. Mandrus, W. Zhu, D. Xiao, and B. M. Hunt, Direct measurement of ferroelectric polarization in a tunable semimetal, Nature Communications **12**, 5298 (2021).
[64] I. Abdelwahab, B. Tilmann, Y. Wu, D. Giovanni, I. Verzhbitskiy, M. Zhu, R. Berté, F. Xuan, L. d. S. Menezes, G. Eda, T. C. Sum, S. Y. Quek, S. A. Maier, and K. P. Loh, Giant second-harmonic generation in ferroelectric $NbOI_2$, Nature Photonics **16**, 644 (2022).
[65] Y. Wu, I. Abdelwahab, K. C. Kwon, I. Verzhbitskiy, L. Wang, W. H. Liew, K. Yao, G. Eda, K. P. Loh, L. Shen, and S. Y. Quek, Data-driven discovery of high performance layered van der Waals piezoelectric $NbOI_2$, Nature Communications **13**, 1884 (2022).
[66] C. Liu, X. Zhang, X. Wang, Z. Wang, I. Abdelwahab, I. Verzhbitskiy, Y. Shao, G. Eda, W. Sun, L. Shen, and K. P. Loh, Ferroelectricity in Niobium Oxide Dihalides $NbOX_2$ (X = Cl, I): A Macroscopic- to Microscopic-Scale Study, ACS Nano **17**, 7170 (2023).
[67] V. Gupta, T. M. Cham, G. M. Stiehl, A. Bose, J. A. Mittelstaedt, K. Kang, S. Jiang, K. F. Mak, J. Shan, R. A. Buhrman, and D. C. Ralph, Manipulation of the van der Waals Magnet $Cr_2Ge_2Te_6$ by Spin–Orbit Torques, Nano Letters **20**, 7482 (2020).
[68] M. Lohmann, T. Su, B. Niu, Y. Hou, M. Alghamdi, M. Aldosary, W. Xing, J. Zhong, S. Jia, W. Han, R. Wu, Y.-T. Cui, and J. Shi, Probing Magnetism in Insulating Cr2Ge2Te6 by Induced Anomalous Hall Effect in Pt, Nano Letters **19**, 2397 (2019).
[69] T. Song, X. Cai, M. W.-Y. Tu, X. Zhang, B. Huang, N. P. Wilson, K. L. Seyler, L. Zhu, T. Taniguchi, K. Watanabe, M. A. McGuire, D. H. Cobden, D. Xiao, W. Yao, and X. Xu, Giant tunneling magnetoresistance in spin-filter van der Waals heterostructures, Science **360**, 1214 (2018).
[70] Z. Wang, I. Gutiérrez-Lezama, N. Ubrig, M. Kroner, M. Gibertini, T. Taniguchi, K. Watanabe, A. Imamoğlu, E. Giannini, and A. F. Morpurgo, Very large tunneling magnetoresistance in layered magnetic semiconductor $CrI_3$, Nature Communications **9**, 2516 (2018).
[71] D. R. Klein, D. MacNeill, J. L. Lado, D. Soriano, E. Navarro-Moratalla, K. Watanabe, T. Taniguchi, S. Manni, P. Canfield, J. Fernández-Rossier, and P. Jarillo-Herrero, Probing magnetism in 2D van der Waals crystalline insulators via electron tunneling, Science **360**, 1218 (2018).
[72] H. H. Kim, B. Yang, S. Li, S. Jiang, C. Jin, Z. Tao, G. Nichols, F. Sfigakis, S. Zhong, C. Li, S. Tian, D. G. Cory, G.-X. Miao, J. Shan, K. F. Mak, H. Lei, K. Sun, L. Zhao, and A. W. Tsen, Evolution of interlayer and intralayer magnetism in three atomically thin chromium trihalides, Proceedings of the National Academy of Sciences **116**, 11131 (2019).
[73] H. H. Kim, B. Yang, S. Tian, C. Li, G.-X. Miao, H. Lei, and A. W. Tsen, Tailored Tunnel Magnetoresistance Response in Three Ultrathin Chromium Trihalides, Nano Letters **19**, 5739 (2019).

[74] J. Wang, Z. Ahmadi, D. Lujan, J. Choe, T. Taniguchi, K. Watanabe, X. Li, J. E. Shield, and X. Hong, Physical Vapor Transport Growth of Antiferromagnetic $CrCl_3$ Flakes Down to Monolayer Thickness, Advanced Science **10**, 2203548 (2023).
[75] M. A. McGuire, G. Clark, S. Kc, W. M. Chance, G. E. Jellison, V. R. Cooper, X. Xu, and B. C. Sales, Magnetic behavior and spin-lattice coupling in cleavable van der Waals layered $CrCl_3$ crystals, Physical Review Materials **1**, 014001 (2017).
[76] X. Cai, T. Song, N. P. Wilson, G. Clark, M. He, X. Zhang, T. Taniguchi, K. Watanabe, W. Yao, D. Xiao, M. A. McGuire, D. H. Cobden, and X. Xu, Atomically Thin $CrCl_3$: An In-Plane Layered Antiferromagnetic Insulator, Nano Lett **19**, 3993 (2019).
[77] W. Chen, Z. Sun, Z. Wang, L. Gu, X. Xu, S. Wu, and C. Gao, Direct observation of van der Waals stacking–dependent interlayer magnetism, Science **366**, 983 (2019).
[78] Y. Wu, M. Zhu, R. Zhao, X. Liu, J. Shen, H. Huang, S. Shen, L. Zhang, J. Zhang, X. Zheng, and S. Wang, Degradation Effect and Magnetoelectric Transport Properties in $CrBr_3$ Devices, Materials **15(9)**, 3007 (2022).
[79] S. Kezilebieke, O. J. Silveira, M. N. Huda, V. Vaňo, M. Aapro, S. C. Ganguli, J. Lahtinen, R. Mansell, S. van Dijken, A. S. Foster, and P. Liljeroth, Electronic and Magnetic Characterization of Epitaxial $CrBr_3$ Monolayers on a Superconducting Substrate, Advanced Materials **33**, 2006850 (2021).
[80] S. Kezilebieke, M. N. Huda, V. Vaňo, M. Aapro, S. C. Ganguli, O. J. Silveira, S. Głodzik, A. S. Foster, T. Ojanen, and P. Liljeroth, Topological superconductivity in a van der Waals heterostructure, Nature **588**, 424 (2020).
[81] Q.-C. Sun, T. Song, E. Anderson, A. Brunner, J. Förster, T. Shalomayeva, T. Taniguchi, K. Watanabe, J. Gräfe, R. Stöhr, X. Xu, and J. Wrachtrup, Magnetic domains and domain wall pinning in atomically thin $CrBr_3$ revealed by nanoscale imaging, Nature Communications **12**, 1989 (2021).
[82] W. Yu, J. Li, T. S. Herng, Z. Wang, X. Zhao, X. Chi, W. Fu, I. Abdelwahab, J. Zhou, J. Dan, Z. Chen, Z. Chen, Z. Li, J. Lu, S. J. Pennycook, Y. P. Feng, J. Ding, and K. P. Loh, Chemically Exfoliated $VSe_2$ Monolayers with Room-Temperature Ferromagnetism, Advanced Materials **31**, e1903779 (2019).
[83] M. Bonilla, S. Kolekar, Y. Ma, H. C. Diaz, V. Kalappattil, R. Das, T. Eggers, H. R. Gutierrez, M.-H. Phan, and M. Batzill, Strong room-temperature ferromagnetism in $VSe_2$ monolayers on van der Waals substrates, Nature Nanotechnology **13**, 289 (2018).
[84] W. Ci, H. Yang, W. Xue, R. Yang, B. Lv, P. Wang, R.-W. Li, and X.-H. Xu, Thickness-dependent and strain-tunable magnetism in two-dimensional van der Waals $VSe_2$, Nano Research **15**, 7597 (2022).
[85] M. Yang, Q. Li, R. V. Chopdekar, R. Dhall, J. Turner, J. D. Carlström, C. Ophus, C. Klewe, P. Shafer, A. T. N'Diaye, J. W. Choi, G. Chen, Y. Z. Wu, C. Hwang, F. Wang, and Z. Q. Qiu, Creation of skyrmions in van der Waals ferromagnet $Fe_3GeTe_2$ on (Co/Pd)n superlattice, Science Advances **6**, eabb5157.
[86] Y. Deng, Y. Yu, Y. Song, J. Zhang, N. Z. Wang, Z. Sun, Y. Yi, Y. Z. Wu, S. Wu, J. Zhu, J. Wang, X. H. Chen, and Y. Zhang, Gate-tunable room-temperature ferromagnetism in two-dimensional $Fe_3GeTe_2$, Nature **563**, 94 (2018).
[87] B. Ding, Z. Li, G. Xu, H. Li, Z. Hou, E. Liu, X. Xi, F. Xu, Y. Yao, and W. Wang, Observation of Magnetic Skyrmion Bubbles in a van der Waals Ferromagnet $Fe_3GeTe_2$, Nano Letters **20**, 868 (2020).

[88] S. Liu, X. Yuan, Y. Zou, Y. Sheng, C. Huang, E. Zhang, J. Ling, Y. Liu, W. Wang, C. Zhang, J. Zou, K. Wang, and F. Xiu, Wafer-scale two-dimensional ferromagnetic $Fe_3GeTe_2$ thin films grown by molecular beam epitaxy, npj 2D Materials and Applications **1**, 30 (2017).
[89] H. Wang, H. Wu, J. Zhang, Y. Liu, D. Chen, C. Pandey, J. Yin, D. Wei, N. Lei, S. Shi, H. Lu, P. Li, A. Fert, K. L. Wang, T. Nie, and W. Zhao, Room temperature energy-efficient spin-orbit torque switching in two-dimensional van der Waals $Fe_3GeTe_2$ induced by topological insulators, Nature Communications **14**, 5173 (2023).
[90] Z. Fei, B. Huang, P. Malinowski, W. Wang, T. Song, J. Sanchez, W. Yao, D. Xiao, X. Zhu, A. F. May, W. Wu, D. H. Cobden, J.-H. Chu, and X. Xu, Two-dimensional itinerant ferromagnetism in atomically thin $Fe_3GeTe_2$, Nature Materials **17**, 778 (2018).
[91] S. T. Chyczewski, J. Shi, H. Lee, P. F. Furlanetto, K. Xu, A. M. van der Zande, and W. Zhu, Probing antiferromagnetism in exfoliated $Fe_3GeTe_2$ using magneto-transport measurements, Nanoscale **15**, 14061 (2023).
[92] M. Ribeiro, G. Gentile, A. Marty, D. Dosenovic, H. Okuno, C. Vergnaud, J.-F. Jacquot, D. Jalabert, D. Longo, P. Ohresser, A. Hallal, M. Chshiev, O. Boulle, F. Bonell, and M. Jamet, Large-scale epitaxy of two-dimensional van der Waals room-temperature ferromagnet $Fe_5GeTe_2$, npj 2D Materials and Applications **6**, 10 (2022).
[93] Y. Zhang, S. Wang, Y. Feng, P. Liu, Y. Lu, and B. Xiang, Antisymmetric Peaks Observed in the Hall Resistance of $Fe_5GeTe_2$ Ferromagnets: Implications for Spintronic Devices, ACS Applied Nano Materials **6**, 15734 (2023).
[94] A. F. May, D. Ovchinnikov, Q. Zheng, R. Hermann, S. Calder, B. Huang, Z. Fei, Y. Liu, X. Xu, and M. A. McGuire, Ferromagnetism Near Room Temperature in the Cleavable van der Waals Crystal $Fe_5GeTe_2$, ACS Nano **13**, 4436 (2019).
[95] Y. Deng, Z. Xiang, B. Lei, K. Zhu, H. Mu, W. Zhuo, X. Hua, M. Wang, Z. Wang, G. Wang, M. Tian, and X. Chen, Layer-Number-Dependent Magnetism and Anomalous Hall Effect in van der Waals Ferromagnet $Fe_5GeTe_2$, Nano Letters **22**, 9839 (2022).
[96] G. Zhang, F. Guo, H. Wu, X. Wen, L. Yang, W. Jin, W. Zhang, and H. Chang, Above-room-temperature strong intrinsic ferromagnetism in 2D van der Waals $Fe_3GaTe_2$ with large perpendicular magnetic anisotropy, Nature Communications **13**, 5067 (2022).
[97] J.-E. Lee, S. Yan, S. Oh, J. Hwang, J. D. Denlinger, C. Hwang, H. Lei, S.-K. Mo, S. Y. Park, and H. Ryu, Electronic Structure of Above-Room-Temperature van der Waals Ferromagnet $Fe_3GaTe_2$, Nano Letters **23**, 11526 (2023).
[98] Y.-F. Zhao, L.-J. Zhou, F. Wang, G. Wang, T. Song, D. Ovchinnikov, H. Yi, R. Mei, K. Wang, M. H. W. Chan, C.-X. Liu, X. Xu, and C.-Z. Chang, Even–Odd Layer-Dependent Anomalous Hall Effect in Topological Magnet $MnBi_2Te_4$ Thin Films, Nano Letters **21**, 7691 (2021).
[99] P. Chen, Q. Yao, J. Xu, Q. Sun, A. J. Grutter, P. Quarterman, P. P. Balakrishnan, C. J. Kinane, A. J. Caruana, S. Langridge, A. Li, B. Achinuq, E. Heppell, Y. Ji, S. Liu, B. Cui, J. Liu, P. Huang, Z. Liu, G. Yu, F. Xiu, T. Hesjedal, J. Zou, X. Han, H. Zhang, Y. Yang, and X. Kou, Tailoring the magnetic exchange interaction in $MnBi_2Te_4$ superlattices via the intercalation of ferromagnetic layers, Nature Electronics **6**, 18 (2023).
[100] M. M. Otrokov, I. P. Rusinov, M. Blanco-Rey, M. Hoffmann, A. Y. Vyazovskaya, S. V. Eremeev, A. Ernst, P. M. Echenique, A. Arnau, and E. V. Chulkov, Unique Thickness-Dependent Properties of the van der Waals Interlayer Antiferromagnet $MnBi_2Te_4$ Films, Physical Review Letters **122**, 107202 (2019).

[101] F. Xue, X. He, J. R. D. Retamal, A. Han, J. Zhang, Z. Liu, J.-K. Huang, W. Hu, V. Tung, J.-H. He, L.-J. Li, and X. Zhang, Gate-Tunable and Multidirection-Switchable Memristive Phenomena in a Van Der Waals Ferroelectric, Advanced Materials **31**, 1901300 (2019).
[102] J. A. Brehm, S. M. Neumayer, L. Tao, A. O'Hara, M. Chyasnavichus, M. A. Susner, M. A. McGuire, S. V. Kalinin, S. Jesse, P. Ganesh, S. T. Pantelides, P. Maksymovych, and N. Balke, Tunable quadruple-well ferroelectric van der Waals crystals, Nature Materials **19**, 43 (2020).
[103] L. You, Y. Zhang, S. Zhou, A. Chaturvedi, S. A. Morris, F. Liu, L. Chang, D. Ichinose, H. Funakubo, W. Hu, T. Wu, Z. Liu, S. Dong, and J. Wang, Origin of giant negative piezoelectricity in a layered van der Waals ferroelectric, Science Advances **5**, eaav3780 (2019).
[104] Y. Qi, and A. M. Rappe, Widespread Negative Longitudinal Piezoelectric Responses in Ferroelectric Crystals with Layered Structures, Physical Review Letters **126**, 217601 (2021).
[105] K. Wang, D. Li, J. Wang, Y. Hao, H. Anderson, L. Yang, and X. Hong, Interface-Tuning of Ferroelectricity and Quadruple-Well State in $CuInP_2S_6$ via Ferroelectric Oxide, ACS Nano **17**, 15787 (2023).
[106] Y. Wang, J. Xiao, H. Zhu, Y. Li, Y. Alsaid, K. Y. Fong, Y. Zhou, S. Wang, W. Shi, Y. Wang, A. Zettl, E. J. Reed, and X. Zhang, Structural phase transition in monolayer $MoTe_2$ driven by electrostatic doping, Nature **550**, 487 (2017).
[107] W. Hou, A. Azizimanesh, A. Sewaket, T. Peña, C. Watson, M. Liu, H. Askari, and S. M. Wu, Strain-based room-temperature non-volatile $MoTe_2$ ferroelectric phase change transistor, Nature Nanotechnology **14**, 668 (2019).
[108] T. Song, Z. Fei, M. Yankowitz, Z. Lin, Q. Jiang, K. Hwangbo, Q. Zhang, B. Sun, T. Taniguchi, K. Watanabe, M. A. McGuire, D. Graf, T. Cao, J.-H. Chu, D. H. Cobden, C. R. Dean, D. Xiao, and X. Xu, Switching 2D magnetic states via pressure tuning of layer stacking, Nature Materials **18**, 1298 (2019).
[109] J. Liu, Y. Zhou, Y. Lin, M. Li, H. Cai, Y. Liang, M. Liu, Z. Huang, F. Lai, F. Huang, and W. Zheng, Anisotropic Photoresponse of the Ultrathin GeSe Nanoplates Grown by Rapid Physical Vapor Deposition, ACS Applied Materials & Interfaces **11**, 4123 (2019).
[110] P. Sharma, T. S. Moise, L. Colombo, and J. Seidel, Roadmap for Ferroelectric Domain Wall Nanoelectronics, Advanced Functional Materials **32**, 2110263 (2022).
[111] W.-Y. Tong, S.-J. Gong, X. Wan, and C.-G. Duan, Concepts of ferrovalley material and anomalous valley Hall effect, Nature Communications **7**, 13612 (2016).
[112] S. Dong, Review on Piezoelectric, Ultrasonic, and Magnetoelectric Actuators, Journal of Advanced Dielectrics **02**, 1230001 (2012).
[113] W. Zhu, X. Hong, P. D. Ye, and Y. Gu, 2D Piezoelectrics, pyroelectrics, and ferroelectrics, Journal of Applied Physics **133**, 120402 (2023).
[114] X. Wang, P. Yu, Z. Lei, C. Zhu, X. Cao, F. Liu, L. You, Q. Zeng, Y. Deng, C. Zhu, J. Zhou, Q. Fu, J. Wang, Y. Huang, and Z. Liu, Van der Waals negative capacitance transistors, Nature Communications **10**, 3037 (2019).
[115] L. Zhao, Y. Liang, J. Ma, Z. Pan, X. Liu, M. Yang, Y. Sun, W. Gao, B. Li, J. Li, and N. Huo, Ultra-Steep-Slope and High-Stability of $CuInP_2S_6/WS_2$ Ferroelectric Negative Capacitor Transistors by Passivation Effect and Dual-Gate Modulation, Advanced Functional Materials **33**, 2306708 (2023).
[116] S. M. Neumayer, L. Tao, A. O'Hara, M. A. Susner, M. A. McGuire, P. Maksymovych, S. T. Pantelides, and N. Balke, The Concept of Negative Capacitance in Ionically Conductive Van der Waals Ferroelectrics, Advanced Energy Materials **10**, 2001726 (2020).

[117] K. Kim, S. Y. Lim, J. Kim, J.-U. Lee, S. Lee, P. Kim, K. Park, S. Son, C.-H. Park, J.-G. Park, and H. Cheong, Antiferromagnetic ordering in van der Waals 2D magnetic material $MnPS_3$ probed by Raman spectroscopy, 2D Materials **6**, 041001 (2019).
[118] S. Baek, H. H. Yoo, J. H. Ju, P. Sriboriboon, P. Singh, J. Niu, J.-H. Park, C. Shin, Y. Kim, and S. Lee, Ferroelectric Field-Effect-Transistor Integrated with Ferroelectrics Heterostructure, Advanced Science **9**, 2200566 (2022).
[119] S. Zhou, L. You, A. Chaturvedi, S. A. Morris, J. S. Herrin, N. Zhang, A. Abdelsamie, Y. Hu, J. Chen, Y. Zhou, S. Dong, and J. Wang, Anomalous polarization switching and permanent retention in a ferroelectric ionic conductor, Materials Horizons **7**, 263 (2020).
[120] W. Huang, F. Wang, L. Yin, R. Cheng, Z. Wang, M. G. Sendeku, J. Wang, N. Li, Y. Yao, and J. He, Gate-Coupling-Enabled Robust Hysteresis for Nonvolatile Memory and Programmable Rectifier in Van der Waals Ferroelectric Heterojunctions, Advanced Materials **32**, 1908040 (2020).
[121] M. Y. Zhuravlev, R. F. Sabirianov, S. S. Jaswal, and E. Y. Tsymbal, Giant electroresistance in ferroelectric tunnel junctions, Physical Review Letters **94**, 246802 (2005).
[122] J. Wu, H.-Y. Chen, N. Yang, J. Cao, X. Yan, F. Liu, Q. Sun, X. Ling, J. Guo, and H. Wang, High tunnelling electroresistance in a ferroelectric van der Waals heterojunction via giant barrier height modulation, Nature Electronics **3**, 466 (2020).
[123] M. Zhao, G. Gou, X. Ding, and J. Sun, An ultrathin two-dimensional vertical ferroelectric tunneling junction based on $CuInP_2S_6$ monolayer, Nanoscale **12**, 12522 (2020).
[124] M. Si, Z. Zhang, S.-C. Chang, N. Haratipour, D. Zheng, J. Li, U. E. Avci, and P. D. Ye, Asymmetric Metal/α-$In_2Se_3$/Si Crossbar Ferroelectric Semiconductor Junction, ACS Nano **15**, 5689 (2021).
[125] L. Wang, G. Sun, and S. Yuan, Chemical Vapor Deposition Growth of 2D Ferroelectric Materials for Device Applications, Advanced Materials Technologies **9**, 2301973 (2024).
[126] M. Gibertini, M. Koperski, A. F. Morpurgo, and K. S. Novoselov, Magnetic 2D materials and heterostructures, Nature Nanotechnology **14**, 408 (2019).
[127] C. Wang, L. You, D. Cobden, and J. Wang, Towards two-dimensional van der Waals ferroelectrics, Nature Materials **22**, 542 (2023).
[128] M. Hossain, B. Qin, B. Li, and X. Duan, Synthesis, characterization, properties and applications of two-dimensional magnetic materials, Nano Today **42**, 101338 (2022).
[129] A. Dimoulas, Perspectives for the Growth of Epitaxial 2D van der Waals Layers with an Emphasis on Ferromagnetic Metals for Spintronics, Advanced Materials Interfaces **9**, 2201469 (2022).
[130] C. Hu, T. Qian, and N. Ni, Recent progress in $MnBi_{2n}Te_{3n+1}$ intrinsic magnetic topological insulators: crystal growth, magnetism and chemical disorder, National Science Review **11**, nwad282 (2023).
[131] D. Wang, F. Luo, M. Lu, X. Xie, L. Huang, and W. Huang, Chemical Vapor Transport Reactions for Synthesizing Layered Materials and Their 2D Counterparts, Small **15**, 1804404 (2019).
[132] C. Tan, J. Lee, S.-G. Jung, T. Park, S. Albarakati, J. Partridge, M. R. Field, D. G. McCulloch, L. Wang, and C. Lee, Hard magnetic properties in nanoflake van der Waals $Fe_3GeTe_2$, Nature Communications **9**, 1554 (2018).
[133] M. Grönke, B. Buschbeck, P. Schmidt, M. Valldor, S. Oswald, Q. Hao, A. Lubk, D. Wolf, U. Steiner, B. Büchner, and S. Hampel, Chromium Trihalides $CrX_3$ (X = Cl, Br, I): Direct

Deposition of Micro- and Nanosheets on Substrates by Chemical Vapor Transport, Advanced Materials Interfaces **6**, 1901410 (2019).
[134] Y. T. Liu, A. N. Morozovska, A. Ghosh, K. P. Kelley, E. A. Eliseev, J. Y. Yao, Y. Liu, and S. Kalinin, Stress and Curvature Effects in Layered 2D Ferroelectric $CuInP_2S_6$, Acs Nano **17**, 22004 (2023).
[135] L. Niu, F. Liu, Q. Zeng, X. Zhu, Y. Wang, P. Yu, J. Shi, J. Lin, J. Zhou, Q. Fu, W. Zhou, T. Yu, X. Liu, and Z. Liu, Controlled synthesis and room-temperature pyroelectricity of $CuInP_2S_6$ ultrathin flakes, Nano Energy **58**, 596 (2019).
[136] S. Wang, L. Liu, L. Gan, H. Chen, X. Hou, Y. Ding, S. Ma, D. W. Zhang, and P. Zhou, Two-dimensional ferroelectric channel transistors integrating ultra-fast memory and neural computing, Nature Communications **12**, 53 (2021).
[137] M. G. Kanatzidis, R. Pöttgen, and W. Jeitschko, The Metal Flux: A Preparative Tool for the Exploration of Intermetallic Compounds, Angewandte Chemie International Edition **44**, 6996 (2005).
[138] A. F. May, J. Yan, and M. A. McGuire, A practical guide for crystal growth of van der Waals layered materials, Journal of Applied Physics **128**, 051101 (2020).
[139] J. Q. Yan, B. C. Sales, M. A. Susner, and M. A. McGuire, Flux growth in a horizontal configuration: An analog to vapor transport growth, Physical Review Materials **1**, 023402 (2017).
[140] K. S. Novoselov, A. K. Geim, S. V. Morozov, D. Jiang, Y. Zhang, S. V. Dubonos, I. V. Grigorieva, and A. A. Firsov, Electric Field Effect in Atomically Thin Carbon Films, Science **306**, 666 (2004).
[141] A. K. Geim, and K. S. Novoselov, The rise of graphene, Nature Materials **6**, 183 (2007).
[142] A. Castellanos-Gomez, M. Buscema, R. Molenaar, V. Singh, L. Janssen, H. S. J. van der Zant, and G. A. Steele, Deterministic transfer of two-dimensional materials by all-dry viscoelastic stamping, 2D Materials **1**, 011002 (2014).
[143] S. Kazim, M. Alì, S. Palleschi, G. D'Olimpio, D. Mastrippolito, A. Politano, R. Gunnella, A. Di Cicco, M. Renzelli, G. Moccia, O. A. Cacioppo, R. Alfonsetti, J. Strychalska-Nowak, T. Klimczuk, R. J Cava, and L. Ottaviano, Mechanical exfoliation and layer number identification of single crystal monoclinic $CrCl_3$, Nanotechnology **31**, 395706 (2020).
[144] K. Hwangbo, Q. Zhang, Q. Jiang, Y. Wang, J. Fonseca, C. Wang, G. M. Diederich, D. R. Gamelin, D. Xiao, J.-H. Chu, W. Yao, and X. Xu, Highly anisotropic excitons and multiple phonon bound states in a van der Waals antiferromagnetic insulator, Nature Nanotechnology **16**, 655 (2021).
[145] C.-T. Kuo, M. Neumann, K. Balamurugan, H. J. Park, S. Kang, H. W. Shiu, J. H. Kang, B. H. Hong, M. Han, T. W. Noh, and J.-G. Park, Exfoliation and Raman Spectroscopic Fingerprint of Few-Layer $NiPS_3$ Van der Waals Crystals, Scientific Reports **6**, 20904 (2016).
[146] F. M. Bartram, Y.-C. Leng, Y. Wang, L. Liu, X. Chen, H. Peng, H. Li, P. Yu, Y. Wu, M.-L. Lin, J. Zhang, P.-H. Tan, and L. Yang, Ultrafast coherent interlayer phonon dynamics in atomically thin layers of $MnBi_2Te_4$, npj Quantum Materials **7**, 84 (2022).
[147] S. Yang, X. Xu, Y. Zhu, R. Niu, C. Xu, Y. Peng, X. Cheng, X. Jia, Y. Huang, X. Xu, J. Lu, and Y. Ye, Odd-Even Layer-Number Effect and Layer-Dependent Magnetic Phase Diagrams in $MnBi_2Te_4$, Physical Review X **11**, 011003 (2021).
[148] A. Gao, Y.-F. Liu, C. Hu, J.-X. Qiu, C. Tzschaschel, B. Ghosh, S.-C. Ho, D. Bérubé, R. Chen, H. Sun, Z. Zhang, X.-Y. Zhang, Y.-X. Wang, N. Wang, Z. Huang, C. Felser, A. Agarwal, T. Ding, H.-J. Tien, A. Akey, J. Gardener, B. Singh, K. Watanabe, T. Taniguchi, K.

S. Burch, D. C. Bell, B. B. Zhou, W. Gao, H.-Z. Lu, A. Bansil, H. Lin, T.-R. Chang, L. Fu, Q. Ma, N. Ni, and S.-Y. Xu, Layer Hall effect in a 2D topological axion antiferromagnet, Nature **595**, 521 (2021).

[149] F. Liu, W. Wu, Y. Bai, S. H. Chae, Q. Li, J. Wang, J. Hone, and X. Y. Zhu, Disassembling 2D van der Waals crystals into macroscopic monolayers and reassembling into artificial lattices, Science **367**, 903 (2020).

[150] Y. Huang, Y.-H. Pan, R. Yang, L.-H. Bao, L. Meng, H.-L. Luo, Y.-Q. Cai, G.-D. Liu, W.-J. Zhao, Z. Zhou, L.-M. Wu, Z.-L. Zhu, M. Huang, L.-W. Liu, L. Liu, P. Cheng, K.-H. Wu, S.-B. Tian, C.-Z. Gu, Y.-G. Shi, Y.-F. Guo, Z. G. Cheng, J.-P. Hu, L. Zhao, G.-H. Yang, E. Sutter, P. Sutter, Y.-L. Wang, W. Ji, X.-J. Zhou, and H.-J. Gao, Universal mechanical exfoliation of large-area 2D crystals, Nature Communications **11**, 2453 (2020).

[151] J.-Y. Moon, M. Kim, S.-I. Kim, S. Xu, J.-H. Choi, D. Whang, K. Watanabe, T. Taniguchi, D. S. Park, J. Seo, S. H. Cho, S.-K. Son, and J.-H. Lee, Layer-engineered large-area exfoliation of graphene, Science Advances **6**, eabc6601 (2020).

[152] J. Shim, S.-H. Bae, W. Kong, D. Lee, K. Qiao, D. Nezich, Y. J. Park, R. Zhao, S. Sundaram, X. Li, H. Yeon, C. Choi, H. Kum, R. Yue, G. Zhou, Y. Ou, K. Lee, J. Moodera, X. Zhao, J.-H. Ahn, C. Hinkle, A. Ougazzaden, and J. Kim, Controlled crack propagation for atomic precision handling of wafer-scale two-dimensional materials, Science **362**, 665 (2018).

[153] Z. Li, L. Ren, S. Wang, X. Huang, Q. Li, Z. Lu, S. Ding, H. Deng, P. Chen, J. Lin, Y. Hu, L. Liao, and Y. Liu, Dry Exfoliation of Large-Area 2D Monolayer and Heterostructure Arrays, ACS Nano **15**, 13839 (2021).

[154] S. B. Desai, S. R. Madhvapathy, M. Amani, D. Kiriya, M. Hettick, M. Tosun, Y. Zhou, M. Dubey, J. W. Ager Iii, D. Chrzan, and A. Javey, Gold-Mediated Exfoliation of Ultralarge Optoelectronically-Perfect Monolayers, Advanced Materials **28**, 4053 (2016).

[155] X. Fan, P. Xu, D. Zhou, Y. Sun, Y. C. Li, M. A. T. Nguyen, M. Terrones, and T. E. Mallouk, Fast and Efficient Preparation of Exfoliated 2H $MoS_2$ Nanosheets by Sonication-Assisted Lithium Intercalation and Infrared Laser-Induced 1T to 2H Phase Reversion, Nano Letters **15**, 5956 (2015).

[156] V. Nicolosi, M. Chhowalla, M. G. Kanatzidis, M. S. Strano, and J. N. Coleman, Liquid Exfoliation of Layered Materials, Science **340**, 1226419 (2013).

[157] J. N. Coleman, M. Lotya, A. O'Neill, S. D. Bergin, P. J. King, U. Khan, K. Young, A. Gaucher, S. De, R. J. Smith, I. V. Shvets, S. K. Arora, G. Stanton, H.-Y. Kim, K. Lee, G. T. Kim, G. S. Duesberg, T. Hallam, J. J. Boland, J. J. Wang, J. F. Donegan, J. C. Grunlan, G. Moriarty, A. Shmeliov, R. J. Nicholls, J. M. Perkins, E. M. Grieveson, K. Theuwissen, D. W. McComb, P. D. Nellist, and V. Nicolosi, Two-Dimensional Nanosheets Produced by Liquid Exfoliation of Layered Materials, Science **331**, 568 (2011).

[158] J. Shen, Y. He, J. Wu, C. Gao, K. Keyshar, X. Zhang, Y. Yang, M. Ye, R. Vajtai, J. Lou, and P. M. Ajayan, Liquid Phase Exfoliation of Two-Dimensional Materials by Directly Probing and Matching Surface Tension Components, Nano Letters **15**, 5449 (2015).

[159] R. Xue, Z. Shao, X. Yang, Y. Zhang, Z. Fu, Y. Huang, and W. Feng, Self-Powered Photoelectrochemical Photodetectors Based on Electrochemically Exfoliated $In_2Se_3$ Nanosheets, ACS Applied Nano Materials **5**, 7036 (2022).

[160] B. Lin, A. Chaturvedi, J. Di, L. You, C. Lai, R. Duan, J. Zhou, B. Xu, Z. Chen, P. Song, J. Peng, B. Ma, H. Liu, P. Meng, G. Yang, H. Zhang, Z. Liu, and F. Liu, Ferroelectric-field accelerated charge transfer in 2D $CuInP_2S_6$ heterostructure for enhanced photocatalytic $H_2$ evolution, Nano Energy **76**, 104972 (2020).

[161] A. Ambrosi, and M. Pumera, Exfoliation of layered materials using electrochemistry, Chemical Society Reviews **47**, 7213 (2018).
[162] S. Yang, P. Zhang, A. S. Nia, and X. Feng, Emerging 2D Materials Produced via Electrochemistry, Advanced Materials **32**, 1907857 (2020).
[163] M. Hofmann, W.-Y. Chiang, T. D Nguyễn, and Y.-P. Hsieh, Controlling the properties of graphene produced by electrochemical exfoliation, Nanotechnology **26**, 335607 (2015).
[164] W.-W. Liu, and A. Aziz, Review on the Effects of Electrochemical Exfoliation Parameters on the Yield of Graphene Oxide, ACS Omega **7**, 33719 (2022).
[165] Q. Zhang, L. Mei, X. Cao, Y. Tang, and Z. Zeng, Intercalation and exfoliation chemistries of transition metal dichalcogenides, Journal of Materials Chemistry A **8**, 15417 (2020).
[166] N. Liu, P. Kim, J. H. Kim, J. H. Ye, S. Kim, and C. J. Lee, Large-Area Atomically Thin $MoS_2$ Nanosheets Prepared Using Electrochemical Exfoliation, ACS Nano **8**, 6902 (2014).
[167] A. Ambrosi, Z. Sofer, and M. Pumera, Electrochemical Exfoliation of Layered Black Phosphorus into Phosphorene, Angewandte Chemie International Edition **56**, 10443 (2017).
[168] P. Yu, S. E. Lowe, G. P. Simon, and Y. L. Zhong, Electrochemical exfoliation of graphite and production of functional graphene, Current Opinion in Colloid & Interface Science **20**, 329 (2015).
[169] H. Shi, M. Li, A. Shaygan Nia, M. Wang, S. Park, Z. Zhang, M. R. Lohe, S. Yang, and X. Feng, Ultrafast Electrochemical Synthesis of Defect-Free $In_2Se_3$ Flakes for Large-Area Optoelectronics, Advanced Materials **32**, 1907244 (2020).
[170] X. Gao, H.-Y. Liu, J. Zhang, J. Zhu, J. Chang, and Y. Hao, Thin-Film Transistors from Electrochemically Exfoliated $In_2Se_3$ Nanosheets, Micromachines **13**, 956 (2022).
[171] M. Wu, and J. Li, Sliding ferroelectricity in 2D van der Waals materials: Related physics and future opportunities, Proceedings of the National Academy of Sciences **118**, e2115703118 (2021).
[172] X. Zhang, and B. Peng, The twisted two-dimensional ferroelectrics, Journal of Semiconductors **44**, 011002 (2023).
[173] M. Vizner Stern, Y. Waschitz, W. Cao, I. Nevo, K. Watanabe, T. Taniguchi, E. Sela, M. Urbakh, O. Hod, and M. Ben Shalom, Interfacial ferroelectricity by van der Waals sliding, Science **372**, 1462 (2021).
[174] S. L. Moore, C. J. Ciccarino, D. Halbertal, L. J. McGilly, N. R. Finney, K. Yao, Y. Shao, G. Ni, A. Sternbach, E. J. Telford, B. S. Kim, S. E. Rossi, K. Watanabe, T. Taniguchi, A. N. Pasupathy, C. R. Dean, J. Hone, P. J. Schuck, P. Narang, and D. N. Basov, Nanoscale lattice dynamics in hexagonal boron nitride moiré superlattices, Nature Communications **12**, 5741 (2021).
[175] L. J. McGilly, A. Kerelsky, N. R. Finney, K. Shapovalov, E.-M. Shih, A. Ghiotto, Y. Zeng, S. L. Moore, W. Wu, Y. Bai, K. Watanabe, T. Taniguchi, M. Stengel, L. Zhou, J. Hone, X. Zhu, D. N. Basov, C. Dean, C. E. Dreyer, and A. N. Pasupathy, Visualization of moiré superlattices, Nature Nanotechnology **15**, 580 (2020).
[176] N. C. H. Hesp, I. Torre, D. Barcons-Ruiz, H. Herzig Sheinfux, K. Watanabe, T. Taniguchi, R. Krishna Kumar, and F. H. L. Koppens, Nano-imaging photoresponse in a moiré unit cell of minimally twisted bilayer graphene, Nature Communications **12**, 1640 (2021).
[177] S. Zhang, Y. Liu, Z. Sun, X. Chen, B. Li, S. L. Moore, S. Liu, Z. Wang, S. E. Rossi, R. Jing, J. Fonseca, B. Yang, Y. Shao, C.-Y. Huang, T. Handa, L. Xiong, M. Fu, T.-C. Pan, D. Halbertal, X. Xu, W. Zheng, P. J. Schuck, A. N. Pasupathy, C. R. Dean, X. Zhu, D. H. Cobden, X. Xu, M. Liu, M. M. Fogler, J. C. Hone, and D. N. Basov, Visualizing moiré

ferroelectricity via plasmons and nano-photocurrent in graphene/twisted-$WSe_2$ structures, Nature Communications **14**, 6200 (2023).
[178] F. Cui, X. Zhao, J. Xu, B. Tang, Q. Shang, J. Shi, Y. Huan, J. Liao, Q. Chen, Y. Hou, Q. Zhang, S. J. Pennycook, and Y. Zhang, Controlled Growth and Thickness-Dependent Conduction-Type Transition of 2D Ferrimagnetic $Cr_2S_3$ Semiconductors, Advanced Materials **32**, 1905896 (2020).
[179] S. Zhou, R. Wang, J. Han, D. Wang, H. Li, L. Gan, and T. Zhai, Ultrathin Non-van der Waals Magnetic Rhombohedral $Cr_2S_3$: Space-Confined Chemical Vapor Deposition Synthesis and Raman Scattering Investigation, Advanced Functional Materials **29**, 1805880 (2019).
[180] J. You, J. Pan, S.-L. Shang, X. Xu, Z. Liu, J. Li, H. Liu, T. Kang, M. Xu, S. Li, D. Kong, W. Wang, Z. Gao, X. Zhou, T. Zhai, Z.-K. Liu, J.-K. Kim, and Z. Luo, Salt-Assisted Selective Growth of H-phase Monolayer $VSe_2$ with Apparent Hole Transport Behavior, Nano Letters **22**, 10167 (2022).
[181] C. Chen, X. Chen, C. Wu, X. Wang, Y. Ping, X. Wei, X. Zhou, J. Lu, L. Zhu, J. Zhou, T. Zhai, J. Han, and H. Xu, Air-Stable 2D $Cr_5Te_8$ Nanosheets with Thickness-Tunable Ferromagnetism, Advanced Materials **34**, 2107512 (2022).
[182] H. Wu, J. Guo, S. Zhaxi, H. Xu, S. Mi, L. Wang, S. Chen, R. Xu, W. Ji, F. Pang, and Z. Cheng, Controllable CVD Growth of 2D $Cr_5Te_8$ Nanosheets with Thickness-Dependent Magnetic Domains, ACS Applied Materials & Interfaces **15**, 26148 (2023).
[183] J. Zhou, Q. Zeng, D. Lv, L. Sun, L. Niu, W. Fu, F. Liu, Z. Shen, C. Jin, and Z. Liu, Controlled Synthesis of High-Quality Monolayered α-$In_2Se_3$ via Physical Vapor Deposition, Nano Letters **15**, 6400 (2015).
[184] L. Tang, C. Teng, Y. Luo, U. Khan, H. Pan, Z. Cai, Y. Zhao, B. Liu, and H.-M. Cheng, Confined van der Waals Epitaxial Growth of Two-Dimensional Large Single-Crystal $In_2Se_3$ for Flexible Broadband Photodetectors, Research **2019**, 2763704 (2019).
[185] E. Sutter, J. Wang, and P. Sutter, Surface Passivation by Excess Sulfur for Controlled Synthesis of Large, Thin SnS Flakes, Chemistry of Materials **32**, 8034 (2020).
[186] Z. Cai, B. Liu, X. Zou, and H.-M. Cheng, Chemical Vapor Deposition Growth and Applications of Two-Dimensional Materials and Their Heterostructures, Chemical Reviews **118**, 6091 (2018).
[187] S. K. Chakraborty, B. Kundu, B. Nayak, S. P. Dash, and P. K. Sahoo, Challenges and opportunities in 2D heterostructures for electronic and optoelectronic devices, iScience **25**, 103942 (2022).
[188] P. Sutter, J. Wang, and E. Sutter, Wrap-Around Core-Shell Heterostructures of Layered Crystals, Advanced Materials **31**, 1902166 (2019).
[189] P. Sutter, and E. Sutter, Growth Mechanisms of Anisotropic Layered Group IV Chalcogenides on van der Waals Substrates for Energy Conversion Applications, ACS Applied Nano Materials **1**, 3026 (2018).
[190] S. M. Poh, S. J. R. Tan, H. Wang, P. Song, I. H. Abidi, X. Zhao, J. Dan, J. Chen, Z. Luo, S. J. Pennycook, A. H. Castro Neto, and K. P. Loh, Molecular-Beam Epitaxy of Two-Dimensional $In_2Se_3$ and Its Giant Electroresistance Switching in Ferroresistive Memory Junction, Nano Letters **18**, 6340 (2018).
[191] Z. Chen, W. Fu, L. Wang, W. Yu, H. Li, C. K. Y. Tan, I. Abdelwahab, Y. Shao, C. Su, M. Sun, B. Huang, and K. P. Loh, Atomic Imaging of Electrically Switchable Striped Domains in β′-$In_2Se_3$, Advanced Science **8**, 2100713 (2021).

[192] Q. Chen, K. Yang, M. Liang, J. Kang, X. Yi, J. Wang, J. Li, and Z. Liu, Lattice modulation strategies for 2D material assisted epitaxial growth, Nano Convergence **10**, 39 (2023).
[193] A. Bedoya-Pinto, J.-R. Ji, A. K. Pandeya, P. Gargiani, M. Valvidares, P. Sessi, J. M. Taylor, F. Radu, K. Chang, and S. S. P. Parkin, Intrinsic 2D-XY ferromagnetism in a van der Waals monolayer, Science **374**, 616 (2021).
[194] Y. Zou, Z. Zhang, J. Yan, L. Lin, G. Huang, Y. Tan, Z. You, and P. Li, High-temperature flexible $WSe_2$ photodetectors with ultrahigh photoresponsivity, Nature Communications **13**, 4372 (2022).
[195] H. Zheng, C. Huang, F. Lin, J. Fan, H. Liu, L. Zhang, C. Ma, C. Wang, Y. Zhu, and H. Yang, Two-dimensional van der Waals ferromagnetic thin film $CrTe_2$ with high Curie temperature and metallic conductivity, Applied Physics Letters **122**, 023103 (2023).
[196] T. Kim, H. Park, D. Joung, D. Kim, R. Lee, C. H. Shin, M. Diware, W. Chegal, S. H. Jeong, J. C. Shin, J. Park, and S.-W. Kang, Wafer-Scale Epitaxial 1T′, 1T′–2H Mixed, and 2H Phases $MoTe_2$ Thin Films Grown by Metal–Organic Chemical Vapor Deposition, Advanced Materials Interfaces **5**, 1800439 (2018).
[197] Z. Guo, R. Zhao, S. Yan, W. Xiong, J. Zhu, K. Lu, and X. Wang, Atomic Layer Deposition of $FeSe_2$, $CoSe_2$, and $NiSe_2$, Chemistry of Materials **33**, 2478 (2021).
[198] K. Kang, S. Xie, L. Huang, Y. Han, P. Y. Huang, K. F. Mak, C.-J. Kim, D. Muller, and J. Park, High-mobility three-atom-thick semiconducting films with wafer-scale homogeneity, Nature **520**, 656 (2015).
[199] Y. Gong, J. Lin, X. Wang, G. Shi, S. Lei, Z. Lin, X. Zou, G. Ye, R. Vajtai, B. I. Yakobson, H. Terrones, M. Terrones, Beng K. Tay, J. Lou, S. T. Pantelides, Z. Liu, W. Zhou, and P. M. Ajayan, Vertical and in-plane heterostructures from $WS_2$/$MoS_2$ monolayers, Nature Materials **13**, 1135 (2014).
[200] J. Zhu, W. Li, R. Huang, L. Ma, H. Sun, J.-H. Choi, L. Zhang, Y. Cui, and G. Zou, One-Pot Selective Epitaxial Growth of Large $WS_2$/$MoS_2$ Lateral and Vertical Heterostructures, Journal of the American Chemical Society **142**, 16276 (2020).
[201] D. Wang, Z. Zhang, B. Huang, H. Zhang, Z. Huang, M. Liu, and X. Duan, Few-Layer $WS_2$–$WSe_2$ Lateral Heterostructures: Influence of the Gas Precursor Selenium/Tungsten Ratio on the Number of Layers, ACS Nano **16**, 1198 (2022).
[202] M.-Y. Li, Y. Shi, C.-C. Cheng, L.-S. Lu, Y.-C. Lin, H.-L. Tang, M.-L. Tsai, C.-W. Chu, K.-H. Wei, J.-H. He, W.-H. Chang, K. Suenaga, and L.-J. Li, Epitaxial growth of a monolayer $WSe_2$-$MoS_2$ lateral p-n junction with an atomically sharp interface, Science **349**, 524 (2015).
[203] M. Li, Y. Zhu, T. Li, Y. Lin, H. Cai, S. Li, H. Ding, N. Pan, and X. Wang, One-step CVD fabrication and optoelectronic properties of $SnS_2$/SnS vertical heterostructures, Inorganic Chemistry Frontiers **5**, 1828 (2018).
[204] M. Diao, H. Li, R. Hou, Y. Liang, J. Wang, Z. Luo, Z. Huang, and C. Zhang, Vertical Heterostructure of SnS–$MoS_2$ Synthesized by Sulfur-Preloaded Chemical Vapor Deposition, ACS Applied Materials & Interfaces **12**, 7423 (2020).
[205] Z. Zou, D. Li, J. Liang, X. Zhang, H. Liu, C. Zhu, X. Yang, L. Li, B. Zheng, X. Sun, Z. Zeng, J. Yi, X. Zhuang, X. Wang, and A. Pan, Epitaxial synthesis of ultrathin β-$In_2Se_3$/$MoS_2$ heterostructures with high visible/near-infrared photoresponse, Nanoscale **12**, 6480 (2020).
[206] Y.-l. Chen, M.-l. Li, Y.-m. Wu, S.-j. Li, Y. Lin, D.-x. Du, H.-y. Ding, N. Pan, and X.-p. Wang, Two Step Chemical Vapor Deposition of $In_2Se_3$/$MoSe_2$ van der Waals Heterostructures, Chinese Journal of Chemical Physics **30**, 325 (2017).

[207] E. Sutter, B. Zhang, M. Sun, and P. Sutter, Few-Layer to Multilayer Germanium(II) Sulfide: Synthesis, Structure, Stability, and Optoelectronics, ACS Nano **13**, 9352 (2019).
[208] P. Sutter, H.-P. Komsa, K. Kisslinger, and E. Sutter, Lateral Integration of SnS and GeSe van der Waals Semiconductors: Interface Formation, Electronic Structure, and Nanoscale Optoelectronics, ACS Nano **17**, 9552 (2023).
[209] G.-H. Lee, R. C. Cooper, S. J. An, S. Lee, A. van der Zande, N. Petrone, A. G. Hammerberg, C. Lee, B. Crawford, W. Oliver, J. W. Kysar, and J. Hone, High-Strength Chemical-Vapor–Deposited Graphene and Grain Boundaries, Science **340**, 1073 (2013).
[210] L. Banszerus, M. Schmitz, S. Engels, J. Dauber, M. Oellers, F. Haupt, K. Watanabe, T. Taniguchi, B. Beschoten, and C. Stampfer, Ultrahigh-mobility graphene devices from chemical vapor deposition on reusable copper, Science Advances **1**, e1500222 (2015).
[211] K. Lai, Spontaneous polarization in van der Waals materials: Two-dimensional ferroelectrics and device applications, Journal of Applied Physics **132**, 121102 (2022).
[212] Y. Dong, C. An, Y. Wu, Z. Zhang, T. Li, T. Min, J. Yang, X. Chen, and M. Tian, Comprehensive Study of Electrode Effect in Metal/$CuInP_2S_6$/Metal Heterostructures, Symmetry **15**, 966 (2023).
[213] Y. Hu, L. Rogée, W. Wang, L. Zhuang, F. Shi, H. Dong, S. Cai, B. K. Tay, and S. P. Lau, Extendable piezo/ferroelectricity in nonstoichiometric 2D transition metal dichalcogenides, Nature Communications **14**, 8470 (2023).
[214] L. Rogée, L. Wang, Y. Zhang, S. H. Cai, P. Wang, M. Chhowalla, W. Ji, and S. P. Lau, Ferroelectricity in untwisted heterobilayers of transition metal dichalcogenides, Science **376**, 973 (2022).
[215] H. S. Zheng, Y. Choi, F. Baniasadi, D. K. Hu, L. Y. Jiao, K. Park, and C. G. Tao, Visualization of point defects in ultrathin layered 1T-PtSe, 2D Materials **6**, 041005 (2019).
[216] F. Zhang, Z. Wang, L. Liu, A. Nie, Y. Li, Y. Gong, W. Zhu, and C. Tao, Atomic-scale manipulation of polar domain boundaries in monolayer ferroelectric $In_2Se_3$, Nature Communications **15**, 718 (2024).
[217] C. Zheng, L. Yu, L. Zhu, J. L. Collins, D. Kim, Y. Lou, C. Xu, M. Li, Z. Wei, Y. Zhang, M. T. Edmonds, S. Li, J. Seidel, Y. Zhu, J. Z. Liu, W.-X. Tang, and M. S. Fuhrer, Room temperature in-plane ferroelectricity in van der Waals $In_2Se_3$, Science Advances **4**, eaar7720 (2018).
[218] J. Gou, H. Bai, X. Zhang, Y. L. Huang, S. Duan, A. Ariando, S. A. Yang, L. Chen, Y. Lu, and A. T. S. Wee, Two-dimensional ferroelectricity in a single-element bismuth monolayer, Nature **617**, 67 (2023).
[219] I. Žutić, J. Fabian, and S. Das Sarma, Spintronics: Fundamentals and applications, Reviews of Modern Physics **76**, 323 (2004).
[220] T. Li, L. Zhang, and X. Hong, Anisotropic magnetoresistance and planar Hall effect in correlated and topological materials, Journal of Vacuum Science & Technology A **40**, 010807 (2021).
[221] N. Nagaosa, J. Sinova, S. Onoda, A. H. Macdonald, and N. P. Ong, Anomalous Hall effect, Reviews of Modern Physics **82**, 1539 (2010).
[222] L. Zhang, X. Huang, H. Dai, M. Wang, H. Cheng, L. Tong, Z. Li, X. Han, X. Wang, L. Ye, and J. Han, Proximity-Coupling-Induced Significant Enhancement of Coercive Field and Curie Temperature in 2D van der Waals Heterostructures, Advanced Materials **32**, 2002032 (2020).

[223] M. Serri, G. Cucinotta, L. Poggini, G. Serrano, P. Sainctavit, J. Strychalska-Nowak, A. Politano, F. Bonaccorso, A. Caneschi, R. J. Cava, R. Sessoli, L. Ottaviano, T. Klimczuk, V. Pellegrini, and M. Mannini, Enhancement of the Magnetic Coupling in Exfoliated $CrCl_3$ Crystals Observed by Low-Temperature Magnetic Force Microscopy and X-ray Magnetic Circular Dichroism, Advanced Materials **32**, 2000566 (2020).
[224] D. Lujan, J. Choe, M. Rodriguez-Vega, Z. Ye, A. Leonardo, T. N. Nunley, L.-J. Chang, S.-F. Lee, J. Yan, G. A. Fiete, R. He, and X. Li, Magnons and magnetic fluctuations in atomically thin $MnBi_2Te_4$, Nature Communications **13**, 2527 (2022).
[225] T.-E. Park, L. Peng, J. Liang, A. Hallal, F. S. Yasin, X. Zhang, K. M. Song, S. J. Kim, K. Kim, M. Weigand, G. Schütz, S. Finizio, J. Raabe, K. Garcia, J. Xia, Y. Zhou, M. Ezawa, X. Liu, J. Chang, H. C. Koo, Y. D. Kim, M. Chshiev, A. Fert, H. Yang, X. Yu, and S. Woo, Néel-type skyrmions and their current-induced motion in van der Waals ferromagnet-based heterostructures, Physical Review B **103**, 104410 (2021).
[226] K. F. Mak, J. Shan, and D. C. Ralph, Probing and controlling magnetic states in 2D layered magnetic materials, Nature Reviews Physics **1**, 646 (2019).
[227] Z. Q. Qiu, and S. D. Bader, Surface magneto-optic Kerr effect, Review of Scientific Instruments **71**, 1243 (2000).
[228] J. M. Taylor, P. Cappellaro, L. Childress, L. Jiang, D. Budker, P. R. Hemmer, A. Yacoby, R. Walsworth, and M. D. Lukin, High-sensitivity diamond magnetometer with nanoscale resolution, Nature Physics **4**, 810 (2008).
[229] L. Rondin, J. P. Tetienne, T. Hingant, J. F. Roch, P. Maletinsky, and V. Jacques, Magnetometry with nitrogen-vacancy defects in diamond, Reports on Progress in Physics **77**, 056503 (2014).
[230] P. Maletinsky, S. Hong, M. S. Grinolds, B. Hausmann, M. D. Lukin, R. L. Walsworth, M. Loncar, and A. Yacoby, A robust scanning diamond sensor for nanoscale imaging with single nitrogen-vacancy centres, Nature Nanotechnology **7**, 320 (2012).
[231] L. Thiel, Z. Wang, M. A. Tschudin, D. Rohner, I. Gutiérrez-Lezama, N. Ubrig, M. Gibertini, E. Giannini, A. F. Morpurgo, and P. Maletinsky, Probing magnetism in 2D materials at the nanoscale with single-spin microscopy, Science **364**, 973 (2019).
[232] B. J. Maertz, A. P. Wijnheijmer, G. D. Fuchs, M. E. Nowakowski, and D. D. Awschalom, Vector magnetic field microscopy using nitrogen vacancy centers in diamond, Applied Physics Letters **96**, 092504 (2010).
[233] C. Phatak, A. K. Petford-Long, and M. De Graef, Recent advances in Lorentz microscopy, Current Opinion in Solid State and Materials Science **20**, 107 (2016).
[234] Y. Wu, S. Zhang, J. Zhang, W. Wang, Y. L. Zhu, J. Hu, G. Yin, K. Wong, C. Fang, C. Wan, X. Han, Q. Shao, T. Taniguchi, K. Watanabe, J. Zang, Z. Mao, X. Zhang, and K. L. Wang, Néel-type skyrmion in $WTe_2/Fe_3GeTe_2$ van der Waals heterostructure, Nature Communications **11**, 3 (2020).
[235] Z. Huang, A. R. C. McCray, Y. Li, D. J. Morrow, E. K. Qian, D. Young Chung, M. G. Kanatzidis, C. Phatak, and X. Ma, Raman Shifts in Two-Dimensional van der Waals Magnets Reveal Magnetic Texture Evolution, Nano Letters **24**, 1531 (2024).
[236] M. G. Han, J. A. Garlow, Y. Liu, H. Zhang, J. Li, D. DiMarzio, M. W. Knight, C. Petrovic, D. Jariwala, and Y. Zhu, Topological Magnetic-Spin Textures in Two-Dimensional van der Waals $Cr_2Ge_2Te_6$, Nano Letters **19**, 7859 (2019).
[237] S. Liu, M. Long, and Y. P. Wang, Theoretical Study on the Raman Effect Due to Magnons in Two-Dimensional Magnets, Nano Letters **23**, 7427 (2023).

[238] Y.-J. Sun, S.-M. Pang, and J. Zhang, Review of Raman spectroscopy of two-dimensional magnetic van der Waals materials, Chinese Physics B **30**, 117104 (2021).
[239] Y. Zhang, X. Wu, B. Lyu, M. Wu, S. Zhao, J. Chen, M. Jia, C. Zhang, L. Wang, X. Wang, Y. Chen, J. Mei, T. Taniguchi, K. Watanabe, H. Yan, Q. Liu, L. Huang, Y. Zhao, and M. Huang, Magnetic Order-Induced Polarization Anomaly of Raman Scattering in 2D Magnet $CrI_3$, Nano Letters **20**, 729 (2020).
[240] Y. J. Sun, J. M. Lai, S. M. Pang, X. L. Liu, P. H. Tan, and J. Zhang, Magneto-Raman Study of Magnon-Phonon Coupling in Two-Dimensional Ising Antiferromagnetic $FePS_3$, The Journal of Physical Chemistry Letters **13**, 1533 (2022).
[241] A. Simon, J. Ravez, V. Maisonneuve, C. Payen, and V. B. Cajipe, Paraelectric-Ferroelectric Transition in the Lamellar Thiophosphate $CuInP_2S_6$, Chemistry of Materials **6**, 1575 (1994).
[242] S. Aoki, Y. Dong, Z. Wang, X. S. W. Huang, Y. M. Itahashi, N. Ogawa, T. Ideue, and Y. Iwasa, Giant Modulation of the Second Harmonic Generation by Magnetoelectricity in Two-Dimensional Multiferroic $CuCrP_2S_6$, Advanced Materials **36**, 2312781 (2024).
[243] P. Liu, Y. Li, D. Hou, H. Zhu, H. Luo, S. Zhou, L. Wei, W. Niu, Z. Sheng, W. Mao, and Y. Pu, Switchable diode effect in 2D van der Waals ferroelectric CuCrP2S6, Applied Physics Letters **124** (2024).
[244] S. Wan, Y. Li, W. Li, X. Mao, W. Zhu, and H. Zeng, Room-temperature ferroelectricity and a switchable diode effect in two-dimensional α-$In_2Se_3$ thin layers, Nanoscale **10**, 14885 (2018).
[245] J. R. Brent, D. J. Lewis, T. Lorenz, E. A. Lewis, N. Savjani, S. J. Haigh, G. Seifert, B. Derby, and P. O'Brien, Tin(II) Sulfide (SnS) Nanosheets by Liquid-Phase Exfoliation of Herzenbergite: IV–VI Main Group Two-Dimensional Atomic Crystals, Journal of the American Chemical Society **137**, 12689 (2015).
[246] A. S. Sarkar, A. Mushtaq, D. Kushavah, and S. K. Pal, Liquid exfoliation of electronic grade ultrathin tin(II) sulfide (SnS) with intriguing optical response, npj 2D Materials and Applications **4**, 1 (2020).
[247] D. Yu, Q. Li, A. Wei, Y. Zhao, J. Liu, and Z. Xiao, Synthesis and characterization of the ultra-thin SnS flakes and the micron-thick SnS crystals by chemical vapor deposition, Journal of Materials Science: Materials in Electronics **30**, 10879 (2019).
[248] H. Z. A. Nalin Mehta, A. Dabral, O. Richard, P. Favia, H. Bender, A. Delabie, M. Caymax, M. Houssa, G. Pourtois, Structural characterization of SnS crystals formed by chemical vapour deposition, Journal of Microscopy **268**, 276 (2017).
[249] Z. Tian, C. Guo, M. Zhao, R. Li, and J. Xue, Two-Dimensional SnS: A Phosphorene Analogue with Strong In-Plane Electronic Anisotropy, ACS Nano **11**, 2219 (2017).
[250] R. Du, Y. Wang, M. Cheng, P. Wang, H. Li, W. Feng, L. Song, J. Shi, and J. He, Two-dimensional multiferroic material of metallic p-doped SnSe, Nature Communications **13**, 6130 (2022).
[251] V. Tayari, B. V. Senkovskiy, D. Rybkovskiy, N. Ehlen, A. Fedorov, C. Y. Chen, J. Avila, M. Asensio, A. Perucchi, P. di Pietro, L. Yashina, I. Fakih, N. Hemsworth, M. Petrescu, G. Gervais, A. Grüneis, and T. Szkopek, Quasi-two-dimensional thermoelectricity in SnSe, Physical Review B **97**, 045424 (2018).
[252] S.-H. Cho, K. Cho, N.-W. Park, S. Park, J.-H. Koh, and S.-K. Lee, Multi-Layer SnSe Nanoflake Field-Effect Transistors with Low-Resistance Au Ohmic Contacts, Nanoscale Research Letters **12**, 373 (2017).

[253] Y. Huang, L. Li, Y.-H. Lin, and C.-W. Nan, Liquid Exfoliation Few-Layer SnSe Nanosheets with Tunable Band Gap, The Journal of Physical Chemistry C **121**, 17530 (2017).
[254] K. Chang, and S. S. P. Parkin, The growth and phase distribution of ultrathin SnTe on graphene, APL Materials **7**, 041102 (2019).
[255] Y. Su, C. Ding, Y. Yao, R. Fu, M. Xue, X. Liu, J. Lin, F. Wang, X. Zhan, and Z. Wang, Orietation-controlled synthesis and Raman study of 2D SnTe, Nanotechnology **34**, 505206 (2023).
[256] D. Tan, H. E. Lim, F. Wang, N. B. Mohamed, S. Mouri, W. Zhang, Y. Miyauchi, M. Ohfuchi, and K. Matsuda, Anisotropic optical and electronic properties of two-dimensional layered germanium sulfide, Nano Research **10**, 546 (2017).
[257] D. Lam, K.-S. Chen, J. Kang, X. Liu, and M. C. Hersam, Anhydrous Liquid-Phase Exfoliation of Pristine Electrochemically Active GeS Nanosheets, Chemistry of Materials **30**, 2245 (2018).
[258] C. Lan, C. Li, Y. Yin, H. Guo, and S. Wang, Synthesis of single-crystalline GeS nanoribbons for high sensitivity visible-light photodetectors, Journal of Materials Chemistry C **3**, 8074 (2015).
[259] R. K. Ulaganathan, Y.-Y. Lu, C.-J. Kuo, S. R. Tamalampudi, R. Sankar, K. M. Boopathi, A. Anand, K. Yadav, R. J. Mathew, C.-R. Liu, F. C. Chou, and Y.-T. Chen, High photosensitivity and broad spectral response of multi-layered germanium sulfide transistors, Nanoscale **8**, 2284 (2016).
[260] C. Li, L. Huang, G. P. Snigdha, Y. Yu, and L. Cao, Role of Boundary Layer Diffusion in Vapor Deposition Growth of Chalcogenide Nanosheets: The Case of GeS, ACS Nano **6**, 8868 (2012).
[261] B. Mukherjee, Y. Cai, H. R. Tan, Y. P. Feng, E. S. Tok, and C. H. Sow, NIR Schottky Photodetectors Based on Individual Single-Crystalline GeSe Nanosheet, ACS Applied Materials & Interfaces **5**, 9594 (2013).
[262] D. Ma, J. Zhao, R. Wang, C. Xing, Z. Li, W. Huang, X. Jiang, Z. Guo, Z. Luo, Y. Li, J. Li, S. Luo, Y. Zhang, and H. Zhang, Ultrathin GeSe Nanosheets: From Systematic Synthesis to Studies of Carrier Dynamics and Applications for a High-Performance UV–Vis Photodetector, ACS Applied Materials & Interfaces **11**, 4278 (2019).
[263] Y. Ye, Q. Guo, X. Liu, C. Liu, J. Wang, Y. Liu, and J. Qiu, Two-Dimensional GeSe as an Isostructural and Isoelectronic Analogue of Phosphorene: Sonication-Assisted Synthesis, Chemical Stability, and Optical Properties, Chemistry of Materials **29**, 8361 (2017).
[264] W. Li, X. Zhang, J. Yang, S. Zhou, C. Song, P. Cheng, Y.-Q. Zhang, B. Feng, Z. Wang, Y. Lu, K. Wu, and L. Chen, Emergence of ferroelectricity in a nonferroelectric monolayer, Nature Communications **14**, 2757 (2023).
[265] Z. Ben Aziza, D. Pierucci, H. Henck, M. G. Silly, C. David, M. Yoon, F. Sirotti, K. Xiao, M. Eddrief, J.-C. Girard, and A. Ouerghi, Tunable quasiparticle band gap in few-layer GaSe/graphene van der Waals heterostructures, Physical Review B **96**, 035407 (2017).
[266] Z. Ben Aziza, V. Zólyomi, H. Henck, D. Pierucci, M. G. Silly, J. Avila, S. J. Magorrian, J. Chaste, C. Chen, M. Yoon, K. Xiao, F. Sirotti, M. C. Asensio, E. Lhuillier, M. Eddrief, V. I. Fal'ko, and A. Ouerghi, Valence band inversion and spin-orbit effects in the electronic structure of monolayer GaSe, Physical Review B **98**, 115405 (2018).
[267] X. Li, L. Basile, B. Huang, C. Ma, J. Lee, I. V. Vlassiouk, A. A. Puretzky, M.-W. Lin, M. Yoon, M. Chi, J. C. Idrobo, C. M. Rouleau, B. G. Sumpter, D. B. Geohegan, and K. Xiao,

Van der Waals Epitaxial Growth of Two-Dimensional Single-Crystalline GaSe Domains on Graphene, ACS Nano **9**, 8078 (2015).
[268] W. Ding, J. Zhu, Z. Wang, Y. Gao, D. Xiao, Y. Gu, Z. Zhang, and W. Zhu, Prediction of intrinsic two-dimensional ferroelectrics in $In_2Se_3$ and other $III_2$-$VI_3$ van der Waals materials, Nature Communications **8**, 14956 (2017).
[269] W. Feng, W. Zheng, F. Gao, X. Chen, G. Liu, T. Hasan, W. Cao, and P. Hu, Sensitive Electronic-Skin Strain Sensor Array Based on the Patterned Two-Dimensional α-$In_2Se_3$, Chemistry of Materials **28**, 4278 (2016).
[270] X. Jiang, Q. Liu, J. Xing, N. Liu, Y. Guo, Z. Liu, and J. Zhao, Recent progress on 2D magnets: Fundamental mechanism, structural design and modification, Applied Physics Reviews **8**, 031305 (2021).
[271] Y. Guan, L. Miao, J. He, J. Ning, Y. Chen, W. Xie, J. Sun, V. Gopalan, J. Zhu, X. Wang, N. Alem, Q. Zhang, and Z. Mao, Layered Semiconductor $Cr_{0.32}Ga_{0.68}Te_{2.33}$ with Concurrent Broken Inversion Symmetry and Ferromagnetism: A Bulk Ferrovalley Material Candidate, Journal of the American Chemical Society **145**, 4683 (2023).
[272] Z. Shu, H. Wang, N. H. Jo, C. Jozwiak, A. Bostwick, E. Rotenberg, W. Xie, and T. Kong, Synthesis and physical properties of a new layered ferromagnet $Cr_{1.21}Te_2$, Physical Review Materials **7**, 044406 (2023).
[273] Z. Tu, T. Xie, Y. Lee, J. Zhou, A. S. Admasu, Y. Gong, N. Valanoor, J. Cumings, S.-W. Cheong, I. Takeuchi, K. Cho, and C. Gong, Ambient effect on the Curie temperatures and magnetic domains in metallic two-dimensional magnets, npj 2D Materials and Applications **5**, 62 (2021).
[274] P. Liu, H. Zhu, Y. Xiang, W. Niu, Y. Lu, and Y. Pu, Magnetic and magneto-transport studies in van der Waals $Fe_{5-x}GeTe_2$ flakes, Applied Physics Letters **121**, 112402 (2022).
[275] M. Mi, X. Zheng, S. Wang, Y. Zhou, L. Yu, H. Xiao, H. Song, B. Shen, F. Li, L. Bai, Y. Chen, S. Wang, X. Liu, and Y. Wang, Variation between Antiferromagnetism and Ferrimagnetism in $NiPS_3$ by Electron Doping, Advanced Functional Materials **32**, 2112750 (2022).
[276] W. Zhuo, B. Lei, S. Wu, F. Yu, C. Zhu, J. Cui, Z. Sun, D. Ma, M. Shi, H. Wang, W. Wang, T. Wu, J. Ying, S. Wu, Z. Wang, and X. Chen, Manipulating Ferromagnetism in Few-Layered $Cr_2Ge_2Te_6$, Advanced Materials **33**, 2008586 (2021).
[277] V. Ostwal, T. Shen, and J. Appenzeller, Efficient Spin-Orbit Torque Switching of the Semiconducting Van Der Waals Ferromagnet $Cr_2Ge_2Te_6$, Advanced Materials **32**, 1906021 (2020).
[278] P. Li, C. Wang, J. Zhang, S. Chen, D. Guo, W. Ji, and D. Zhong, Single-layer $CrI_3$ grown by molecular beam epitaxy, Science Bulletin **65**, 1064 (2020).
[279] B. Yang, Y. M. Goh, S. H. Sung, G. Ye, S. Biswas, D. A. S. Kaib, R. Dhakal, S. Yan, C. Li, S. Jiang, F. Chen, H. Lei, R. He, R. Valentí, S. M. Winter, R. Hovden, and A. W. Tsen, Magnetic anisotropy reversal driven by structural symmetry-breaking in monolayer α-$RuCl_3$, Nature Materials **22**, 50 (2023).
[280] Z. Wang, L. Liu, H. Zheng, M. Zhao, K. Yang, C. Wang, F. Yang, H. Wu, and C. Gao, Direct observation of the Mottness and p–d orbital hybridization in the epitaxial monolayer α-$RuCl_3$, Nanoscale **14**, 11745 (2022).
[281] M. Grönke, P. Schmidt, M. Valldor, S. Oswald, D. Wolf, A. Lubk, B. Büchner, and S. Hampel, Chemical vapor growth and delamination of α-$RuCl_3$ nanosheets down to the monolayer limit, Nanoscale **10**, 19014 (2018).

[282] W. Zhou, A. J. Bishop, M. Zhu, I. Lyalin, R. Walko, J. A. Gupta, J. Hwang, and R. K. Kawakami, Kinetically Controlled Epitaxial Growth of $Fe_3GeTe_2$ van der Waals Ferromagnetic Films, ACS Applied Electronic Materials **4**, 3190 (2022).
[283] D. H. Luong, T. L. Phan, G. Ghimire, D. L. Duong, and Y. H. Lee, Revealing antiferromagnetic transition of van der Waals $MnPS_3$ via vertical tunneling electrical resistance measurement, APL Materials **7**, 081102 (2019).
[284] J.-U. Lee, S. Lee, J. H. Ryoo, S. Kang, T. Y. Kim, P. Kim, C.-H. Park, J.-G. Park, and H. Cheong, Ising-Type Magnetic Ordering in Atomically Thin $FePS_3$, Nano Letters **16**, 7433 (2016).
[285] K.-z. Du, X.-z. Wang, Y. Liu, P. Hu, M. I. B. Utama, C. K. Gan, Q. Xiong, and C. Kloc, Weak Van der Waals Stacking, Wide-Range Band Gap, and Raman Study on Ultrathin Layers of Metal Phosphorus Trichalcogenides, ACS Nano **10**, 1738 (2016).
[286] S. Kezilebieke, M. N. Huda, P. Dreher, I. Manninen, Y. Zhou, J. Sainio, R. Mansell, M. M. Ugeda, S. van Dijken, H.-P. Komsa, and P. Liljeroth, Electronic and magnetic characterization of epitaxial $VSe_2$ monolayers on superconducting $NbSe_2$, Communications Physics **3**, 116 (2020).
[287] P. M. Coelho, K. Nguyen Cong, M. Bonilla, S. Kolekar, M.-H. Phan, J. Avila, M. C. Asensio, I. I. Oleynik, and M. Batzill, Charge Density Wave State Suppresses Ferromagnetic Ordering in $VSe_2$ Monolayers, The Journal of Physical Chemistry C **123**, 14089 (2019).
[288] Z. Zhang, J. Niu, P. Yang, Y. Gong, Q. Ji, J. Shi, Q. Fang, S. Jiang, H. Li, X. Zhou, L. Gu, X. Wu, and Y. Zhang, Van der Waals Epitaxial Growth of 2D Metallic Vanadium Diselenide Single Crystals and their Extra-High Electrical Conductivity, Advanced Materials **29**, 1702359 (2017).
[289] B. Li, Z. Wan, C. Wang, P. Chen, B. Huang, X. Cheng, Q. Qian, J. Li, Z. Zhang, G. Sun, B. Zhao, H. Ma, R. Wu, Z. Wei, Y. Liu, L. Liao, Y. Ye, Y. Huang, X. Xu, X. Duan, W. Ji, and X. Duan, Van der Waals epitaxial growth of air-stable $CrSe_2$ nanosheets with thickness-tunable magnetic order, Nature Materials **20**, 818 (2021).
[290] M. Liu, J. Gou, Z. Liu, Z. Chen, Y. Ye, J. Xu, X. Xu, D. Zhong, G. Eda, and A. T. S. Wee, Phase-selective in-plane heteroepitaxial growth of H-phase $CrSe_2$, Nature Communications **15**, 1765 (2024).
[291] L. Meng, Z. Zhou, M. Xu, S. Yang, K. Si, L. Liu, X. Wang, H. Jiang, B. Li, P. Qin, P. Zhang, J. Wang, Z. Liu, P. Tang, Y. Ye, W. Zhou, L. Bao, H.-J. Gao, and Y. Gong, Anomalous thickness dependence of Curie temperature in air-stable two-dimensional ferromagnetic 1T-$CrTe_2$ grown by chemical vapor deposition, Nature Communications **12**, 809 (2021).
[292] X. Sun, W. Li, X. Wang, Q. Sui, T. Zhang, Z. Wang, L. Liu, D. Li, S. Feng, S. Zhong, H. Wang, V. Bouchiat, M. Nunez Regueiro, N. Rougemaille, J. Coraux, A. Purbawati, A. Hadj-Azzem, Z. Wang, B. Dong, X. Wu, T. Yang, G. Yu, B. Wang, Z. Han, X. Han, and Z. Zhang, Room temperature ferromagnetism in ultra-thin van der Waals crystals of 1T-$CrTe_2$, Nano Research **13**, 3358 (2020).
[293] J.-J. Xian, C. Wang, J.-H. Nie, R. Li, M. Han, J. Lin, W.-H. Zhang, Z.-Y. Liu, Z.-M. Zhang, M.-P. Miao, Y. Yi, S. Wu, X. Chen, J. Han, Z. Xia, W. Ji, and Y.-S. Fu, Spin mapping of intralayer antiferromagnetism and field-induced spin reorientation in monolayer $CrTe_2$, Nature Communications **13**, 257 (2022).
[294] X. Zhang, Q. Lu, W. Liu, W. Niu, J. Sun, J. Cook, M. Vaninger, P. F. Miceli, D. J. Singh, S.-W. Lian, T.-R. Chang, X. He, J. Du, L. He, R. Zhang, G. Bian, and Y. Xu, Room-temperature

intrinsic ferromagnetism in epitaxial $CrTe_2$ ultrathin films, Nature Communications **12**, 2492 (2021).
[295] K. Lasek, P. M. Coelho, K. Zberecki, Y. Xin, S. K. Kolekar, J. Li, and M. Batzill, Molecular Beam Epitaxy of Transition Metal (Ti-, V-, and Cr-) Tellurides: From Monolayer Ditellurides to Multilayer Self-Intercalation Compounds, ACS Nano **14**, 8473 (2020).
[296] Y. Deng, Y. Yu, M. Z. Shi, Z. Guo, Z. Xu, J. Wang, X. H. Chen, and Y. Zhang, Quantum anomalous Hall effect in intrinsic magnetic topological insulator $MnBi_2Te_4$, Science **367**, 895 (2020).
[297] M. de Jong, W. Chen, H. Geerlings, M. Asta, and K. A. Persson, A database to enable discovery and design of piezoelectric materials, Scientific Data **2**, 150053 (2015).
[298] X.-Y. Ma, H.-Y. Lyu, X.-J. Dong, Z. Zhang, K.-R. Hao, Q.-B. Yan, and G. Su, Voting Data-Driven Regression Learning for Accelerating Discovery of Advanced Functional Materials and Applications to Two-Dimensional Ferroelectric Materials, The Journal of Physical Chemistry Letters **12**, 973 (2021).
[299] M. Kruse, U. Petralanda, M. N. Gjerding, K. W. Jacobsen, K. S. Thygesen, and T. Olsen, Two-dimensional ferroelectrics from high throughput computational screening, npj Computational Materials **9**, 45 (2023).
[300] X. Jin, Y.-Y. Zhang, and S. Du, Recent progress in the theoretical design of two-dimensional ferroelectric materials, Fundamental Research **3**, 322 (2023).
[301] J. Li, M. Chen, A. Samad, H. Dong, A. Ray, J. Zhang, X. Jiang, U. Schwingenschlögl, J. Domke, C. Chen, Y. Han, T. Fritz, R. S. Ruoff, B. Tian, and X. Zhang, Wafer-scale single-crystal monolayer graphene grown on sapphire substrate, Nature Materials **21**, 740 (2022).
[302] S. Fukamachi, P. Solís-Fernández, K. Kawahara, D. Tanaka, T. Otake, Y.-C. Lin, K. Suenaga, and H. Ago, Large-area synthesis and transfer of multilayer hexagonal boron nitride for enhanced graphene device arrays, Nature Electronics **6**, 126 (2023).
[303] J. Wang, X. Xu, T. Cheng, L. Gu, R. Qiao, Z. Liang, D. Ding, H. Hong, P. Zheng, Z. Zhang, Z. Zhang, S. Zhang, G. Cui, C. Chang, C. Huang, J. Qi, J. Liang, C. Liu, Y. Zuo, G. Xue, X. Fang, J. Tian, M. Wu, Y. Guo, Z. Yao, Q. Jiao, L. Liu, P. Gao, Q. Li, R. Yang, G. Zhang, Z. Tang, D. Yu, E. Wang, J. Lu, Y. Zhao, S. Wu, F. Ding, and K. Liu, Dual-coupling-guided epitaxial growth of wafer-scale single-crystal $WS_2$ monolayer on vicinal a-plane sapphire, Nature Nanotechnology **17**, 33 (2022).
[304] W. Zhu, and X. Hong, Getting two-dimensional materials ready for industrial manufacturing, Nature Electronics **6**, 931 (2023).
[305] H. Yoon, T. K. Truttmann, F. Liu, B. E. Matthews, S. Choo, Q. Su, V. Saraswat, S. Manzo, M. S. Arnold, M. E. Bowden, J. K. Kawasaki, S. J. Koester, S. R. Spurgeon, S. A. Chambers, and B. Jalan, Freestanding epitaxial $SrTiO_3$ nanomembranes via remote epitaxy using hybrid molecular beam epitaxy, Science Advances **8**, eadd5328 (2022).
[306] C. S. Chang, K. S. Kim, B.-I. Park, J. Choi, H. Kim, J. Jeong, M. Barone, N. Parker, S. Lee, X. Zhang, K. Lu, J. M. Suh, J. Kim, D. Lee, N. M. Han, M. Moon, Y. S. Lee, D.-H. Kim, D. G. Schlom, Y. J. Hong, and J. Kim, Remote epitaxial interaction through graphene, Science Advances **9**, eadj5379 (2023).
[307] N. Nagaosa, and Y. Tokura, Topological properties and dynamics of magnetic skyrmions, Nature Nanotechnology **8**, 899 (2013).
[308] R. Wiesendanger, Nanoscale magnetic skyrmions in metallic films and multilayers: a new twist for spintronics, Nature Reviews Materials **1**, 16044 (2016).

[309] A. Fert, N. Reyren, and V. Cros, Magnetic skyrmions: advances in physics and potential applications, Nature Reviews Materials **2**, 17031 (2017).
[310] Y. Tokura, and N. Kanazawa, Magnetic Skyrmion Materials, Chemical Reviews **121**, 2857 (2021).
[311] X. Wang, C. Zhu, Y. Deng, R. Duan, J. Chen, Q. Zeng, J. Zhou, Q. Fu, L. You, S. Liu, J. H. Edgar, P. Yu, and Z. Liu, Van der Waals engineering of ferroelectric heterostructures for long-retention memory, Nature Communications **12**, 1109 (2021).
[312] X. Hong, Emerging ferroelectric transistors with nanoscale channel materials: the possibilities, the limitations, Journal of Physics: Condensed Matter **28**, 103003 (2016).
[313] D. Li, X. Huang, Q. Wu, L. Zhang, Y. Lu, and X. Hong, Ferroelectric Domain Control of Nonlinear Light Polarization in $MoS_2$ via $PbZr_{0.2}Ti_{0.8}O_3$ Thin Films and Free-Standing Membranes, Advanced Materials **35**, 2208825 (2023).
[314] D. Li, S. Sun, K. Wang, Z. Ahmadi, J. E. Shield, S. Ducharme, and X. Hong, Assembly of Close-Packed Ferroelectric Polymer Nanowires via Interface-Epitaxy with $ReS_2$, Advanced Materials **33**, 2100214 (2021).
[315] D. Li, Z. Xiao, H. R. Golgir, L. Jiang, V. R. Singh, K. Keramatnejad, K. E. Smith, X. Hong, L. Jiang, J.-F. Silvain, and Y. Lu, Large-Area 2D/3D $MoS_2$–$MoO_2$ Heterostructures with Thermally Stable Exciton and Intriguing Electrical Transport Behaviors, Advanced Electronic Materials **3**, 1600335 (2017).
[316] C. Chen, Y. Zhou, L. Tong, Y. Pang, and J. Xu, Emerging 2D Ferroelectric Devices for In-Sensor and In-Memory Computing, Advanced Materials **n/a**, 2400332 (2024).
[317] S. Yang, T. Zhang, and C. Jiang, van der Waals Magnets: Material Family, Detection and Modulation of Magnetism, and Perspective in Spintronics, Advanced Science **8**, 2002488 (2021).